Remote End Fault Diagnosis of Microgrid-Based Power Distribution Network

Thesis Submitted

by

Sagnik Datta

Doctor of Philosophy (Engineering)

Department of Electrical Engineering

Faculty Council of Engineering &Technology

Jadavpur University

Kolkata, India

2025

INDEX NO. 164/22/E

Remote End Fault Diagnosis of Microgrid-Based Power Distribution Network

Under the guidance of

Dr. Surajit Chattopadhayay

Professor

Department of Electrical Engineering,

Ghani Khan Choudhury Institute of Engineering and Technology

and

Dr. Arabinda Das

Professor

Department of Electrical Engineering, Jadavpur University

<u>List of Publications:</u>

List of papers published in journals

1. **Datta, S**., Chattopadhyaya, A., Chattopadhyay, S., & Das, A. (2020). Line to ground and line to line fault analysis in IEEE standard 9 Bus System. AMSE, 93(1-4), 10-18.
2. **Datta, S.**, Chattopadhyaya, A., Chattopadhayay, S., & Das, A. (2022). S-transform based kurtosis analysis for detection of LG and LL faults in 14 Bus microgrid system. IETE Journal of Research, 68(5), 3766-3777.
3. **Datta, S.**, Chattopadhyaya, A., Chattopadhayay, S., & Das, A. (2024). ANN-Based Statistical Computation for Remote End Fault Monitoring of the IEEE 14 Bus Microgrid Network. IETE Journal of Research, 70(3), 2530-2544.

List of papers under review in journals

1. **Datta, S.,** Chattopadhyaya, A., Chattopadhayay, S., & Das, A, “S – Transform Based Skewness Computation of Current Signature for Fault Assessment in IEEE-Standard 14 Bus Microgrid System at Remote Terminal”, under review in Journal of Institution of Engineers (India): Series (B).

List of Patents: Nil

List of Presentation in National/ International Conference

1. **Datta, S.**, Chattopadhyaya, A., Chattopadhyay, S., & Das, A. (2020, October). Harmonic distortion, inter-harmonic group magnitude and discrete wavelet transformation based statistical parameter estimation for line to ground fault analysis in microgrid system. In Michael Faraday IET International Summit 2020 (MFIIS 2020) (Vol. 2020, pp. 177-184). IET.
2. **Datta, S.**, Chattopadhyay, S., & Das, A. (2017, November). FFT based harmonic assessment of line to ground fault in 14 bus microgrid system. In International Conference on Modelling and Simulation (pp. 73-86). Cham: Springer International Publishing.

List of Book Chapters

1. **Datta, S.**, Chattopadhyaya, A., Chattopadhyay, S., & Das, A. (2024). Comparative Study of Different Existing Standard Microgrid Networks. Linear and Nonlinear System Modeling, 33-47, ISBN 978-111984-742-7.

"Statement of Originality"

I.......SAGNIK DATTA...........registered on ......7^{th} June, 2022........do hereby declare that this thesis entitled..."Remote End Fault Diagnosis of Microgrid-Based Power Distribution Network"... contains literature survey and original research work done by the undersigned candidate as part of Doctoral studies.

All information in this thesis have been obtained and presented in accordance with existing academic rules and ethical conduct. I declare that, as required by these rules and conduct, I have fully cited and referred all materials and results that are not original to this work.

I also declare that I have checked this thesis as per the "Policy on Anti Plagiarism, Jadavpur University, 2019", and the level of similarity as checked by iThenticate software is ___3___%.

Signature of Candidate: Sagnik Datta

Date: 08.04.2026.

Certified by Supervisor(s):

(Signature with date, seal)

1. Analinda Das 08/04/2026
Professor
Electrical Engg. Deptt.
Jadavpur University
Kolkata - 700 032

2. Surajit Chattopadhyay 08.04.2026
Associate Professor
Department of Electrical Engineering
Gani Khan Choudhury Institute of Engineering & Technology
Narayanpur Malda-732141

CERTIFICATE FROM THE SUPERVISORS

This is to certify that the thesis entitled "Remote End Fault Diagnosis of Microgrid-Based Power Distribution Network" submitted by Shri/~~Smt~~ SAGNIK DATTA, who got his/~~her~~ name registered on 7th June, 2022 for the award of Ph.D. (Engg./Pharmacy) degree of Jadavpur University is absolutely based upon his/~~her~~ own work under the supervision of Dr. Arabinda Das & Dr. Surajit Chattopadhayay and that neither his/~~her~~ thesis nor any part of the thesis has been submitted for any degree/diploma or any other academic award anywhere before.

1. Arabinda Das 08/04/2026
Signature of the Supervisor
And date with Office Seal
Professor
Electrical Engg. Deptt.
Jadavpur University
Kolkata - 700 032

2. Surajit Chattopadhyay 08.04.2026
Signature of the Supervisor
and date with Office Seal
Associate Professor
Department of Electrical Engineering
Ghani Khan Choudhury Institute of Engineering & Technology
Narayanpur, Malda-732141

Acknowledgement

Firstly, praises and thanks to God, the Almighty, for His blessings which has helped me to complete my research works successfully.

I would like to express my sincere gratitude to my research supervisors Dr. Surajit Chattopadhayay, Professor, Department of Electrical Engineering, Ghani Khan Choudhury Institute of Engineering and Technology, Malda and Dr. Arabinda Das, Professor, Department of Electrical Engineering, Jadavpur University, Kolkata for providing me with the opportunity to carry out research and their continuous support and guidance for my Ph.D. related research. I am again thankful to them for their vision, patience, immense knowledge and relentless motivation which have continued to inspire me. Their persistent guidance and mentorship has helped me during the time of research as well as while writing this thesis. I would also like to extend my heartfelt thanks to them for their empathy during the crisis time; and most importantly, the faith with which they have entrusted me with the research opportunity throughout the tenure. It was really a great privilege and honour to work and finally carry out research under their blessed guidance.

Besides my advisors, I would also like to thank the rest of my thesis committee members for their insightful comments and encouragement, as well as for the relevant questions which compelled me to widen my research from various perspectives. My sincere thanks also go to my colleague and friend, Dr. Aveek Chattopadhyaya, who has helped me with his extremely vital advices at different points of time during this research.

Finally, and most importantly, I am extremely grateful to all my family members, for their love, prayers and sacrifices which have all helped me to carry out research. I am most thankful to my wife for her great understanding, patience, prayers, admiration, and continuous support. Her tremendous inspiration throughout my research work has truly been instrumental in completing this thesis.

Sagnik Datta

(SAGNIK DATTA)

Date: 08.04.2026

Place: Falakata

Contents

Abstract

The expanding integration of Distributed Energy Resources (DERs), such as solar photovoltaic (P–V) systems, battery storage, and diesel generators, combined with advancements in energy management technologies, has fundamentally altered the structure of contemporary power systems. This evolution has given rise to microgrids—self-contained, manageable clusters of distributed energy sources and loads operating within specific electrical boundaries. Microgrids can function in grid-connected mode, exchanging energy with the main grid or in islanded mode, independently meeting local power demands. By enhancing system reliability, resilience, sustainability, and operational flexibility, microgrids play a crucial role in advancing smart, self-reliant energy systems.

Nevertheless, the widespread adoption of microgrids presents significant technical and protection challenges. Unlike traditional radial power networks, microgrids are dynamic, non-radial systems having multiple generation points, bidirectional power flows and frequent mode transitions. The unpredictable output of renewable energy sources, combined with variable fault impedances, lower voltage and current levels, complicates fault detection and isolation. Conventional protection strategies, which rely on fixed relay thresholds and simple current–voltage correlations, often prove inadequate. Additionally, the non-stationary nature of fault currents renders traditional frequency-domain methods, such as the Fast Fourier Transform (FFT), insufficient for accurate fault identification and localization.

To tackle these issues, this thesis proposes an innovative Digital Signal Processing (DSP) based protection framework for microgrid networks, designed to detect location and type of faults independently of current, voltage, fault impedance, or power flow direction. This approach hinges on the principle that faults induce significant changes in the harmonic content and statistical properties of outgoing currents from generator buses, which can be captured using advanced time–frequency analysis techniques.

Two DSP-based approaches are developed and examined: one based on the Discrete Wavelet Transform (DWT) and the other on the Stockwell Transform (S-Transform). The DWT-based method uses multi-resolution wavelet decomposition to analyze transient current signals, extracting statistical features like skewness and kurtosis. These features form the basis of a rule-based system for identifying fault types and locations, integrated with an

Artificial Neural Network (ANN) and fog computing architecture to enable real-time processing and scalability.

The S-Transform-based method, in contrast, delivers a continuous, high-resolution time–frequency representation of current signals without requiring a predefined mother wavelet, offering enhanced adaptability across diverse operating conditions. By analyzing statistical parameters derived from S-Transform matrices, the method identifies characteristic patterns associated with various fault types, enabling precise classification of both symmetrical (L–L–L, L–L–L–G) and unsymmetrical (L–G, L–L, L–L–G) faults.

The proposed algorithms were evaluated through extensive simulations on the IEEE Standard 14-bus microgrid system. Various fault scenarios, including Line-to-Ground (L–G), Double-Line (L–L), Double-Line-to-Ground (L–L–G), and Three-Line (L–L–L) faults, were simulated under different pre-fault conditions. Current measurements from generator buses were processed using the S-Transform method. The algorithm accurately identified fault locations and types, with results closely matching known fault conditions. The study also explored uncertainties related to DERs, such as P–V cells, batteries, and diesel generators, by varying their generation levels at 100%, 80%, and 50%. While harmonic component magnitudes varied, the skewness values from S-Transform matrices remained stable, demonstrating the robustness of the algorithm, to DER output fluctuations and fault resistance variations.

Comparative analysis showed that both DSP-based methods outperform conventional FFT-based approaches in addressing non-stationary fault signals. The DWT-based method excels in computational efficiency and suitability for real-time applications, while the S-Transform-based approach offers greater accuracy in fault localization and resilience to parameter variations.

List of Figures

List of Tables

List of Abbreviations

L-G	-	Line to Ground Fault
L-L	-	Line to Line Fault
L-L-G	-	Line to Line to Ground Fault
L-L-L	-	Line to Line to Line Fault
L-L-L-G	-	Line to Line to Line to Ground Fault
WT	-	Wavelet Transform
CWT	-	Continuous Wavelet Transform
DWT	-	Discrete Wavelet Transform
S-Transform	-	Stockwell Transform
RMS_A	-	Root Mean Square Value of Approximate Coefficient
RMS_D	-	Root Mean Square Value of Detail Coefficient
S_A	-	Skewness of Approximate Coefficient
S_D	-	Skewness of Detail Coefficient
K_A	-	Kurtosis of Approximate Coefficient
K_D	-	Kurtosis of Detail Coefficient

Chapter 1

Introduction

This thesis is directed towards the investigation of signal processing based statistical parameter analysis for fault diagnosis in a microgrid network. Different methods of fault diagnosis are implemented in standard microgrid network and comparative studies between the proposed methods are also performed.

1.1 Introduction

A microgrid is a localized cluster of distributed energy resources (DER) and loads within a defined electrical boundary, functioning as a single, manageable unit in relation to the main grid. It can operate either in sync with the conventional power grid in grid-connected mode or independently in island mode. Effective fault identification and isolation is of paramount importance in a microgrid system as well. However, traditional methods of fault assessment fail in a microgrid environment. In recent years, a lot of research work is being done to design robust protection schemes for microgrid networks which overcome the challenges in fault detection present in a microgrid environment.

This work presented in this thesis addresses several challenges in fault diagnosis within a microgrid network, achieving reliable accuracy. Rather than focusing on the amplitudes of harmonic components in the currents from various generator buses, the primary emphasis is kept on examining changes in the statistical characteristics of these current harmonics.

1.2 Faults in Microgrid Network under Consideration

Microgrids with over-head transmission lines are susceptible to the same types of faults as over-head transmission lines in conventional power grids. The faults occurring in over-head transmission lines can be broadly classified into two categories: Symmetrical Fault and Unsymmetrical Fault.

A triple line fault (L-L-L) or a triple line-to-ground fault (L-L-L-G), known as a symmetrical fault, maintains balance in a three-phase power network if it was balanced prior to the occurrence of the fault. This happens because all three phases are affected similarly by these types of faults.

In most real-world scenarios, faults are of unsymmetrical nature because they typically impact only one or occasionally two lines, disrupting one or two phases and altering the electrical parameters of the affected lines. These faults are of the following types:

- Line to Ground (L-G) Fault.
- Double Line (L-L) Fault.

- Double Line to Ground (L-L-G) Fault.

Faults involving ground connections, such as line-to-ground (L-G) or double line-to-ground (L-L-G) faults, exhibit distinct characteristics compared to faults without ground involvement. The ground connection in these faults gives rise to the zero-sequence current component (I_0) in all three phases. Zero-sequence current component flow through the transmission line via grounded points, such as the grounded neutral and become particularly significant during unsymmetrical faults, especially ground-related ones. Ground faults are heavily influenced by these zero-sequence currents, which is evident in their post-fault voltage and current profiles. Ground faults generate an arcing resistance to the ground, leading to the malfunction of distance relays, particularly in short transmission lines, such as those very frequently found in microgrid environments.

In L-G faults, one line is either fully or partially shorted to ground. Regardless of whether the fault is transient or permanent, the voltage and current parameters of the affected line are significantly disrupted. Additionally, zero-sequence currents circulate through the unaffected lines via the grounded faulty line and the grounded neutral, which is also connected to these lines. This results in minor disturbances in the unaffected lines, observable in their post-fault voltage and current waveforms. Similarly, in L-L-G faults, the two directly affected lines experience the most significant disturbances but the third, unaffected line is also impacted to a lesser extent by the zero-sequence currents flowing through the two faulty lines to ground and the grounded neutral. Thus, the third line gets affected to some degree too. In contrast, for asymmetrical faults like double line (L-L) faults, the absence of ground involvement is evident in post-fault measurements. The lack of ground connection minimizes the flow of zero-sequence currents through the unaffected lines, leaving the third line largely undisturbed by the fault occurring between the other two lines. This distinction clearly differentiates L-L faults from L-L-G faults.

1.3 Objective of the Work

Two fundamental differences between traditional power grid and microgrid network are that in a microgrid environment neither the structure of the grid is ‘radial’ nor it is ‘passive’ in nature. Microgrids also have much lower levels of voltages and currents in comparison with the traditional power grids. So, the protective equipments and protection schemes employed for protection of traditional grids does not work satisfactorily. Moreover, the direction of power flow in a microgrid network may change depending upon its mode of operation, time of the day and available sources, which adds additional challenges in designing a protection strategy.

Aforementioned challenges call for a centralized protection scheme which will be independent of voltage and current levels, direction of current flow and fault impedance. So, objective of our work is outlined as follows:

- To frame a protection scheme using digital signal processing based statistical parameter analysis for microgrid networks which will be faster than existing schemes and also be able to distinguish fault type and identify the location of the fault.
- The proposed protection scheme must be independent of the values of voltage and currents.
- It must not be affected by variation of fault resistance i.e. the protection scheme should be well suited to successfully identify ground faults in short lines.

The following chapters contain the research work done with an aim to fulfill the objectives outlined above.

1.4 Detailed Workflow of this Research

Complete workflow of this thesis is represented by Fig. 1.1 given below.

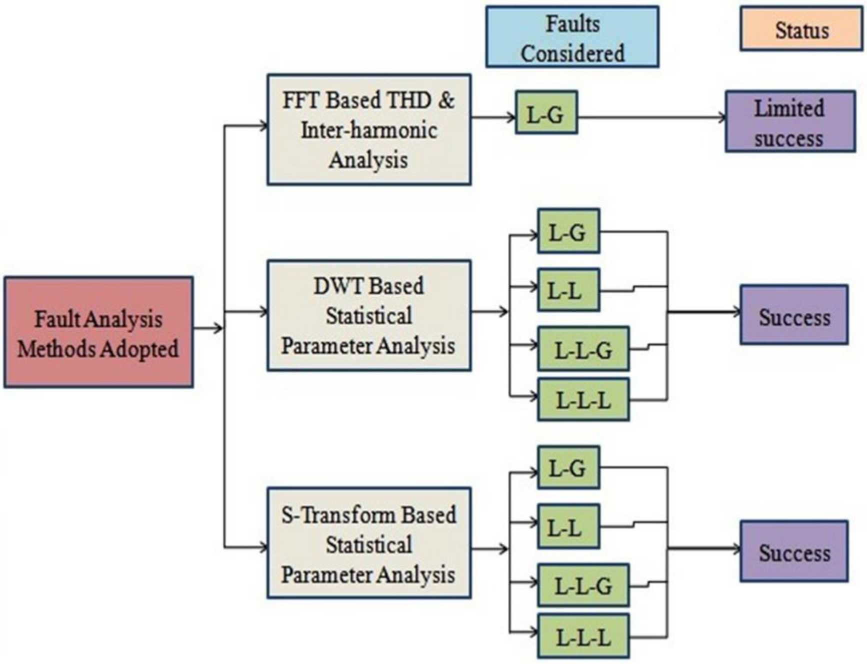

Fig. 1.1: Detailed Workflow of the Research

1.5 Thesis Organization

This thesis has been organized in the following manner.

Chapter 1: This introductory chapter provides a brief introduction to microgrid networks, faults of microgrid networks considered in this research work, Objective of the work and a detailed workflow of this work.

Chapter 2: This chapter outlines a brief overview of different types of microgrid networks, modes of operation of microgrid networks, various standard microgrid models and general structure of a microgrid network along with its basic control structure. Second half of this chapter introduces the various signal processing tools and statistical parameters utilized in this thesis to achieve the goals of classifying the type and locating faults in microgrid environment. Discrete Wavelet Transform and Stockwell Transform based statistical approaches are detailed herein.

Chapter 3: This chapter illustrates the application of statistical analysis using Fast Fourier Transform (FFT) and Discrete Wavelet Transform (DWT) on outgoing currents from generator buses to detect line-to-ground (L-G) faults in an IEEE 14-bus microgrid system, where traditional fault detection methods prove inadequate. Here, the limitations of FFT and reason for its incompatibility are also discussed in detail.

Chapter 4: Here, a technique for pinpointing fault locations and differentiating fault types in a microgrid network. It employs kurtosis analysis based on the Stockwell Transform (S-Transform), followed by the development of a specialized algorithm to accomplish these tasks.

Chapter 5: This chapter presents an approach for locating faults and classifying fault types in a microgrid network. It utilizes skewness analysis derived from the Stockwell Transform (S-Transform), leading to the creation of a tailored algorithm for these objectives.

Chapter 6: This chapter introduces a fog computing framework incorporating artificial neural networks for remote fault monitoring in IEEE standard 14 bus microgrid network. It leverages Discrete Wavelet Transform (DWT) based statistical analysis of currents to build a dependable rule-based system, enabling accurate detection of Line-to-Ground (L-G) and Line-to-Line (L-L) faults at load buses. The approach delivers consistent results under diverse fault resistance conditions while minimizing cloud storage requirements.

Chapter 7: This concluding chapter reviews the key results achieved by the various fault classification and localization algorithms proposed in this thesis. It provides a concise overview of the conducted research and compares the proposed fault detection algorithms with established algorithms from the literature review. The chapter also explores potential future directions and possible extensions of this research toward the end.

Chapter 2

A Brief Review on Microgrid and Methods of Fault Analysis in Microgrid

First part of this chapter presents a concise examination of microgrid systems, their essential elements, and their influence on contemporary energy frameworks. Second part outlines an overview of the statistical parameters and signal processing tools utilized in this work along with a brief description of an application of this method.

2.1 Introduction

Microgrid consists of a set of distributed energy sources and loads confined to a small region, which acts as a single controllable entity with respect to the grid, having a distinct electrical borderline. It is capable of working either connected the traditional power grid in grid connected mode or on its own in island mode. However, widespread introduction of microgrid will bring forth its own sets of technical challenges. The main challenges are to deal with the significant impact on existing networks created due to the deployment of number of DERs and design a proper protection schemes which can operate satisfactorily in the much lower voltage and currents levels present in the microgrid environment. Unlike traditional power networks; generators, energy storage facilities and loads are present at all the levels of the microgrid network. Generation, distribution and consumption can occur at any level of a microgrid network and direction of power flow is also uncertain. Complete understanding of a microgrid operation is still at very early phase. In this chapter a succinct overview of microgrid networks is provided, examining their standard form of structures, operating mechanisms and main elements. It further outlines the recent advancements in the field of fault detection in microgrid environment and a brief description of the workflow of the research work presented in this thesis.

2.2 Microgrid Network

Evolution in the field of Distributed Energy Resources (DER) and energy storage system, are making microgrids extremely popular for enhancing overall reliability and resilience of conventional power networks. A microgrid comprises a localized group of distributed energy sources and loads within a defined electrical boundary, operating as a unified, controllable unit relative to the main grid. It can work either in coordination with the conventional grid in grid-connected mode or autonomously in island mode. However, the widespread implementation of microgrids introduces some unique technical challenges. Key issues include managing the substantial effects on existing networks due to the integration of multiple DERs and developing effective protection strategies that perform reliably at the lower voltage and current levels typical of microgrid environments. Unlike conventional power systems, microgrids feature generators, energy storage units, and loads at all network levels, with generation, distribution and consumption occurring at any level and power flow directions being unpredictable.

2.2.1 Types of Microgrid Networks

Microgrid networks can be classified in three broad categories, depending upon the DER units and the type of loads present. These are: DC Microgrid, AC Microgrid and Hybrid Microgrid.

DC Microgrid Network

DC microgrids exhibit the least energy loss compared to other microgrid types. Fig. 1.1 illustrates the fundamental layout of a DC microgrid, capable of functioning at various DC voltage levels. Connection with the grid may be done through a rectifier unit [71 - 73]. Various sources like PV farm, wind farm and battery storage units may be connected to the common DC bus through suitable DC/DC link or rectifier unit. Different types of loads may be joined with the common DC bus through DC/DC links. Control is simpler because reactive power is absent, requiring only voltage amplitude regulation to connect DC sources to the bus. The primary benefits of DC microgrids include the elimination of energy conversion stages and the lack of need for phase or frequency synchronization. Their use, however, is restricted to applications involving low voltage levels.

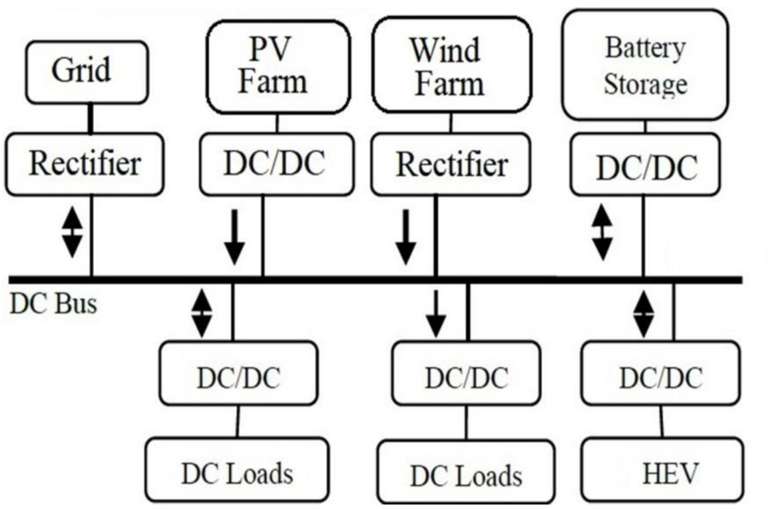

Fig. 2.1: Basic Structure of a DC Microgrid Network

AC Microgrid Network

Fig. 1.2 given below shows the basic structure of an AC Microgrid network. Main advantage of this type of microgrid is that local loads can draw power from it and excess power can also be injected back to the main conventional grid [13]. Different voltage levels can be achieved through the use of transformers. Perfect synchronization of phase angle and frequency is needed for the operation of AC microgrids. High power applications need this type of microgrids. Here, DC sources such as PV farms may be connected to the common DC bus using rectifier units. Connection with wind farm and grid may be achieved through suitable transformers. Various loads may be connected with common AC bus through suitable transformers as required.

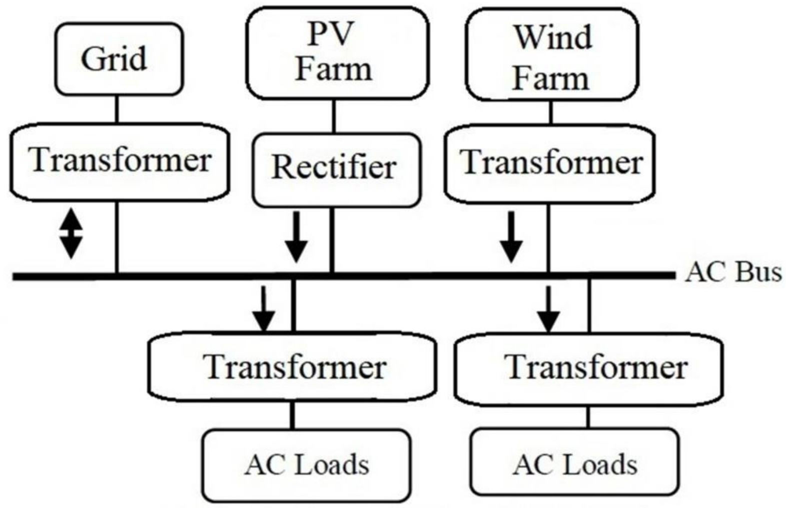

Fig. 2.2: Basic Structure of a AC Microgrid Network

Hybrid AC-DC Microgrid Network

Fig. 1.3 given below shows the basic structure of a hybrid AC-DC microgrid [54, 57]. This type of microgrid network is a combination of AC and DC microgrid. So, it has two distinct portions. Direction connection between the AC network and the conventional grid is present. An interlinking converter joins the DC section of the microgrid network with the conventional power grid. These types of networks are designed by considering the flow of power, nature of loads and cost. This type of microgrid network can serve both AC and DC loads. All the existing standard forms of microgrid are of this type.

The main difference between hybrid AC-DC microgrid and an only DC microgrid or AC microgrid is that in this particular type of microgrid network both common AC as well as common DC bus exists. Both sources and loads can be connected to both common AC and DC bus. A rectifier block allowing power flow in both the directions, maintains the connection between the common AC and DC bus. The main grid may be connected with the common AC bus through a suitably chosen transformer, to facilitate grid connected mode of operation. Any green energy sources producing power in AC such as wind farm, needs to be connected with the common AC bus through a transformer. Whereas, sources producing power in DC such as PV farm, needs to be connected with the common DC bus through a DC/DC link.

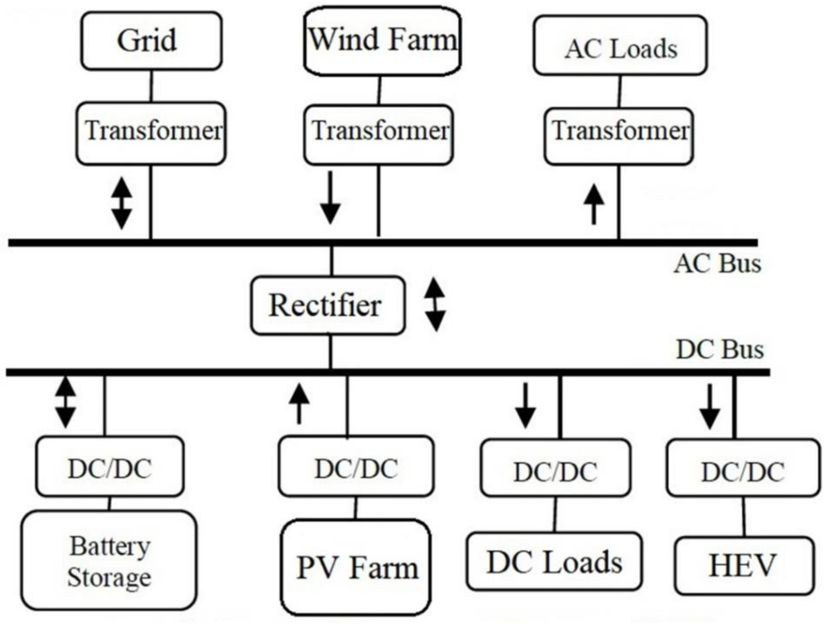

Fig. 2.3: Basic Structure of a Hybrid AC-DC Microgrid Network

2.2.2 Modes of Operation

IEEE 2030.7-2017 describes the different operating modes for a microgrid network in a comprehensive way. This standard summarizes microgrid operation to two steady state (SS) operating modes and four types of transitions (T), as shown in Fig. 1.4.

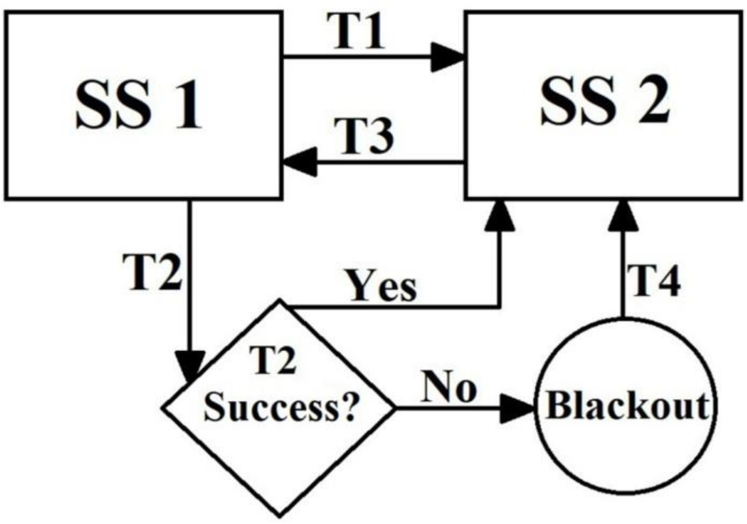

Fig. 2.4: Microgrid Operating Modes and Control Flow Diagram

The operating modes according to IEEE 2030.7-2017 are as follows:

- **Steady State Grid Connected (SS1):** At this mode, the microgrid network is connected to the traditional grid. Microgrid is capable of providing services to the grid, such as peak shaving, valley filling and reactive power control. The microgrid controller provides a single communication point to access all of these services.
- **Steady State Island (SS2):** At this mode, disconnection of the microgrid from the traditional power network is achieved. So, the microgrid network operates on its own (formally known as "islanding"). A continuous balance needs to present between loads and local generation and energy storage facilities. If the microgrid has enough generation capacity then it can be operated in this mode indefinitely. Island mode demands different settings for the protective devices than in grid connected mode due of the much lower fault current levels and possible changes in direction of power flow within the network. Stable operation in island mode needs load management, in case the generation fails to meet the net load demand, or if the energy storage systems do not have enough reserve to meet power demand for a specific time-frame. Microgrids which are only having solar or wind energy sources generally need energy storage systems to get a buffer between the variable energy sources and load. It will also require the ability to cut-down generation, if storage is full and generation exceeds the load, in order to prevent high-frequency or high-voltage problems.
- **T1 – Transition from Grid Connected to Steady State Island (Planned):** Microgrid may be operated in island mode even when the traditional power grid is available. It can be done for several reasons such as to test the network for a scheduled power outage, or simply for economic reasons. T1 demands a smooth transition from grid-connected to island mode. Auxiliary generation is initiated to achieve equilibrium between load-demand and available power generation. After that microgrid is disconnected at the 'point of interconnection (POI)'. At the same time local generation should also switch from 'grid-following mode' to 'grid-forming mode'. Protective devices which generally operate in a particular direction may become bi-directional during island mode and it is extremely important that settings on these devices should be tweaked accordingly.
- **Grid Connected to Steady State Island – Unplanned (T2):** This mode of operation takes place if in the event of a fault in the main grid; the microgrid has the ability to disconnect itself and transit into islanded mode without interruption of power supply to the loads with the help of local generations. T2 is somewhat easier in case of small dedicated microgrid networks but difficult for large microgrid networks. Sometimes, the critical loads are disconnected during this process until additional power sources are brought online. Similar to the planned island, protective equipments require adjustments.

- **Steady State Island Reconnect to Grid (T3):** At this mode, changeover occurs from island mode of operation to grid-connected mode through successful reconnection. Phase angle as well as frequency of the ‘grid-forming’ generator present in the microgrid network must be matched with that of the traditional power grid to obtain proper synchronization. After the reconnection is complete, the ‘grid-forming’ generator gets switched to ‘grid following’.
- **Black Start into Steady State Island (T4):** In this mode of operation a microgrid is restarted in island mode after experiencing black-out. T4 needs the microgrid network to be detached from the main grid at the POI. If the microgrid controller fails to deal with an unexpected power outage of the main power grid and initiate stable transition (T2) to island mode then T4 is experienced. T4 can also happen if there exists insufficient generation or energy storage reserve for continuation of supply to loads and consequently it has to be shut down.

2.3 Standard Microgrid Networks

The dynamics of a microgrid network are highly variable, regardless of whether it operates in grid-connected or island mode. The addition or removal of a Distributed Energy Resource (DER) or load can occur at any moment. Such network changes necessitate adjustments in power generation, load distribution, control mechanisms, and protection strategies. Standardized frameworks are invaluable for studying and addressing the complex technical challenges related to the operation, control, and protection of microgrid systems. Three widely adopted standard microgrid networks include the IEEE 9-bus microgrid network, the IEEE 14-bus microgrid network, and the IEC 61850-7-420 standard microgrid network. Further details about these networks are discussed in the subsequent section.

2.3.1 IEEE 9 Bus Microgrid Network

This network is derived from the conventional IEEE 9 bus network and depicted below in Fig. 1.6 [7]. It has been modified into a microgrid network by reducing the line lengths and strategically introducing various DERs [71]. Alternator G1 is taken as the reference generator and bus B1 is considered as the swing bus. Three alternators present in this network are of three different types. The hydro-alternator is connected to bus B1, gas-turbine is at B2 and the coal-fired type alternator is present at B3. Capacity of the hydro-alternator, gas-turbine and the coal-fired type alternator is 250 MW, 255 MW and 230MW respectively. Automatic voltage regulator is present with each of these alternators has a turbine. Solar PV systems are connected at buses 5 and 9, doubly-fed induction generator based wind farms are at buses 6 and 8. These sources are connected to the microgrid through a transformer of rating 0.4 / 230 kV. Power rating of the PV Farm A and B are 69 MW and 49 MW respectively. The Wind Farm has power rating of 50 MW. An Energy Storage System (BESS) is connected with bus 1.

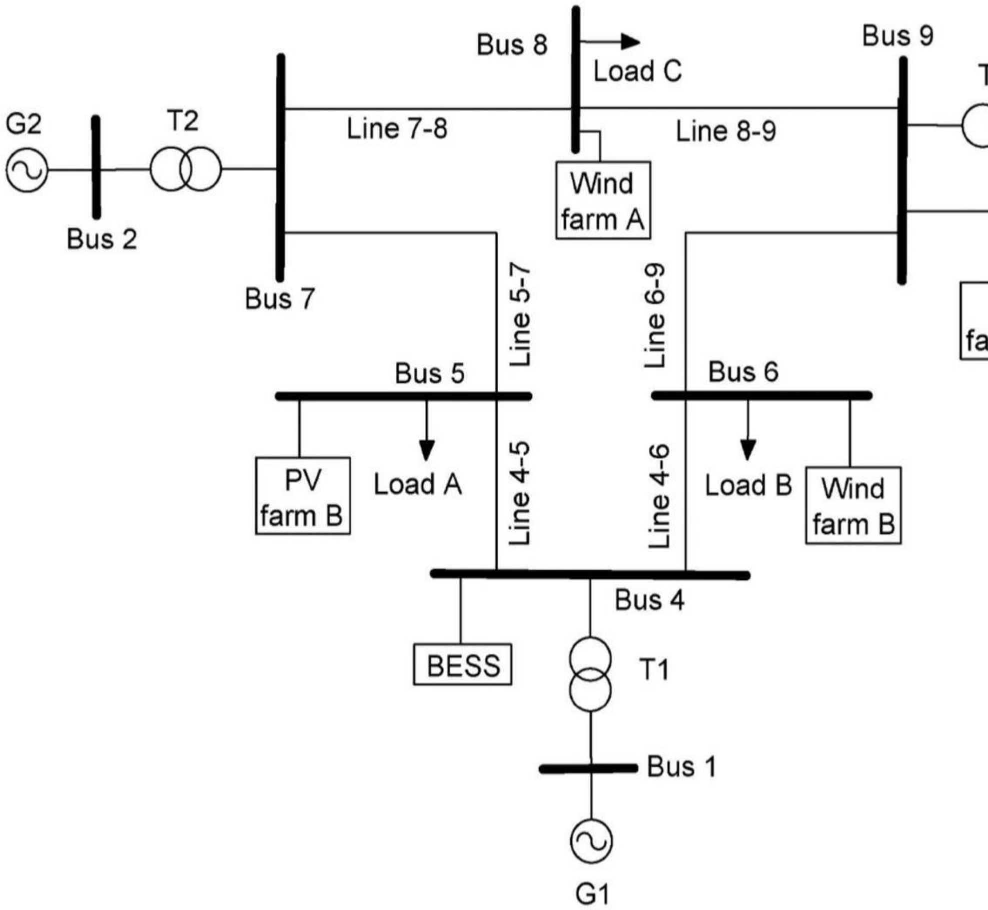

Fig. 2.5: IEEE 9 bus microgrid network

2.3.2 IEEE 14 Bus Microgrid Network

IEEE standard 14 bus microgrid system is shown below in Fig. 1.5 [12, 14, 68]. There are four different types of sources present in this microgrid network. Bulk-generator is connected at bus G-13. At G-12, PV system is present. Diesel generator - 1 (DG-1) and diesel generator - 2 (DG-2) are connected at G-8 at G-3 respectively. Loads are of four different types. Bus B-10 has nonlinear bulk load, B-6 has furnace, B-1 has battery charging system, B2 has linear load and B-3 has linear load 1 connected to it. Length of transmission lines connecting one bus to its adjacent bus is 1 Km. Operating voltage and frequency is kept at 400 Volt (line to line) and 50 Hz respectively. Bulk generator bus is considered as the swing bus. Bulk Generator is rated at 100 MW, P-V system has a capacity of 40 MW and both the diesel generators are rated at 50 MW. This standard model is widely used in the work presented in this thesis.

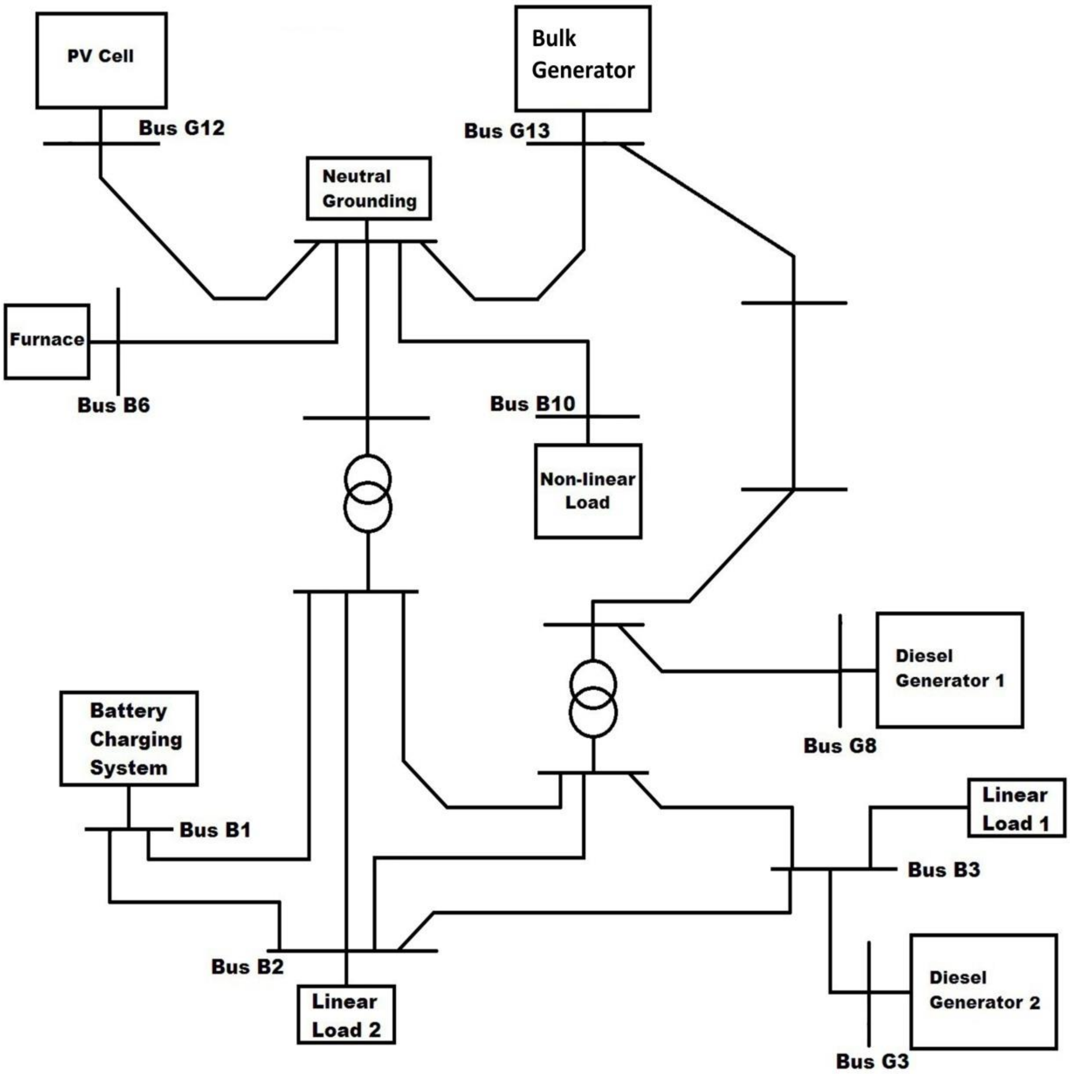

Fig. 2.6: IEEE Standard 14 Bus Microgrid Network

2.3.3 IEC 61850-7-420 Standard Microgrid Network

In IEC 61850-7-420 standard network, all branches contain energy source and load, and the main feature of this network is that the structure can be altered as per requirement network with the help of combinations of relays. Fig. 1.7 given below, shows IEC 61850-7-420 standard microgrid network [72]. The power flow, load sharing, stability parameters and protection schemes need to be adjusted accordingly. In this network structure, various DGs and loads can be connected to and disconnected from the microgrid followed by some minor adjustments. In case CB4 is disconnected, then CB5 has to be closed for keeping the integrity of the network. For protection of the microgrid against failures, line connecting Load 1 and 2 (under the protection of CB5) forms a loop structure if needed. The whole network structure and the relationship between the microgrid components change significantly. This would require major adjustments on the flow of power, sharing of load, stability parameters and schemes for protection to ensure satisfactory and safe operation.

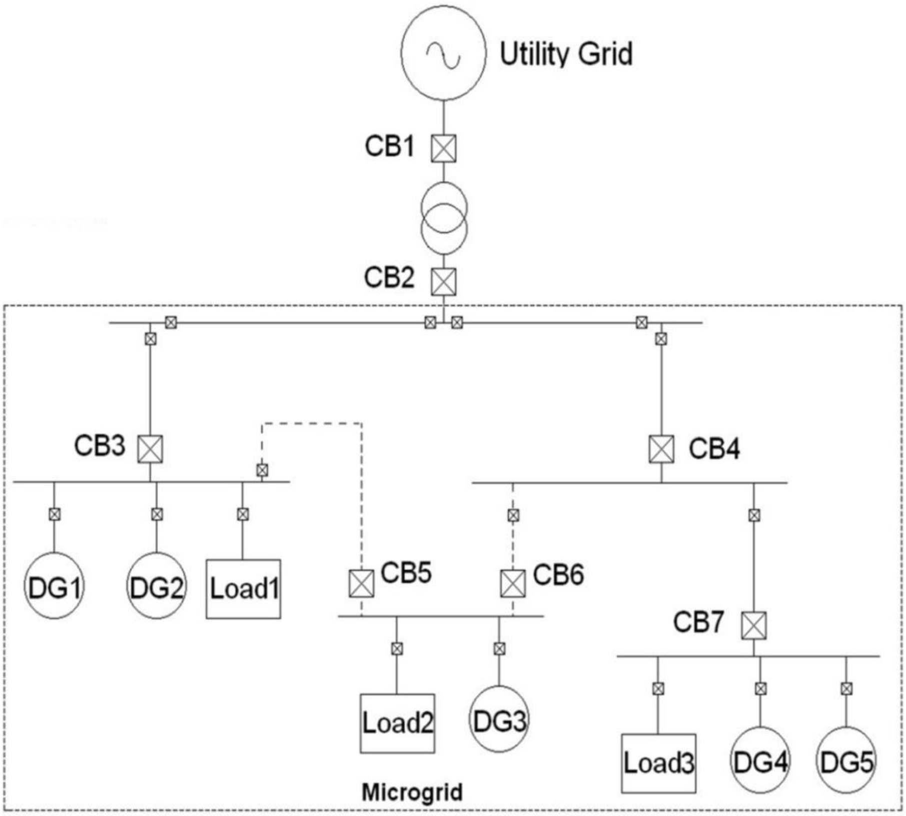

Fig. 2.7: IEC 61850-7-420 standard microgrid network

Therefore, a centralized microgrid management system which implements extensive communication with microgrid components is required. This management system will monitor DGs, loads, storage devices along with protection equipment and assign necessary parameters for respective component. The continuous monitoring and adjusting microgrid parameters on the fly help implement a dynamic management system required by the highly variable nature of the microgrid.

2.4 General Equipments of a Microgrid Network

Identification of the energy sources, energy storage systems, load management, and automated distribution system equipments which are present in the microgrid is of paramount importance for understanding the operation of the microgrid controller [1, 5 - 8].

- **Energy Sources:** Energy sources present in microgrid networks are generally photovoltaic systems (PV), diesel generators, fuel cells, wind generators etc. Now a day, behind-the-meter (BTM) sources, like commercial or residential PV systems are also being utilized. One of the active energy sources act as the ‘grid-forming’ generator. It sets operating frequency and voltage level of the network. A traditional rotating alternator or a battery-based inverter is used as the ‘grid-forming’ generator. Solar systems and wind generators generally do not play the role of ‘grid-forming’ generator due to their highly variable nature.

- **Energy Storage:** Energy storage facilities act like a bridge between generation and load management. Battery systems, can also serve as energy sources, when there is a provision of recharging them from other sources. Thermal energy storage, such as controllable water heaters or ice storage (for commercial cooling), can also help stabilize the grid, although these cannot actively contribute electric power to the microgrid. Table 2.1 given below shows the classification of energy storage systems on the basis of their operating principles.

Table 2.1 Classification of Energy Storage Systems on the basis of Operating Principle

Sl. No.	Types of Energy Storage	Examples
1.	Mechanical	• Flywheel. • Compressed air • Hydro pump
2.	Electrical	• Super conducting Magnetic Energy Storage • Capacitor bank
3.	Electrochemical	• Secondary batteries (lead acid, NiCd, NaS, etc.) • Flow batteries (redox flow, hybrid flow) • Super capacitors
4.	Chemical	• Fuel Cell
5.	Thermal Systems	• Heat storage

- **Load Management:** It is the key component of balanced operation of a microgrid network, because proper load management ensures a balance between generations and the load demand. Load management can be of various types such as utility demand response techniques (e.g. water heater and air conditioner curtailment or thermostat control), remote-disconnect meters at residences and small commercial entities, active load disconnects at large commercial and manufacturing facilities, and feeder sectionalizing foe the purpose of isolating entire group of users based on their location. Information must be fed to the microgrid controller regarding the loads which are present at different points in the network. A priority schedule of the most critical loads should also be maintained, in case an event of limited generation is faced.

- **Automated Distribution System Equipment:** Two purposes are generally served by automated distribution system equipments present in a microgrid network. Firstly, they perform micro-level load management, such as initiating ‘rotating blackouts’ in case a shortage in generation is faced. Secondly, they also play the role of sensing as well as protective equipment. The electrical characteristics vary considerably, between islanded mode and grid-connected mode of operation because flow of current in grid-connected mode is always unidirectional - from substation to load, whereas, in steady state island (SS2) mode of operation, flow of current can be bidirectional depending upon the energy sources available at a given time. Hence, the protective devices should possess the ability to handle the bidirectional current flow in case the microgrid network experiences a changeover from grid-connected to island mode or vice-versa.
- **Communications and Cyber Security Issues:** For proper operation of a microgrid network, microgrid controllers need to communicate with a number of devices such as inverters present in PV systems to residential thermostats. This communication system poses the greatest challenge in design and operation of a microgrid network mainly because of great variety of communication technologies (e.g.: fiber, PLC, cellular etc.) and also of standards and protocols (e.g.: Modbus, DNP3, IEC 61850 etc). The protocols generally employed in the network are also very much different than the consumer-oriented behind-the-meter (BTM) protocols (e.g.: WiFi, Ethernet etc.). Microgrid controllers can either be self-contained or hierarchical in nature. In both the cases interoperability is very much needed. Cyber security is also very closely related to communications and interoperability. Devices should have the ability to figure out whether a request for status or control is valid or not. It should also ensure that the communication signals are secure and can only be decrypted by the appropriate controller. Hence, cyber security needs to be built into the software process as early as possible.

2.5 Basic Control Structure of Microgrid Network

Basic Control structure for microgrid operation generally consists of three stages or layers [2].

- **Primary Control:** Output voltage regulation through inverters and sharing of load amongst the inverters is performed at primary level of control. This level of control is required for maintenance of economy and enhancing the overall reliability of the network.
- **Secondary Control:** Deviations in voltage waveforms and frequency caused at primary control level is rectified with the help of secondary control. Load demand forecasting and adjustment of output from the DERs are performed.

- **Tertiary Control:** Exchange of power between different consumers is managed at this control level. It is used to achieve the economic-emission reliability dispatch. Optimization-based control techniques are utilized to implement this control.

2.6 Recent Advancements in Fault Diagnosis in Microgrid Network

Scientists have long employed highly effective methods for detecting, categorizing, and pinpointing faults. Various algorithms and network structures have been utilized by researchers to achieve these objectives. In a modern power network, a microgrid, if utilized properly, can increase the overall reliability of the system to a great extent but fault detection inside a microgrid environment comes with its own set of hurdles and most the existing techniques fail to work satisfactorily. So, in recent times, researchers focused their attention towards identification and mitigation of faults especially in a microgrid network. This section elaborates on the various articles utilized to develop the topologies and methodologies employed in this thesis for creating fault diagnosis techniques. It also underscores the key contributions of researchers and their relevance to this study.

A new fault location topology implemented in DC microgrid systems based on the selective switching frequency of the semiconductor switches and the amplitude of input DC voltage is presented by **E. Dehghanpour** et al in [1]. Differential current based fault detection and location in a multiple photovoltaic based DC microgrid system is proposed by **S. Dhar** et al [2]. **D. Kar** et al had introduced a strategy for identification of faulty load bus in a multi-bus power system by monitoring the inter-harmonic and sub-synchronous inter-harmonic operating point in P-δ plane in [3]. **D.K. Ray** et al had proposed a method of steady state harmonic stability analysis in IEEE 14 bus system for fault at generator bus [4]. Fault detection system based on voltage, instead of current to trigger the microgrid disconnection procedures had been introduced by **G. M. S. Azevedo** et al in [5]. **G. Madingou** et al (2015) had proposed a method for fault detection and isolation in a DC microgrid using a central processing unit [6]. **T. Aziz** et al investigated post-fault voltage recovery performance with battery-based energy storage system in a microgrid [7]. **S. Mirsaedi** et al presented the structure of hybrid microgrids with a detailed overview of available protection schemes and devices for AC and DC subgrids [8]. Interaction of the microgrid and main network by using unidirectional fault current limiters had been carried out by **E. Farjah** et al [9]. **S. Wen** et al developed an ensemble forecasting model based upon extreme learning machine algorithm for predicting short term power fluctuations to control alternators running parallel with renewable energy sources [10]. A fractional-order dynamic-error-based fuzzy petri net for detection of DC side faults in an AC / DC microgrid network consisting of PV energy conservation has been proposed by **J. L. Chen** et al [11]. **Y. M. Markawa** et al utilized voltage signals from the distributed generator terminals of standard microgrid systems in real time digital simulator environment and presented a novel technique of islanding detection [12]. **M. Manohar** et al proposed a method to discriminate PV array faults and symmetrical line faults in a microgrid with the help of voltage and current signal recorded from the relaying buses [13]. An efficient interface between the microgrid and main network had been introduced with the use of unidirectional fault current limiter by **T. Ghanbari** et al [14]. FFT and wavelet decomposition based harmonics assessments have been observed using current signature analysis for fault diagnosis [15 – 16].

Fuzzy set theory based fault tree analysis has been applied in wind energy system for the purpose of reliability assessment considering operational failures and errors in the fuzzy environment by **I. Akhtar** et al [17]. **P. D. Raval** et al used Particle Swarm Optimization based training of Artificial Neural Network assisted by multiresolution Wavelet Analysis (MRA) and statistical feature extraction to identify faults in EHV Transmission Lines [18]. **M. Ikhide** et al proposed a transient and non-unit based protection technique for DC grids using the rate of change of associated travelling wave components when fault occurs to distinguish between internal and external faults [19]. Hilbert – Huang Transform and Extreme Learning Algorithm have been utilized to detect islanding condition in a distribution system consisting of distributed generators by **M. Mishra** et al [20]. **A. Ali** et al proposed an observer based fault detection filter (FDF) to detect faults in a power system network model consisting of a power generating unit and transmission and distribution network formed in state space [21]. Relevance Vector Machine (RVM) based fault classifier has been used for development of an algorithm to classify and detect faults in power transformers by **D. Patel** et al [22]. Differential current based fault detection and location in a multiple photovoltaic based DC microgrid system is proposed by **S. Dhar** et al [23]. **Manohar M.** et al had introduced a reliable protection scheme for a PV integrated microgrid using ensemble classifier approach which is insensitive to the biasness of individual classifier and dimension of dataset [24]. **B. M. Eid** et al examined architecture of microgrids and its classifications during island mode of operation [25]. **M. J. Morshed** et al has proposed a fault-tolerant control paradigm for a microgrid connected doubly-fed induction generator based wind farm [26]. Power estimation has been done with certain probabilistic boundary condition and fault diagnosis has been carried out for power distribution system by **H. Nademi** et al [27]. Current measurement is a common technique for fault detection in nearby buses and it is also used for proper section of current limiter by **A. Heidary** et al [28].

N. Mukherjee et al presents a MATLAB-simulated study on the rapid detection and classification of symmetrical and unsymmetrical faults in grid-connected wind systems, utilizing discrete wavelet transform (DWT), total harmonic distortion (THD), inter-harmonics, and Stockwell transform (S-transform) for statistical parameter analysis to assess unbalanced conditions and harmonic presence [29]. **D. Li** et al proposes a high-speed, robust fault detection method for VSC-based DC power systems using an adaptively adjusted S-transform, achieving fault detection within 0.3 ms by leveraging high-frequency detection for rapid response and low-frequency screening to distinguish faults from other transients, validated through OPAL-RT simulations and a point-to-point experimental DC test bed, with superior performance compared to wavelet transform and short-time Fourier transform methods [30]. **G. Ahamad** et al proposed a method of power system fault detection in presence of thyristor controlled reactors in the system with the help of median based fault index, derived from the S – matrix of the voltage current [31]. A protection scheme for the transmission lines against various types of faults using a fault index dependent upon S – Transform based medians of current signals obtained from the nodes of IEEE 34 node test system is presented by **S. R. Ola** et al [32]. **A. Ghorbani** et al has shown methods of fault detection for double circuit lines based upon negative sequence circuit of the transmission line system, which are affected by neither fault resistance nor mutual coupling [33 - 34]. Non-standard characteristics of over current relay for minimum operating time and maximum protection level has been presented by **R. Hemmati** et al [35]. **H. Mehrjedi** et al proposed an algorithm for transmission line protection based upon active power calculation of the buses using synchro-phasors to eliminate the effects of fault resistance and unified power flow controller (UPFC) [36]. A method of fault detection in transmission lines connected to wind farms based upon combination of distance and differential protection has been presented by **M. S. A. Ghorbani** et al [37]. Fault type identification in advanced series compensated transmission lines have been performed using artificial neural network and support vector machine by **B. Vyas** et al [38]. **S. Agarwal** et al proposed a method of bearing fault detection of induction motors using Hilbert Transform and High Frequency Resolution Technique [39]. **M.N. Eskander** et al has discussed mitigation of voltage dips and swells in grid connected wind energy conversion systems along with an investigation of active and reactive power behaviors during and after fault recovery [40]. A study of advanced signal processing technique for the classification of different power quality disturbances using pattern recognition based upon Wavelet Packet Transform has been presented by **B.K. Panigrahi** et al [41].

W. Elmasry et al has shown fault detection in practical power grids based upon detection diagnosis of anomalies which were validated through two most popular models of anomaly detection [42]. Detailed study of different A.I. based methods of detecting power line faults including the scopes of usage of unmanned aerial vehicles for real – time monitoring purposes has been performed by **S. Y. Wong** et al [43]. **N. Mayadevi** et al presented a fault diagnosis methodology for the drive systems of induction motors using fuzzy – logic based algorithms which are capable of working satisfactorily under various loading conditions [44]. **D. Kar** et al developed a method to detect faults in a multi-bus power system, specifically identifying generator bus faults in the IEEE 14 bus system, by analyzing sub-synchronous inter-harmonics and inter-harmonic operating points in the P-δ plane through steady-state harmonic stability analysis [45 - 46]. Voltage based fault detection system to trigger the disconnection process of microgrid had been introduced by **G. M. S. Azevedo** et al where the disconnection process has been triggered by voltage based fault detection [47]. **S. Mishra** et al have proposed an S-Transformation-based probabilistic neural-network classifier to detect disturbances in power quality [48]. **Z. He** et al discussed a novel technique of fault perception and categorization in EHV transmission lines using wavelet transformation-based singular value decomposition and Shannon entropy [49]. Unique time determinism and suitable refresh rate for phasor measuring units are utilized to detect faults of active distribution networks by **M. Pignati** et al [50]. S – Transformation and artificial neural-network-based hybrid classifier and a rule-based decision tree are applied to detect various types of disturbances in power quality by **R. Kumar** et al [51]. **C. Ling** et al. presented a discrete wavelet transform-based triggering algorithm to detect a ground fault in single-phase lines by observing zero-sequence voltage under normal along with faulty conditions [52]. **K. Hatipoglu** et al had implemented faults in a microgrid environment with MATLAB-based GUI [53]. An effective association between the microgrid and traditional power grid had been done through one directionnal fault current limiter by **T. Ghanbari** et al [54]. 'Hilbert – Huang Transform' and 'Extreme-Learning Algorithm' is used for detecting islanding in a distribution network having distributed generators by **M. Mishra** et al [55]. **M. Ikhide** et al introduced a 'transient and non-unit' based protection technique for DC grids employing the rate at which the related traveling-wave components change when an abnormal condition happens, for identifying internal and external faults [56]. Controlled series inductances are put at the points of common coupling between high power microgrid and main power grid to enhance fault ride-through capability of a microgrid by **S. I. Gkavanoudis** et al [57]. **Y. Tan** et al used S – Transform for fault identification of different analog circuits [58]. S – Transformation is used to find out high resistance faults at the time of power swing using by **N. Z. Mohamad** et al [59]. **N. Roy** et al presented an S-Transformation-based rule set for the identifying faults at overhead transmission lines during unbalanced conditions by extracting waveforms of voltages and currents from both sending and receiving ends [60]. Training and testing of artificial neural-networks are done through features obtained from S-Transformation to detect high impedance faults of distribution lines by **P. Routray** et al [61]. Features from the signals of current and voltage are obtained through S-Transform and utilized to identify faults in power distribution systems by **G. G. Santos** et al [62]. **S. Devi** et al presented a discrete wavelet transform-based methodology to detect various kinds of faults occurring at transmission lines [63]. **M. Choudhury** et al detected faults through Discrete Wavelet Transform (DWT) on the fault currents and evaluation of mean of approximate coefficients from the phase-signals [64]. FFT and wavelet-based current signature analysis got utilized for the diagnosis of faults by **A. Chattopadhyaya** et al [65]. **M .M. A. Mahfouz** et al proposed an algorithm employing the data available through the communication facilities to identify faulty feeder [66]. Strategy of DC microgrid protection using ensemble classifiers having immunity against weather variations is put forward by **S. P. Tiwari** et al [67]. **F. B. Reis** et al proposed a multi agent approach divided in online and offline mode of identification of fault in DC microgrids [68]. **S. Banerjee** et al proposed a Discrete Wavelet Transform (DWT) method to identify power system transients in microgrids by analyzing performance indices such as absolute values, standard deviations, and energy of wavelet coefficients across high, medium, and low levels, effectively detecting events like faults, islanding, load changes, and capacitor switching [69]. **D. Salomonsson** et al introduced a protection system design for low-voltage (LV) DC microgrids, which connect distributed energy sources and sensitive loads, leveraging insights from existing DC systems while addressing unique challenges posed by bidirectional AC grid converters, analyzing operational principles, technical specifications of protection devices, fault-detection techniques, and grounding methods through simulations that confirm the feasibility of current devices but highlight difficulties in detecting high-impedance ground faults [70]. **R. Mohanty** et al proposed a noniterative fault location technique using a probe power unit (PPU), which accounts for damping frequency and probe current attenuation as functions of fault distance and damping coefficient, demonstrating improved accuracy for high-resistance faults in both radial and looped topologies compared to methods assuming equivalence between system natural frequency and damped resonant frequency [73]. **W. Qiu** et al introduced a novel approach for automatically recognizing and classifying power quality (PQ) disturbances using a modified S transform (MST) with a Kaiser window for enhanced time-frequency energy concentration, combined with a parallel stacked sparse auto-encoder (PSSAE) that leverages both time-frequency matrices and Fourier transform spectra for feature extraction, followed by dimensionality reduction, visual analysis, and classification via a softmax classifier, with experimental validation across various single and combined signal types confirming its effectiveness and robustness [74]. In the evolving landscape of smart grids, protecting AC microgrids (MGs) is challenging due to bidirectional power flow and reduced fault currents from the main grid, rendering traditional Over Current (OC) relays less effective against High Impedance Faults (HIFs), prompting **E. K. Bindumol** et al to review diverse fault detection and control strategies to enhance the reliability and efficiency of AC MG systems [75]. **S. Nanda** et al proposed a novel Artificial Neural Network (ANN)-based approach for swift and precise fault detection, location, and isolation in AC power systems, leveraging ANN’s pattern recognition to overcome the limitations of traditional methods, validated through simulations on a diverse dataset of fault scenarios, load variations, and system configurations, achieving superior speed, accuracy, and adaptability with minimal infrastructure changes [76]. **P. Criollo** et al presented a Sliding Mode Observer-based fault detection method for photovoltaic systems in AC hybrid microgrids, comparing observer responses with system behavior to generate residuals for fault identification across normal, incipient, and random fault scenarios, validated through MATLAB/Simulink simulations on a microgrid benchmark with photovoltaic panels, battery storage, and varied loads, setting the stage for future hierarchical control and fault tolerance advancements [77]. A robust fault detection and classification method for AC microgrids using ensemble empirical mode decomposition (EEMD), employing a two-stage process that first detects faults and then identifies their types by decomposing current signals into intrinsic mode functions and residuals, validated through MATLAB/Simulink simulations on a modified IEEE 13-bus microgrid model, demonstrating effective system protection against various fault conditions is presented by **S. K. Prince** et al [78]. **M. Mola** et al presented a distributed fast fault detection approach for a DC microgrid with interconnected distributed generation units (DGUs), utilizing local fault detectors that leverage subsystem states and neighboring measurements to form an effective fault detection network [79]. **W. Miao** at al proposed a state-space modeling-based method for detecting and locating series arc faults in DC microgrids by analyzing the topology and operation of power converters, developing equivalent circuits for normal and fault conditions, and using residuals of inductor current and capacitor voltage to identify faults, with over-threshold integration to mitigate load transient effects, validated through simulations and experiments on a two-branch DC microgrid [80]. **F. Chang** et al developed a transient analysis for ungrounded islanding microgrids with multiple inverter-based distributed generators (IBGDs) under varied control strategies and fault types, proposing a fault detection and location method using two-terminal measurements of zero-sequence, negative-sequence, and phase currents, which outperforms conventional single-terminal over-current protection without requiring extensive data exchange, as validated through simulations [81]. **M. Takhellambam** et al introduced a novel online fault detection and identification method for grid-connected microgrids using discrete wavelet transformation (DWT) and multi-resolution analysis (MRA) to extract detailed coefficients for various fault types (e.g., line-line, line-to-ground, double line-to-ground) under diverse parameters, validated through extensive MATLAB/SIMULINK simulations of a microgrid with a PV power plant and battery storage, demonstrating robust and effective fault detection and classification [82]. **Z. Ali** et al examined cutting-edge fault management strategies for DC microgrids, reviewing advancements in fault detection, location, identification, isolation, and reconfiguration, while outlining future trends and challenges in enhancing system reliability [83]. **A. Sardashti** et al explored fault detection in an islanded AC microgrid benchmark, leveraging its advantages over conventional power systems, by proposing a sensor fault detection method that uses online recursive model estimation and linear Kalman filters for residual generation, enabling a sequential change detection unit to distinguish between normal operation and fault conditions [84]. **K. F. Krommydas** presented a model-based algorithm for fault detection and isolation in DC microgrids, demonstrating its ability to accurately identify and classify faults, with simulation results confirming its effectiveness as a robust protection scheme design [85]. **A. Bhuyan** et al proposed an innovative approach for detecting and classifying fault disturbances in diverse operating conditions, using wavelet and Hyperbolic S-transform to extract statistical features for a compact dataset, processed by decision trees (DT) and support vector machines (SVM), with simulations showing HS-transform combined with DT achieves superior accuracy under varying loads, solar insolation, harmonics, and noise [86]. **D. Jarika** et al introduced a novel method for accurately detecting and classifying symmetrical and asymmetrical faults, overcoming traditional technique limitations, with PSCAD simulations on a distribution system confirming its high accuracy and reliability, promising enhanced fault diagnosis for modern power systems under complex and dynamic conditions [87]. M. Getthanjali et al proposed fault detection and classification method combining Wavelet Transformation Technique (WTT) for rapid fault identification and Decision Tree

Algorithm (DTA) for precise fault categorization, tested on a MATLAB/Simulink-modeled power system under normal and asymmetrical fault conditions, with simulation results validating effective fault localization [89]. **M. Shaik** et al a novel Stockwell transform-based protection scheme, validated on the IEEE 14-bus system in MATLAB, detects and classifies faults in a solar photovoltaic-integrated distribution network by analyzing substation fault current transients' second harmonic peak magnitude (fault index) against a threshold, demonstrating resilience to switching transients, component energization/de-energization, and noise across varied fault angles and locations [90]. **S. V. R. Naik** et al introduced a Wavelet Transform and Data Mining-based methodology for fault diagnosis in PV-integrated distribution systems, validated through simulations and real-world data, achieving 99.3% accuracy in detecting line-to-ground faults, arc faults, and partial shading, outperforming existing literature methods while enhancing reliability, scalability, and response time for sustainable energy networks [91]. **O. A. Gashteroodkhani** et al proposed novel intelligent protection scheme for fault detection in microgrids with multiple distributed generations, which employs S-transform to extract statistical features from one cycle of three-phase post-fault feeder currents, constructing a deep belief network model validated on unseen data using a MATLAB-integrated real-time digital simulator, surpassing existing methods across diverse operating conditions, radial/mesh topologies, and grid-connected/islanded modes [92]. **D. K. J. S. Jayamaha** et al proposed an algorithm appling Wavelet Transform to sampled branch current measurements, capturing temporal variations in relative wavelet energy across frequency bands to form a feature vector, classified by an artificial neural network for rapid, reliable DC fault detection and precise localization, validated through comprehensive studies demonstrating superior performance under strict time constraints [93]. **S. R. K. Joga** et al employed a novel combination of machine learning and signal processing techniques for enhanced fault detection and isolation, outperforming existing methods by analyzing current fluctuations for improved monitoring and control in a microgrid system [94]. **P. Pandey** et al introduced a novel microgrid protection scheme utilizing discrete wavelet transform (DWT) for multi-resolution analysis of three-phase current signals, computing spectral entropy in real-time via a microcontroller to trigger circuit breaker trip signals under various fault conditions, validated through controller hardware-in-the-loop (CHIL) testing with a real-time digital simulator (RTDS) and RSCAD microgrid model, demonstrating high accuracy, simplicity, and cost-effectiveness compared to traditional protection methods [95]. **K. Thattai** et al presents a dual approach using Park's Vector Trajectory (PVT) for real-time detection of load current transients and Hilbert-Huang Transform (HHT) for offline analysis of fault transients at the point of common coupling (PCC), leveraging instantaneous frequency from the Hilbert-Spectrum to identify fault timing and harmonic components in load current [96]. **S. Ranjbar** et al This study introduces a fault detection method for microgrids, employing wavelet packet transform (WPT) to preprocess one cycle of voltage and current signals from various fault and no-fault scenarios, extracting key features via detailed WPT coefficients, and utilizing random forest (RF) and K-nearest neighbors (K-NN) classifiers, enhanced by two filter-based feature selection methods, to distinguish faults from non-fault events with high accuracy, validated on a standard IEC microgrid simulated in islanded and grid-connected modes with meshed and radial topologies [97]. **Y. Y. Hong** et al proposes a fault detection, classification, and localization method for microgrids, utilizing discrete wavelet transform (DWT) multi-resolution analysis to compute wavelet entropies of three-phase fault voltages, currents, and neutral fault current as inputs to a Taguchi-based artificial neural network (ANN), trained with orthogonal datasets from Taguchi's experiments, implemented on a Renesas RX62T microcontroller, and validated via chip-in-the-loop simulation with an OP5600 real-time digital simulator and a 50 kVA static switch, demonstrating effective fault phase identification and localization [98]. **S. Kar** et al introduced a data-mining-based differential protection scheme for microgrids, utilizing discrete Fourier transform to preprocess faulted current and voltage signals, extracting sensitive features from both feeder ends to compute differential features, which feed a decision tree-based model for reliable relaying decisions, validated extensively across diverse fault scenarios in the IEC microgrid model for radial and mesh topologies in grid-connected and islanded modes, ensuring robust and secure microgrid operation [99]. **A. M. Stanisavljević** et al introduces a data-mining-based differential protection scheme for microgrids, utilizing discrete Fourier transform to pre-process faulted current and voltage signals, extracting sensitive features from both feeder ends to compute differential features, which feed a decision tree-based model for reliable relaying decisions, validated extensively across diverse fault scenarios in the IEC microgrid model for radial and mesh topologies in grid-connected and islanded modes, ensuring robust and secure microgrid operation [100]. **M. R. B. M. Saifuddin** et al proposed a novel hybridized approach for in-house operators to detect, classify, and locate fault interferences in a nanogrid system, integrating fuzzy control and discrete Fourier transform to recompose directional fault relay functions through a three-stage algorithm: quantifying conditional correlate coefficients from feeder-sampled current and phase angle features, applying a fuzzy logic controller to assess linguistic truth values, and directing circuit breaker operations to isolate faulted regions based on post-phase-shift aberrations, validated on a MATLAB-simulated nanogrid model [101]. **J. Yan** et al proposed a method which is able to improve the responsiveness of early-warning models to real power network operational environment, enhancing the level of intelligence of the security analysis to cope with renewable uncertainty [102]. **K. Saxena** et al presents a fast and accurate algorithm for estimating synchro-phasors, system frequency, and rate of change of frequency (ROCOF), designed to handle abrupt variations in amplitude and phase combining an initial frequency estimation process with a Logarithmic Entropy Ratio–based method to reliably detect transient events [103]. **M. U. Kanth** et al introduces an integrated method for identifying and classifying AC and DC faults using symmetrical component decomposition of line currents, where the resulting symmetrical-domain currents are further employed to compute voltage drops across the line section at both the sending and receiving ends [104].

However, it has been observed from the past works that the statistical nature of harmonic content in the waveforms of currents (generator bus) have not yet been widely studied for fault identification. Fault diagnosis in online, broadly classified as, impedance-based and travelling wave-based methods. Perfect measurement of line parameters is extremely required in impedance based method because between existing line parameters and impedance at fault condition, a comparative study is always required. So, the accuracy relies on the exact measurement of parameters. Travelling wave-based analysis depends on information regarding wave velocity and time instants of multiple 'fault-created' waves at the site of 'fault-locator' [88]. Discrete Wavelet Transform has been applied to identify of faults in power systems and machines in past but the accuracy analysis using wavelet transform is heavily dependent upon the correct selection of mother wavelet. S – Transform is capable of eliminating this complication. At past, it has been widely applied to detect disturbances in power quality, faults in analog electronic circuits and also in power distribution networks and transmission lines. However, the techniques proposed at past are well suited for conventional grids with a high level of voltage and current. Past methods work satisfactorily only for some specific types of faults e.g. symmetrical, asymmetrical, or high-impedance faults. The diverse studies reviewed have significantly contributed to understanding fault analysis, classification, and localization techniques in a microgrid network as well as in conventional power grids; thereby helping the development of the novel fault analysis algorithms proposed in this thesis.

2.7 Methods of Fault Analysis for Microgrid Network

The presented work can be divided into two primary approaches: analysis of statistical parameters using Discrete Wavelet Transform (DWT) and Stockwell Transform (S-Transform) for examining out-going currents from generator buses to assess faults at the remote end within a microgrid network. A short trial using FFT was conducted before using the aforementioned signal processing tools but it yielded low precision in identifying the type as well as location of the fault occurring at the load buses. Due to the non-stationary (signals having time varying frequency) nature of the current signals during the fault, FFT failed to deliver reliable outcomes. Thus, subsequent sections aim to provide only a brief description of DWT and S-Transform in addition with the definitions of statistical parameters broadly used in this work.

2.8 Definitions of Different Statistical Parameters

Skewness

Skewness quantifies the asymmetry of a distribution of data around its mean. It indicates whether the data is skewed to the left (negative skew) or right (positive skew) relative to a normal distribution. A normal distribution has zero skewness because mean, median and mode coincide with each other [103]. Right-Skewed distributions are those which have longer right tail i.e. mean is greater than median and median is also greater than mode. Left-Skewed distributions are those which have longer left tail i.e. mean is less than median and median is also less than mode. Fig. 2.8 given below illustrates the aforementioned concepts.

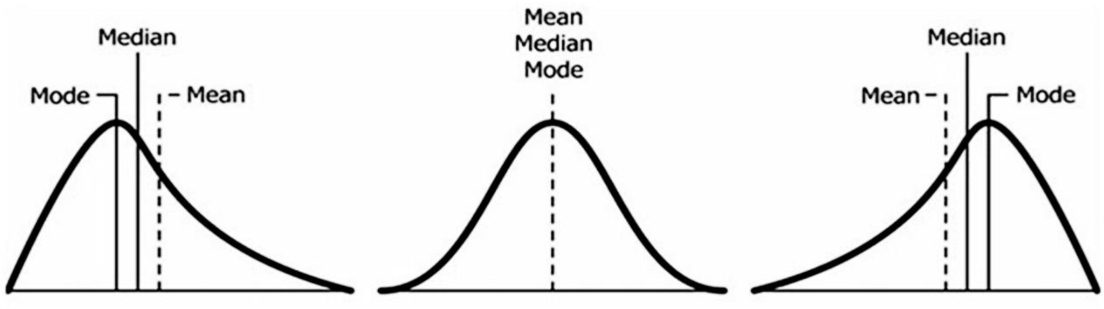

2.8(a) 2.8(b) 2.8(c)

Fig. 2.8: (a) Positive skewness **(b)** zero skewness and **(c)** negative skewness

Kurtosis

Kurtosis is a type of statistical metric which describes the peakedness of a distribution. If a distribution possesses greater peakedness in comparison with the normal distribution then it is called Leptokurtic. If a distribution is more flat in comparison with the normal distribution then it is called Platykurtic. Normal distribution curves are called Mesokurtic. Fig. 2.9 given below illustrates the aforementioned concepts [103].

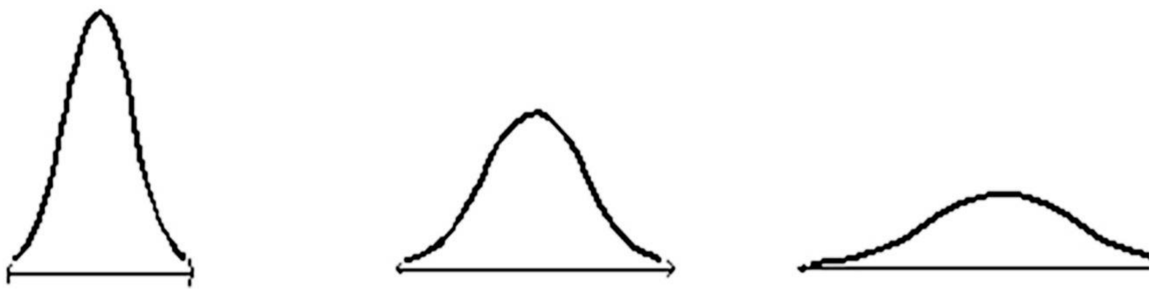

2.9(a) 2.9(b) 2.9(c)

Fig. 2.9: (a) Leptokurtic **(b)** Mesokurtic and **(c)** Platykurtic distribution

2.9 Discrete Wavelet Transform based Statistical Approach

The Wavelet Transform (WT) is employed to examine signals that are non-stationary in nature. In the Wavelet Transform (WT) process, the signal is multiplied by a function known as the mother wavelet, akin to the window function used in the Short-Time Fourier Transform (STFT). The transform is calculated independently for various segments of the time-domain signal. A key feature of the wavelet transform is that the width of the window adjusts as the transform is computed for each segment. Its expression is given below in the equation (2.1).

$$\boldsymbol{w(s,\tau) = \int_{-\infty}^{\infty} f(t)\frac{1}{\sqrt{|s|}}\psi^*\left(\frac{t-\tau}{s}\right)dt} \tag{2.1}$$

Here, the mother wavelet is shown by equation (2.2) given below.

$$\boldsymbol{\varphi_{s,\tau} = \frac{1}{\sqrt{|s|}}\psi\left(\frac{t-\tau}{s}\right)} \tag{2.2}$$

The Continuous Wavelet Transform (CWT) is impractical for analyzing real-world current signals due to its generation of a vast number of data samples. To mitigate excessive data production, the Discrete Wavelet Transform (DWT) is employed instead.

In this method, the original signal is broken down into multiple wavelet bases, from which suitable ones are selected for signal analysis. This approach effectively reduces the number of data sets to be processed. In Discrete Wavelet Transform (DWT) analysis, multilevel decomposition is performed utilizing approximation and detail coefficients. The basic decomposition process is illustrated in Fig. 2.10 below.

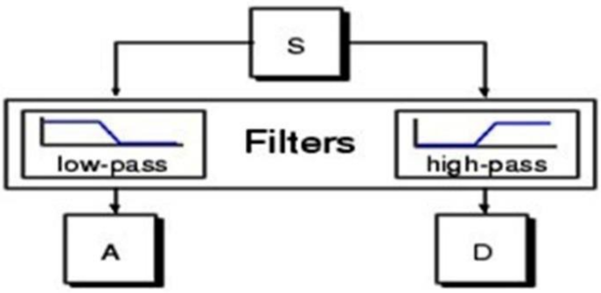

Fig. 2.10: Decomposition process of signal ‘S’

The original signal ‘S’ is processed through two complementary filters, producing two distinct signals. However, in practical digital signal processing, this operation doubles the data volume. For instance, if the original signal ‘S’ contains 1000 data samples, each resulting signal after decomposition would also have 1000 samples, leading to a total of 2000 samples. This outcome undermines the advantage of choosing DWT over CWT. To address this, down-sampling is applied. By closely examining the computation, every other point in each of the 2000-sample signals can be retained to preserve the complete information. This concept is known as down-sampling. Figure 2.11 given below, visually depicts an example of a single-stage DWT applied to a pure sinusoidal signal overlaid with high-frequency noise.

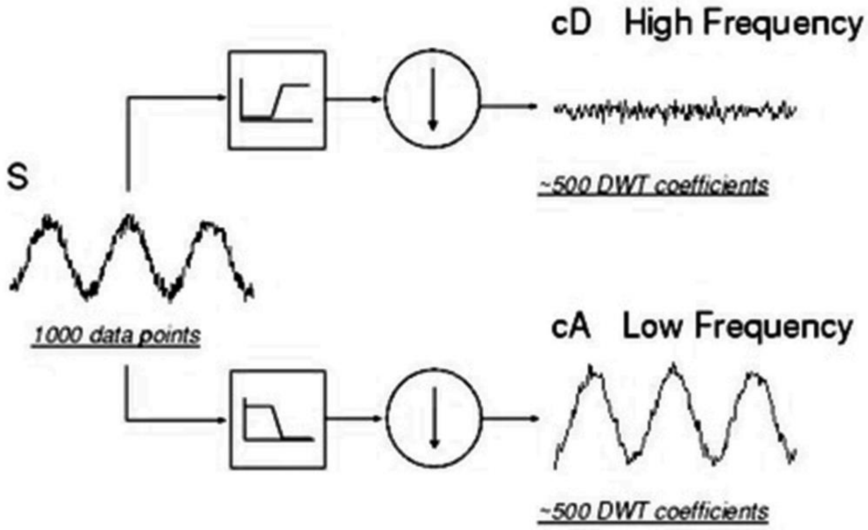

Fig 2.11: Single stage discrete wavelet transform

The detail coefficient 'cD' primarily captures high-frequency noise, while the approximation coefficient 'cA' contains significantly less noise compared to the original signal. Together, 'cA' and 'cD' encompass all the information of the signal 'S', which can be reconstructed through an inverse operation using these coefficients. In the context of DWT, the approximation coefficients (cA) undergo further decomposition, breaking down the original signal 'S' into multiple lower-resolution components. This process is referred to as the 'Wavelet Decomposition Tree', as illustrated in Fig. 2.12.

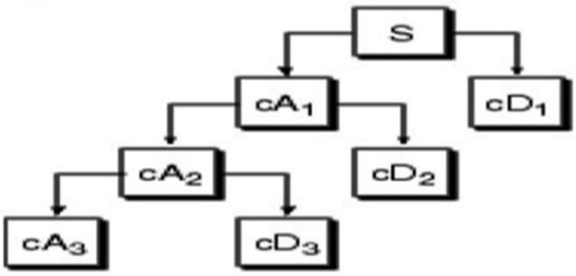

Fig. 2.12: Wavelet Decomposition Tree

In theory, the decomposition process can continue infinitely. However, in practice, it is limited to the point where individual details are reduced to a single sample. The number of decomposition levels is selected based on the characteristics of the signal. In the work presented here, the out-going current signals of 50 Hz fundamental frequency, from various generator buses of IEEE-standard 14 bus microgrid network are decomposed for nine levels to consider up to 20th harmonic component of the currents i.e. 1000 Hz. For both approximate and detail level coefficients RMS, skewness and kurtosis values are computed in each level.

2.10 Stockwell Transform based Statistical Approach

S-Transformation is applied to the out-going current signals from the generator buses of IEEE-standard 14 bus microgrid network under seven distinct conditions: ‘healthy’, ‘L-G’, ‘L-L’, ‘L-L-G’, and ‘L-L-L’ faults at load bus B-6 and B-10, as well as in nearby transmission lines. Compared to other common signal processing techniques, S-Transformation offers two key benefits. Its analysis accuracy does not depend on the choice of the mother wavelet and it can effectively display various harmonics at different time instants. The S-Transformation is built upon the Continuous Wavelet Transform (CWT), utilizing a scalable and movable Gaussian window. The S-Transform offers superior resolution compared to CWT. The CWT of a function g(t) can be represented as follows [102]:

$$W(\tau,d)=\int_{-\infty}^{\infty} g(t)\Psi(t-\tau,d)dt \tag{2.3}$$

Here, $\Psi(\tau,d)$ represents the ‘mother wavelet,’ and 'd' denotes the dilation (inverse of frequency) of the mother wavelet, which is used to adjust the signal frequency resolution. Consequently, the S-transformation of g(t) is obtained by multiplying the mother wavelet by a ‘phase factor,’ as shown below in equation (2.4):

$$S(\tau,f)=W(\tau,d)\exp(i2\pi ft) \tag{2.4}$$

Here, the mother wavelet is:

$$\Psi(\tau,d)=\frac{|f|}{\sqrt{2\pi}}\exp(\frac{-t^2f^2}{2})\exp(-i2\pi ft) \tag{2.5}$$

Let g[kT] be the discrete time-series representation of g(t), with a sampling interval of T and k = 0, 1, …, (N-1). The ‘Discrete Fourier Transform’ (DFT) of g[kT] is expressed as follows:

$$G\left[\frac{n}{NT}\right]=\frac{1}{N}\sum_{k=0}^{N-1} g[kT]\,exp\left(-\frac{i2\pi nk}{N}\right) \tag{2.6}$$

If G(f) is the Fourier spectrum, ‘f’ is tending towards (n/NT) and τ to jT, in that case S-transformation of g[kT] is given by equation (2.7) given below where Here, n = 0, 1,…., (N-1).

$$S\left[jT,\frac{n}{NT}\right]=\sum_{p=0}^{N-1} G\left[\frac{p+n}{NT}\right]\exp\left(\frac{-2p^2\pi^2}{n^2}\right)\exp\left(\frac{i2\pi pj}{N}\right) \tag{2.7}$$

The S – Transformation matrix of order (m×n), thus produced can be expressed as shown below in equation (2.8) [102].

$$(S_{ij})_{m\times n} = \begin{array}{c c} & \begin{array}{cccc} t_1 & t_2 & \cdots & t_n \end{array} \\ \begin{array}{c} f_1 \\ f_2 \\ f_3 \\ \vdots \\ \\ f_m \end{array} & \begin{bmatrix} x_{11} & x_{12} & \cdots & x_{1n} \\ x_{21} & x_{22} & \cdots & x_{2n} \\ x_{31} & x_{32} & \cdots & x_{3n} \\ \vdots & \vdots & \vdots & \vdots \\ \vdots & \vdots & \vdots & \vdots \\ x_{m1} & x_{m2} & x_{m3} & x_{mn} \end{bmatrix} \end{array} \tag{2.8}$$

As represented by equation (2.8) given above; rows and columns of the 'S – Transformation matrix' shows frequency and time respectively. Skewness can be calculated using equation (2.9), given below.

$$Skewness = \frac{\frac{1}{n}\sum_{i=1}^{n}(x_i - \frac{1}{n}\sum_{i=1}^{n} x_i)^3}{\left\{\frac{1}{n-1}\sum_{i=1}^{n}(x_i - \frac{1}{n}\sum_{i=1}^{n} x_i)^2\right\}^{3/2}} \tag{2.9}$$

Skewness of the S – Transformation matrix given in equation (2.8) can be determined as shown below in equation (2.10).

$$Skewness = \frac{\frac{1}{m}\sum_{i=1}^{m}(x_{ij} - \frac{1}{m}\sum_{i=1}^{m} x_{ij})^3}{\left\{\frac{1}{m-1}\sum_{i=1}^{m}(x_{ij} - \frac{1}{m}\sum_{i=1}^{m} x_{ij})^2\right\}^{3/2}} \tag{2.10}$$

Where, j = 1, 2, 3 ... n.

Equation (2.10) clearly shows that the skewness of the S-Transformation matrix elements is computed column-wise, meaning the skewness is evaluated for the elements at each time instant. Plots of skewness versus time are also generated. The subsequent section includes these plots, illustrating the variations in skewness values over time.

2.11 Summary

Both DWT and S-Transform based approaches are used to identify fault location and fault type in IEEE-standard 14 bus microgrid network by comparing healthy and faulty conditions. These signal processing tool based statistical analysis focuses on the statistical nature of the harmonic components present in the out-going current signals from various generator buses of the aforementioned microgrid network instead of working with the magnitudes of different harmonics components present in the current signals. Subsequent chapters showcase the analysis in detail.

Publication:

Datta, S., Chattopadhyaya, A., Chattopadhyay, S., & Das, A. (2024). Comparative Study of Different Existing Standard Microgrid Networks. Linear and Nonlinear System Modeling, 33-47.

Chapter 3

FFT based Harmonic Distortion Estimation and DWT based Statistical Parameter Evaluation for Line to Ground Fault Detection

This chapter demonstrates the use of Fast Fourier Transform (FFT) and Discrete Wavelet Transform (DWT) based statistical evaluation of the currents flowing out from various generator buses for identifying line to ground (L-G) fault in an IEEE-standard 14 bus microgrid system, where conventional fault detection approaches are less effective.

3.1 Introduction

Harmonic and inter-harmonic evaluation based on FFT and DWT based statistical analysis of currents flowing out of various generator buses are utilized for identifying L-G fault in IEEE-standard 14 bus microgrid system. Traditional fault-detection techniques falter due to the significantly reduced voltage and current levels inside microgrid network. Earth faults occurring in microgrid environment create even greater hurdles in detection of the same due to much reduced voltage levels in faulty condition. Analysis using FFT and DWT is performed under both normal and faulty states, leading to the creation of a rule set for identifying fault locations, which contributed to the development of fault classification techniques outlined in subsequent sections.

3.2 IEEE-Standard 14 Bus System with D.C.U.

The IEEE-standard 14 bus microgrid system having Data-Capture Units (D.C.U.) connected to each and every generator bus is depicted in Figure 3.1 given below. This microgrid network incorporates bulk power generator at bus G-13, a photovoltaic (P-V) cell at bus G-12, diesel generator - 1 (DG-1) at bus G-8 and diesel generator - 2 (DG-2) at bus G-3. It features loads of five different kinds; bus B-10 has non-linear load, B-6 has furnace connected to it, battery-charging system is connected to B-1, B-3 and B-2 has linear-load 1 and linear-load 2 respectively. Each bus is interconnected by Π-section lines, with each section spanning a length of 1 kilometer. The Data Capture Units (D.C.U.) monitor the out-going currents from phase 'C' across all generator buses. A line-to-ground (L-G) fault was made to occur separately to phase 'C' of load bus B-10, which hosts a non-linear load, and of bus B-6, associated with a furnace load, while ensuring that the remaining load buses operated normally. These simulations were executed using MATLAB. Total time of simulation is equal to 0.8 seconds. The fault duration is set between 0.2 and 0.4 seconds. For FFT analysis, 15 cycles of out-going currents from various generator buses are evaluated, starting at 0.15 seconds. The maximum sampling frequency of 2000 Hz is kept to cancel out any possibility of aliasing. The Total Harmonic Distortion (THD) levels and significant inter-harmonic elements in the out-going current signal from the generator buses are recorded. Subsequently, Discrete Wavelet Transform (DWT) is applied to these currents, yielding approximate and detail coefficients. For DWT analysis the current waveforms were broken down into nine levels for normal as well as faulty conditions.

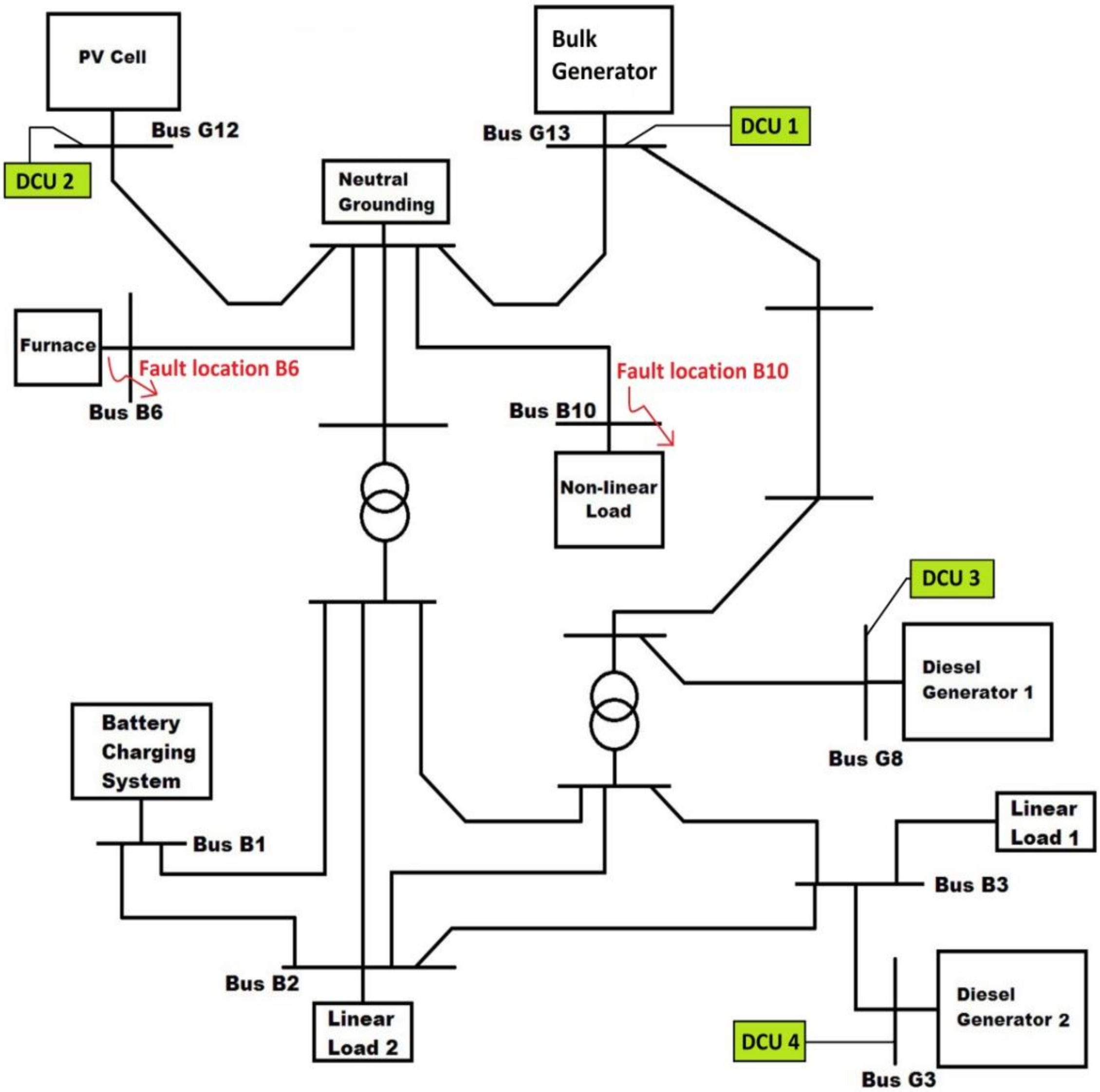

Fig. 3.1: IEEE-Standard 14 Bus Microgrid System with D.C.U. connected to generator buses

Among all loads, the non-linear load and furnace primarily contribute harmonics in the current waveforms. Consequently, L-G faults at the non-linear load bus (B-10) and furnace bus (B-6) were evaluated.

Out-going current waveforms from bulk generator bus in normal as well as faulty conditions are shown below in Fig. 3.2, 3.3 and 3.4. In Fig. 3.2 -3.4, ‘x – axis’ represents time in seconds and ‘y – axis’ represents signal magnitude i.e. current magnitude in ampere.

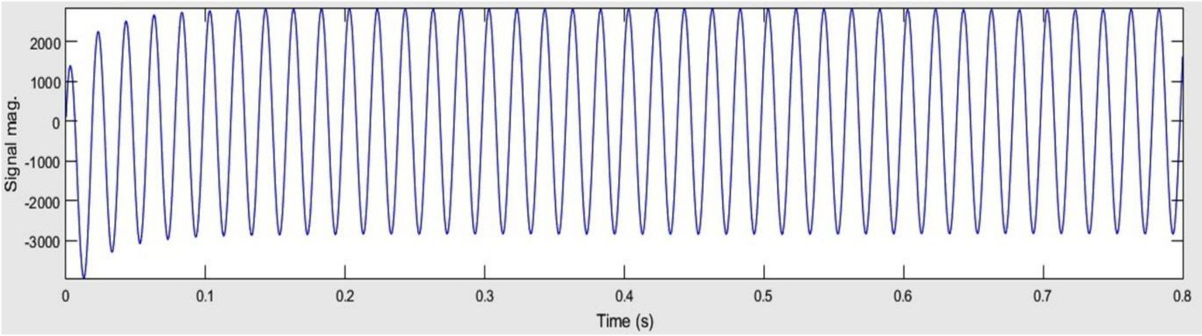

Fig. 3.2: The out-going current waveform from the bulk-generator bus during normal condition

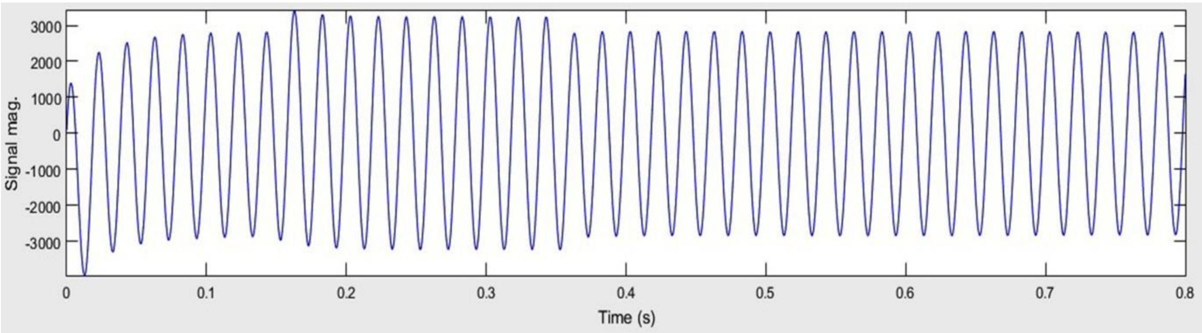

Fig. 3.3: The out-going current waveform from the bulk-generator bus during an L-G fault at B-10

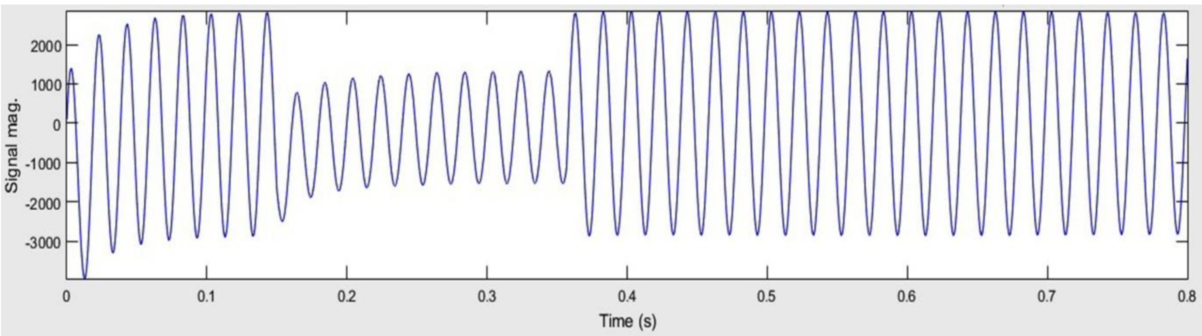

Fig. 3.4: The out-going current waveform from the bulk-generator bus during an L-G fault at B-6

The waveforms of the out-going currents from the P-V Cell bus under normal as well as faulty conditions are shown below in Fig. 3.5, 3.6 and 3.7. In Fig. 3.5 – 3.7, 'x – axis' represents time in seconds and 'y – axis' represents current magnitude in ampere.

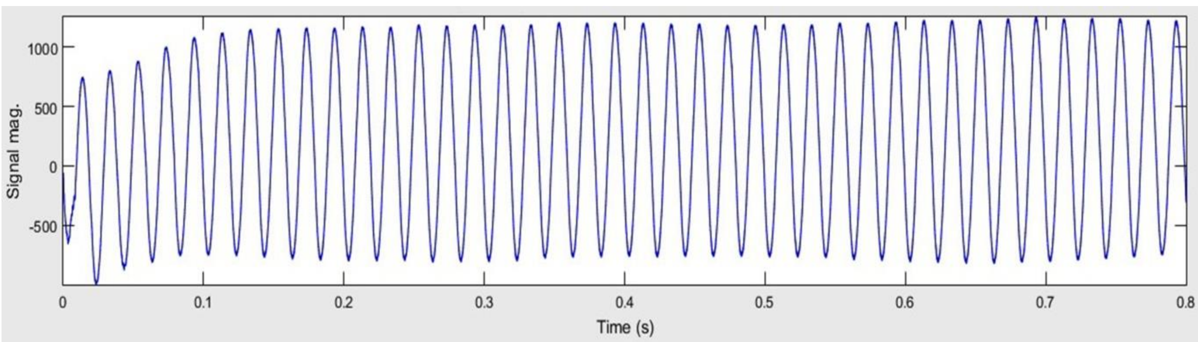

Fig. 3.5: The out-going current waveform from the P-V Cell bus during normal condition

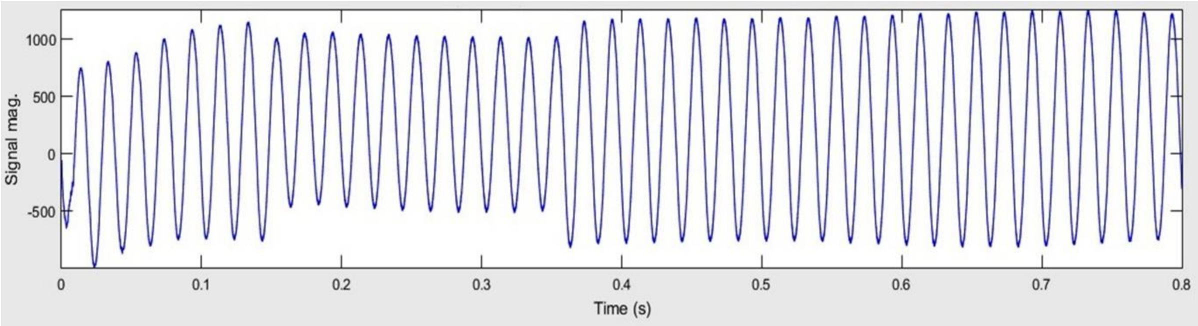

Fig. 3.6: The out-going current waveform from the P-V Cell bus during an L-G fault at B-10

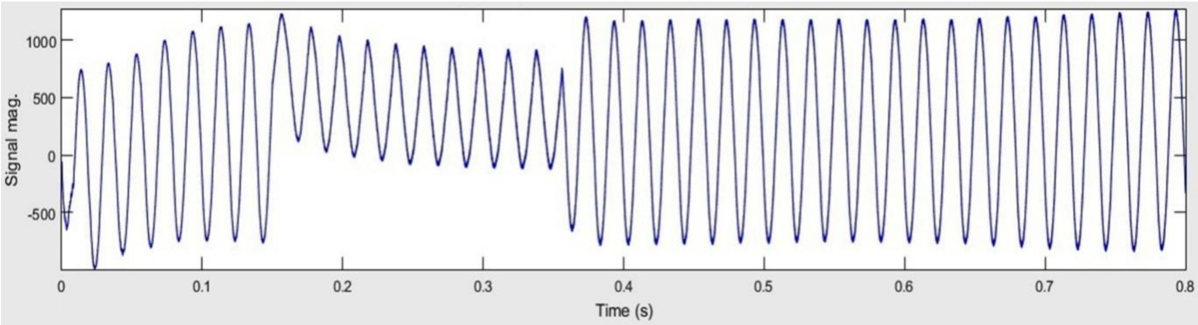

Fig. 3.7: The out-going current waveform from the P-V Cell bus during an L-G fault at B-6

The waveforms of the out-going currents from the DG-1 bus in normal as well as faulty conditions are shown below in Fig. 3.8, 3.9 and 3.10. In Fig. 3.8 – 3.10, 'x – axis' represents time in seconds and 'y – axis' represents current magnitude in ampere.

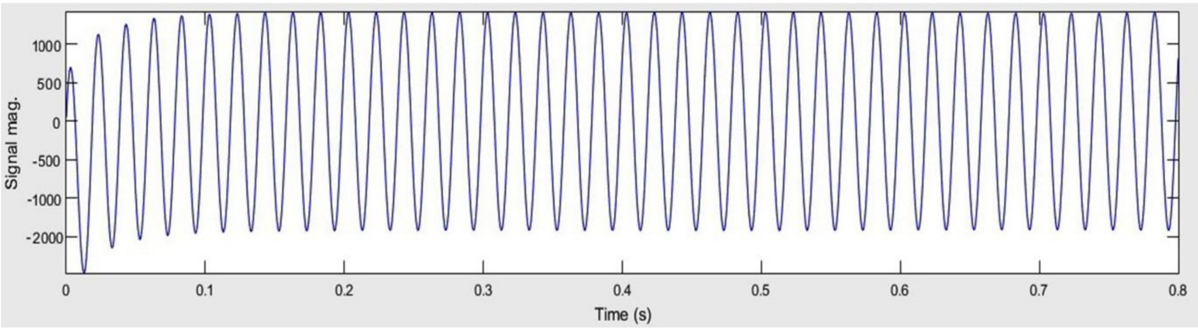

Fig. 3.8: The out-going current waveform from the DG-1 bus during normal condition

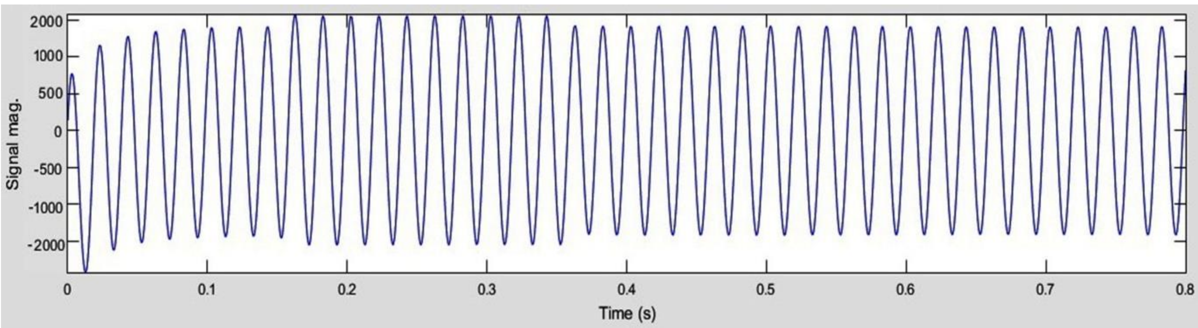

Fig. 3.9: The out-going current waveform from the DG-1 bus during an L-G fault at B-10

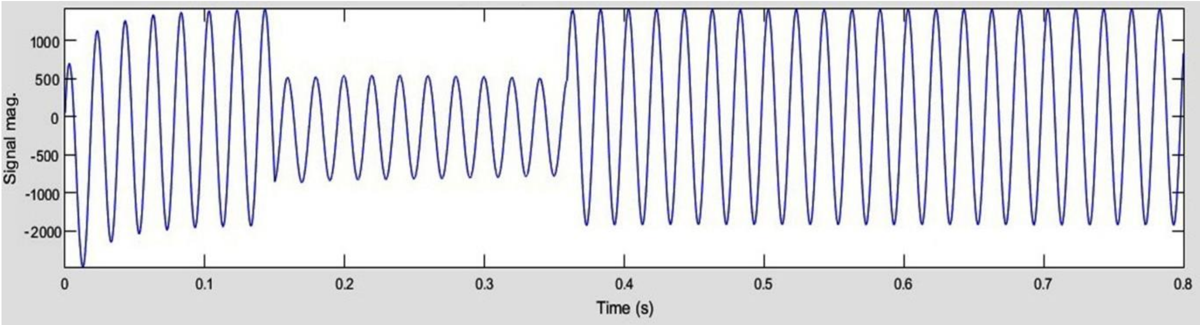

Fig. 3.10: The out-going current waveform from the DG-1 bus during an L-G fault at B-6

Out-going currents from the DG-2 bus in normal as well as faulty conditions are shown below in Fig. 3.11, 3.12, 3.13. Here, x–axis shows time in seconds and y-axis current in ampere.

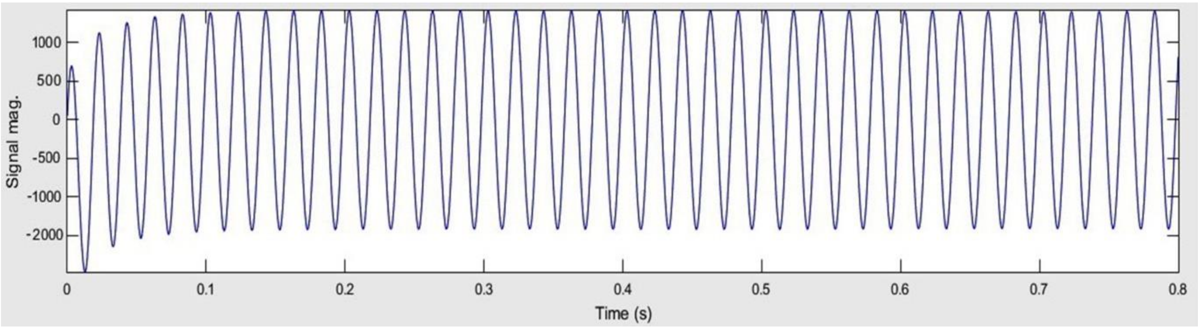

Fig. 3.11: The out-going current waveform from the DG-2 bus during normal condition

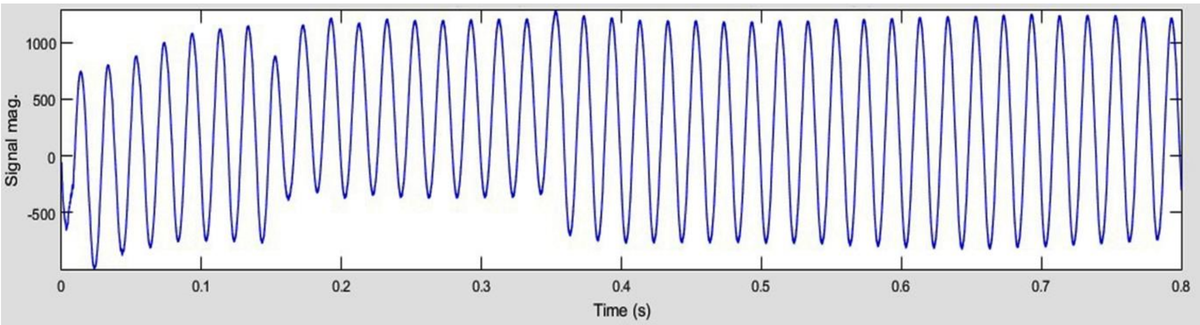

Fig. 3.12: The out-going current waveform from the DG-2 bus during an L-G fault at B-10

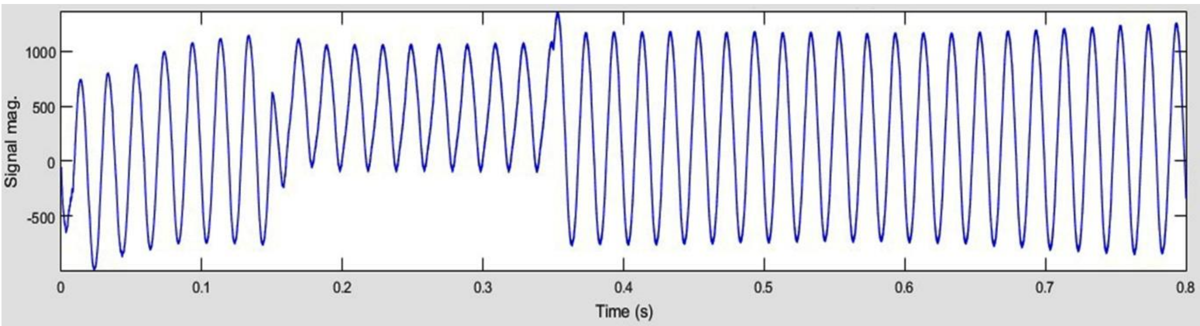

Fig. 3.13: The out-going current waveform from the DG-2 bus during an L-G fault at B-6

It has been observed from the waveforms depicted above in Fig. 3.2 – 3.13, that all the generator bus out-going currents possess significant amount of distortion in comparison with their respective normal condition values during the occurrence of the L-G faults.

3.3 Evaluation of Integer and Inter-harmonic Components using FFT Analysis

FFT evaluations of the output currents from various generator buses are conducted, capturing the Total Harmonic Distortion (THD) value and identifying the primary inter-harmonic components. For this FFT analysis, 15 cycles of the output currents from these generator buses are examined, starting at 0.15 seconds with a maximum sampling rate of 2000 Hz.

3.3.1 Integer Harmonic Evaluation

FFT analysis is applied to the output currents from various generator buses, and the THD is determined using integer harmonic values under different conditions. THD values for integer harmonics of the out-going currents from various generator buses under different conditions are calculated and presented in Table 3.1.

Table 3.1 THD values for integer harmonics of out-going currents from various generator buses

Condition	THD Values of out-going Currents in percentage of Fundamental			
	Bulk-Gen Bus (G-13)	PV Cell Bus (G-12)	DG-1 Bus (G-8)	DG-2 Bus (G-3)
Normal	0.055	2.102	0.384	0.278
L-G at B-10	0.037	1.58	0.44	0.338
L-G at B-6	0.043	4.87	0.608	0.753

Variations in THD values for integer harmonics of out-going currents from various generator buses under different scenarios are graphically represented below in Fig. 3.14.

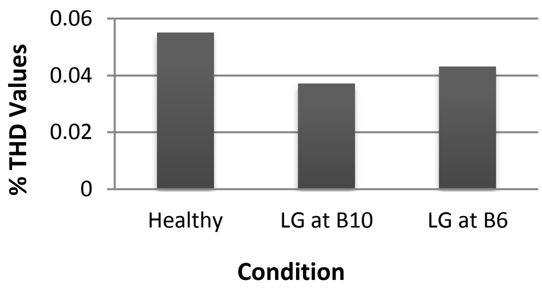

3.14 (a)

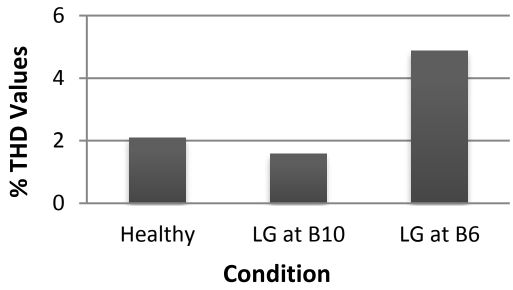

3.14(b)

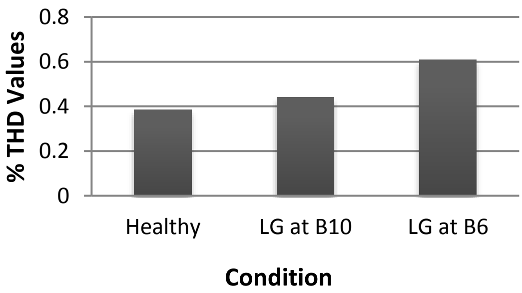

3.14 (c)

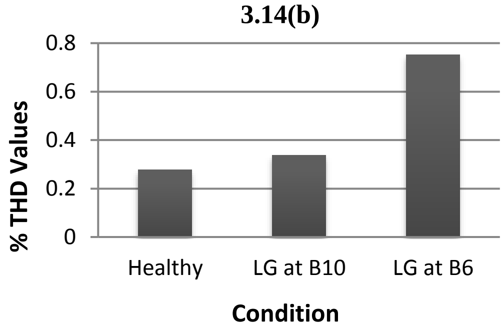

3.14 (d)

Fig. 3.14: Integer harmonic THD values of Out-going Current of **(a)** Bulk Generator bus, **(b)** PV Cell bus, **(c)** DG-1 bus and **(d)** DG-2 bus

3.3.2 Inter-Harmonic Evaluation

Analysis of inter-harmonics is conducted via Fast Fourier Transform (FFT) in compliance with the ‘IEC 61000-4-7’ standard. The components of inter-harmonics of frequency less than that of the fundamental, termed ‘sub-harmonics’, are categorized as inter-harmonic group - 0 (IG-0). Those falling between the fundamental and the second order harmonic are designated as inter-harmonic group - 1 (IG-1), with successive groups categorized accordingly. The magnitudes of inter-harmonic groups are calculated by considering inter-harmonic components at 5 Hz intervals between the frequencies of integer harmonics. For a 50 Hz fundamental frequency, the magnitude of the Nth inter-harmonic group is determined using equation (3.1).

$$\mathrm{IG_N} = \sqrt{\sum_{k=1}^{9} \mathrm{I}^2_{(50\mathrm{Hz}\times \mathrm{N}+5\mathrm{Hz}\times \mathrm{k})}} \tag{3.1}$$

The analysis focuses on the first three inter-harmonic groups, as the magnitudes of higher groups diminish substantially. The magnitudes of inter-harmonic groups, represented as percentage of fundamental frequency, are computed for the currents flowing out of various generator buses under distinct operating conditions. Magnitudes of inter-harmonic groups for out-going currents from bulk-generator bus, P-V Cell bus, DG-1 & DG-2 bus at various conditions, are presented below in Table 3.2, 3.3, 3.4 and 3.5 respectively.

Table 3.2 Inter-harmonic Group (I-G) Magnitude for Bulk Generator Bus

Condition	Inter-harmonic Group (I-G) Magnitude in percentage of Fundamental			
	IG-0	IG-1	IG-2	IG-3
Normal	0.0436	0.0173	0	0.01
L-G at B-10	0.1077	0.0616	0.03	0.0173
L-G at B-6	1.3245	0.8075	0.1421	0.0436

Table 3.3 Inter-harmonic Group (I-G) Magnitude for PV Cell Bus

Condition	Inter-harmonic Group (I-G) Magnitude in percentage of Fundamental			
	IG-0	IG-1	IG-2	IG-3
Normal	0.8729	0.2352	0.17	0.1519
L-G at B-10	3.0687	1.8806	0.2828	0.1574
L-G at B-6	36.9728	21.3704	2.37321	1.0367

Table 3.4 Inter-harmonic Group (I-G) Magnitude for DG - 1 Bus

Condition	Inter-harmonic Group (I-G) Magnitude in percentage of Fundamental			
	IG-0	IG-1	IG-2	IG-3
Normal	0.3313	0.1338	0.0529	0.0842
L-G at B-10	1.2624	0.5483	0.1425	0.1109
L-G at B-6	8.9134	3.9748	0.7836	0.2081

Table 3.5 Inter-harmonic Group (I-G) Magnitude for DG - 2 Bus

Condition	Inter-harmonic Group (IG) Magnitude in percentage of Fundamental			
	IG-0	IG-1	IG-2	IG-3
Normal	0.5247	1.0654	0.1204	0.0479
L-G at B-10	1.0739	1.3644	0.1161	0.2696
L-G at B-6	4.919	4.75	0.1738	0.3398

Changes in the magnitudes of groups of inter-harmonics for out-going currents from the bulk-generator bus, P-V Cell bus, DG-1, and DG-2 buses under various conditions are illustrated in Figures 3.15(a), 3.15(b), 3.15(c), and 3.15(d), respectively.

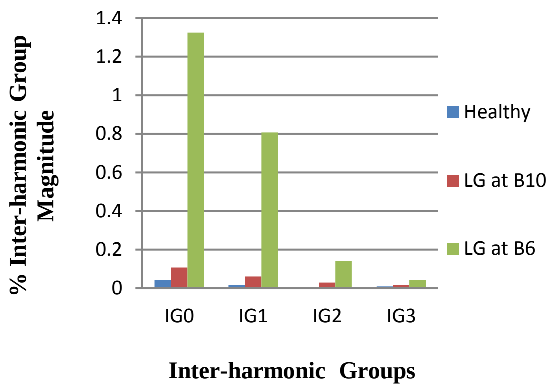

3.15(a)

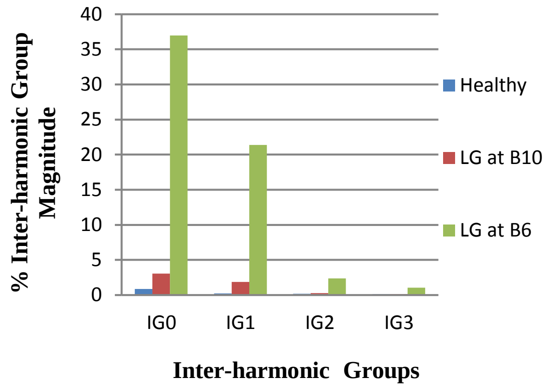

3.15(b)

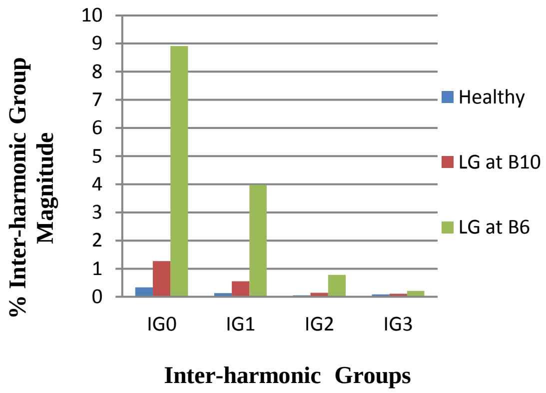

3.15 (c)

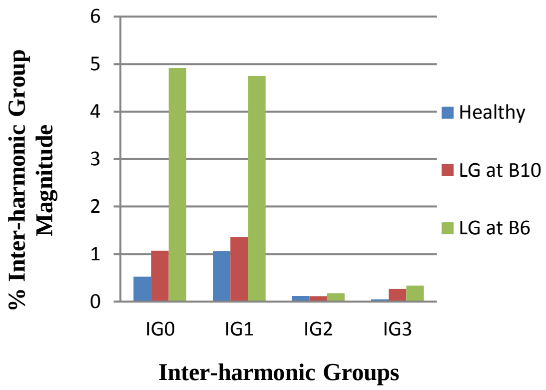

3.15 (d)

Fig. 3.15: Changes in the Magnitudes of Groups of Inter-harmonics of Out-going Current from **(a)** Bulk-Generator bus, **(b)** P-V Cell bus, **(c)** DG-1 bus and **(d)** DG-2 bus

3.4 Observations from FFT - based Assessment

The findings from the results presented in the preceding section are outlined below.

3.4.1 Observation from Bulk Generator Bus

Fig. 3.14(a) shows that THD value of the bulk generator bus out-going current decreases when L-G fault occurs either at B-10 or at B-6.

However, from Fig. 3.15(a) it has been observed that significant increment in the magnitudes of inter-harmonic groups, particularly in case of IG-0 and IG-1. IG-0 and IG-1 have increased up to 1.2% and 0.8% of fundamental respectively due to L-G fault at B-6.

3.4.2 Observation from P-V Cell Bus

Fig. 3.14(b) shows the THD of the P-V Cell bus output current rising to approximately 1.6% of the fundamental during an L-G fault at B-10 and nearing 5% for an L-G fault at B-6.

As illustrated in Fig. 3.15(b), an L-G fault at B-6 causes IG-0 and IG-1 to surge beyond 35% and 20% of the fundamental frequency, respectively. In contrast, under normal conditions or during an L-G fault at B-10, these values stay below 5%.

3.4.3 Observations from DG-1 Bus

Fig. 3.14(c) reveals that the Total Harmonic Distortion (THD) of the output current from the DG-1 bus reaches its lowest level (below 0.4%) under normal system conditions, while it peaks (exceeding 0.6%) during an L-G fault at B-6.

As shown in Fig. 3.15(c), the magnitudes of inter-harmonic groups of the out-going current from DG-1 bus remain under 1% of the fundamental during normal operation. However, during an L-G fault at B-10, the magnitude of IG-0 exceeds 1%, and at B-6, it rises to as high as 9%. Additionally, the IG-1 magnitude climbs to 4% of the fundamental during an L-G fault at B-6.

3.4.4. Observations from DG-2 Bus

Fig. 3.14(d) illustrates that the Total Harmonic Distortion (THD) of the output current from the DG-2 bus exceeds 0.6% of the fundamental during an L-G fault at B-6.

As depicted in Fig. 3.15 (d), there is a significant increase in the amplitudes of IG-0 and IG-1, with both reaching up to 5% of the fundamental when an L-G fault occurs at the furnace bus (B-6).

3.5 Constraints of FFT - based Assessment

For P-V Cell bus alone, integer harmonic based upon FFT assessment satisfactorily discriminated between three different conditions; normal, L-G fault at B-10 and B-6.

The FFT-based ‘inter-harmonic’ analysis of out-going currents from the generator buses comprehensibly differentiates between normal and faulty scenarios. However, it struggles to clearly distinguish between normal condition and an L-G fault at B-10.

3.6 DWT based Harmonic Assessment

Faults cause the current waveforms to become non-stationary in nature. Hence, integer and inter-harmonic analysis based upon FFT did not work satisfactorily for all the cases although up to a restricted extent these results are able to indicate the fault location.

For DWT based analysis, out-going currents of various generator buses are examined in different conditions. At first the original current signal is decomposed into two levels, approximate and details level by passing it through low-pass and high-pass filter respectively. Nine levels of decomposition for both approximate and details level are obtained by repeating the aforementioned process for nine times. First 20^{th} harmonics i.e. components of current up to 1000 Hz frequency are considered. Decomposition is done in nine levels to consider components of current in between 1 – 1000 Hz of frequency range. Down sampling of each level is done after decomposition to get approximate and details coefficients. Approximate coefficient contains components of lower frequency and details coefficient components of higher frequency. RMS, skewness and kurtosis values are computed in each level after getting approximate and details coefficients. Daubechies-4 (DB-4) wavelet is used as the mother wavelet for this DWT analysis. Other mother wavelets (e.g. DB-3, DB-10 etc) are also tested but DB-4 is found to be the most perfectly suitable.

3.6.1 DWT based RMS value comparison

For every generator bus RMS values of approximate coefficient (RMS_A) and details coefficients (RMS_D) are acquired from DWT decomposition of the respective out-going currents at different conditions. RMS_A and RMS_D of bulk generator bus out-going currents are presented in Table 3.6 and 3.7 respectively.

Table 3.6 Values of RMS_A of bulk generator bus out-going currents in different conditions

DWT Decomposition Levels	RMS_A in Normal Condition	RMS_A for L-G fault in B-10	RMS_A for L-G fault in B-6
1	2008.928	2011.583	2053.978
2	2008.927	2011.583	2053.977
3	2008.929	2011.584	2053.979
4	2008.927	2011.583	2053.977
5	2008.901	2011.557	2053.952
6	2008.281	2010.937	2053.327
7	1949.689	1952.254	1993.367
8	663.7544	664.4214	678.0694
9	171.2441	171.4038	172.9059

Table 3.7 Values of RMS_D of bulk generator bus out-going currents in different conditions

DWT Decomposition Levels	RMS_D in Normal Condition	RMS_D for L-G fault in B-10	RMS_D for L-G fault in B-6
1	0.132729	0.132089	0.1306
2	0.412539	0.412336	0.411881
3	0.638166	0.636495	0.637827
4	1.973111	1.972136	1.970971
5	5.519418	5.518871	5.537201
6	44.60744	44.6478	45.46178
7	472.4493	473.1493	483.6959
8	1831.422	1833.912	1872.817
9	638.6482	639.2986	653.0258

Values of RMS_A and RMS_D of bulk generator bus out-going currents are graphically represented in Fig. 3.16 given below.

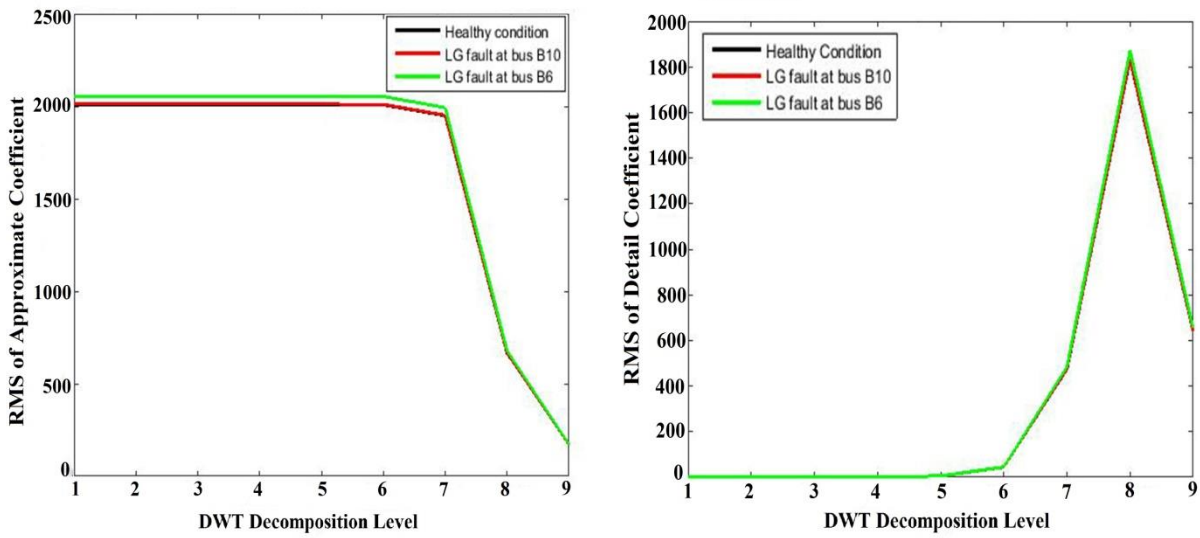

3.16(a) **3.16(b)**

Fig. 3.16: (a) RMS_A and **(b)** RMS_D of bulk generator bus out-going currents

Values in RMS_A and RMS_D of PV Cell bus out-going currents are presented in Table 3.8 and 3.9 respectively.

Table 3.8 Values of RMS_A of PV Cell bus out-going currents in different conditions

DWT Decomposition Levels	RMS_A in Normal Condition	RMS_A for L-G fault in B-10	RMS_A for L-G fault in B-6
1	714.6035	690.1251	668.1125
2	714.6031	690.1247	668.1118
3	714.6019	690.1237	668.1109
4	714.5945	690.1169	668.1008
5	714.5554	690.0821	668.0591
6	714.2372	689.7731	667.7331
7	695.1239	671.3111	651.2443
8	294.8342	287.7444	345.7359
9	200.3699	197.2536	260.4877

Table 3.9 Values of RMS_D of PV Cell bus out-going currents in different conditions

DWT Decomposition Levels	RMS_D in Normal Condition	RMS_D for L-G fault in B-10	RMS_D for L-G fault in B-6
1	11.88607	12.72886	17.33612
2	0.741235	0.713563	0.882612
3	1.525471	1.45219	1.810159
4	3.15603	2.941296	3.399304
5	6.933179	6.337385	6.731102
6	19.97367	19.2584	19.56072
7	161.7552	156.0628	144.711
8	627.0091	603.932	548.864
9	217.6817	210.935	228.7636

Values of RMS_A and RMS_D of PV Cell bus out-going currents are graphically represented in Fig. 3.17 given below.

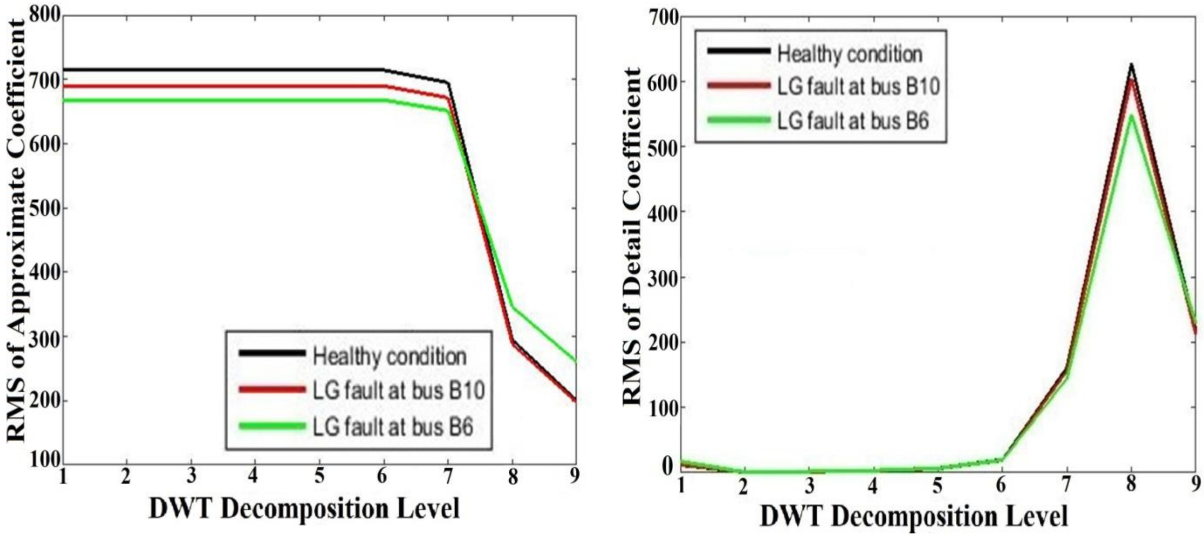

3.17(a) **3.17(b)**

Fig. 3.17: (a) RMS_A and **(b)** RMS_D of P-V Cell bus out-going currents

Values in RMS_A and RMS_D of Diesel Generator 1 (DG-1) bus out-going currents are presented in Table 3.10 and 3.11 respectively.

Table 3.10 Values of RMS_A of Diesel Generator 1 (DG-1) bus out-going currents in different conditions

DWT Decomposition Levels	RMS_A in Normal Condition	RMS_A for L-G fault in B-10	RMS_A for L-G fault in B-6
1	888.3778	885.6942	862.7424
2	888.3779	885.6943	862.7424
3	888.3777	885.6941	862.7421
4	888.3776	885.694	862.742
5	888.3782	885.6947	862.7437
6	888.1954	885.512	862.5659
7	865.1603	862.5705	840.7061
8	363.1631	363.114	368.3535
9	240.0405	241.0287	262.5014

Table 3.11 Values of RMS_D of Diesel Generator 1 (DG-1) bus out-going currents in different conditions

DWT Decomposition Levels	RMS_D in Normal Condition	RMS_D for L-G fault in B-10	RMS_D for L-G fault in B-6
1	0.449198	0.448377	0.449041
2	0.14556	0.144047	0.155146
3	0.301492	0.296015	0.32269
4	0.589186	0.561073	0.658775
5	1.741768	1.704565	1.741607
6	18.51281	18.48218	17.95898
7	198.8265	198.1088	190.4336
8	782.5407	779.6981	753.1033
9	268.1033	267.151	254.2445

Values of RMS_A and RMS_D of Diesel Generator 1 (DG-1) bus out-going currents are graphically represented in Fig. 3.18 given below.

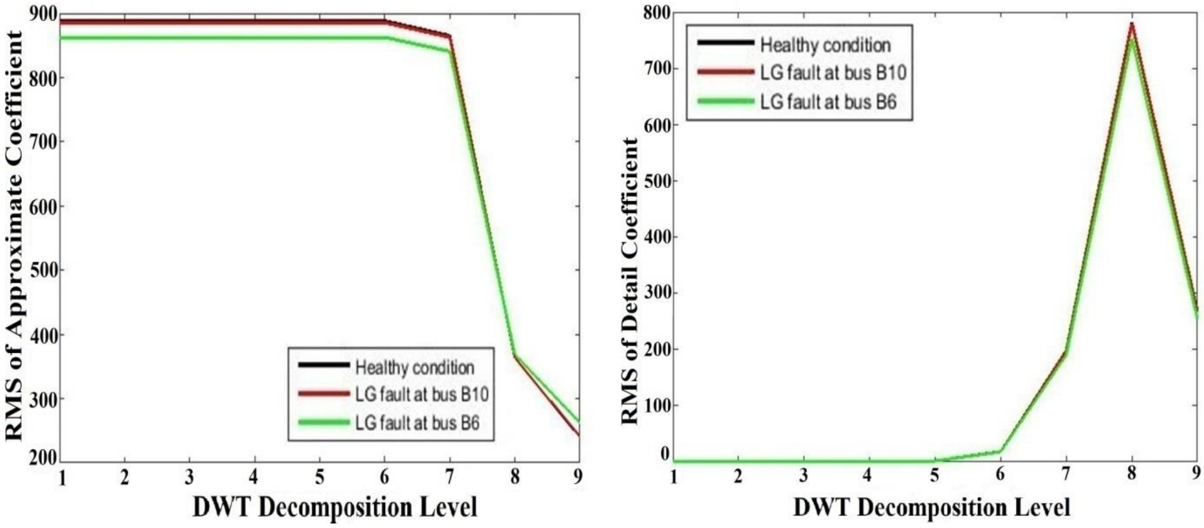

3.18(a) **3.18(b)**

Fig. 3.18: (a) RMS_A and **(b)** RMS_D of Diesel Generator 1 (DG-1) bus out-going currents

Values in RMS_A and RMS_D of Diesel Generator 2 (DG-2) bus out-going currents are presented in Table 3.12 and 3.13 respectively.

Table 3.12 Values of RMS_A of Diesel Generator 2 (DG-2) bus out-going currents in different conditions

DWT Decomposition Levels	RMS_A in Normal Condition	RMS_A for L-G fault in B-10	RMS_A for L-G fault in B-6
1	68.7043	68.716	68.7447
2	68.7043	68.716	68.7447
3	68.7047	68.7164	68.7451
4	68.7049	68.7166	68.7453
5	68.704	68.7157	68.7444
6	68.6816	68.6933	68.722
7	66.7407	66.752	66.7802
8	27.0722	27.0752	27.0921
9	17.02	17.02	17.0165

Table 3.13 Values of RMS_D of Diesel Generator 2 (DG-2) bus out-going currents in different conditions

DWT Decomposition Levels	RMS_D in Normal Condition	RMS_D for L-G fault in B-10	RMS_D for L-G fault in B-6
1	0.03942	0.03524	0.03735
2	0.00955	0.00955	0.00958
3	0.01336	0.01334	0.01336
4	0.04726	0.04726	0.04757
5	0.14609	0.14611	0.14646
6	1.45422	1.4544	1.45459
7	15.7666	15.7695	15.7783
8	61.1245	61.1356	61.1554
9	21.67	21.6738	21.6998

Values of RMS_A and RMS_D of Diesel Generator 2 (DG-2) bus out-going currents are graphically represented in Fig. 3.19 given below.

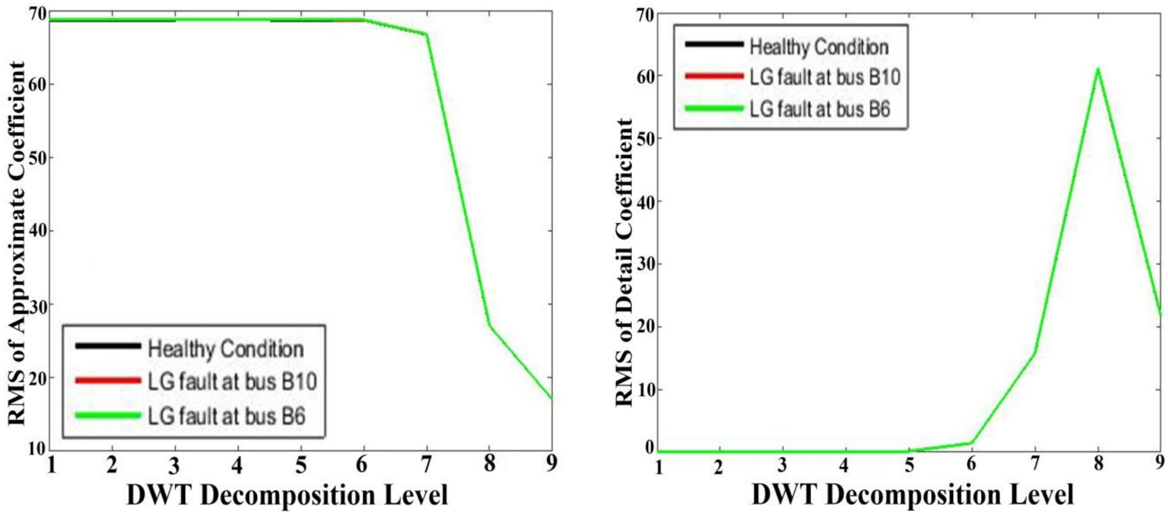

3.19 (a) **3.19(b)**

Fig. 3.19: (a) RMS_A and **(b)** RMS_D of Diesel Generator 2 (DG-2) bus out-going currents

3.6.2 DWT based skewness value comparison

For every generator bus skewness of approximate coefficients (S_A) and details coefficients (S_D) are acquired from DWT decomposition of the out-going currents at different conditions. S_A and S_D of bulk generator bus out-going currents are presented in Table 3.14 and 3.15 respectively.

Table 3.14 Values of S_A of bulk generator bus out-going currents in different conditions

DWT Decomposition Levels	S_A in Normal Condition	S_A for L-G fault in B-10	S_A for L-G fault in B-6
1	-0.00321	-0.002815	0.001007
2	-0.00321	-0.002816	0.001006
3	-0.00322	-0.002825	0.000997
4	-0.00323	-0.002836	0.000986
5	-0.003236	-0.002837	0.000986
6	-0.003322	-0.002928	0.0009
7	-0.000794	-0.000842	-0.00313
8	-0.038881	-0.038251	-0.0209
9	-1.631391	-1.619719	-1.54512

Table 3.15 Values of S_D of bulk generator bus out-going currents in different conditions

DWT Decomposition Levels	S_D in Normal Condition	S_D for L-G fault in B-10	S_D for L-G fault in B-6
1	-5.111591	-5.190263	-5.218738
2	-26.41396	-26.46912	-26.63336
3	-29.06973	-29.17678	-28.92876
4	-0.610926	-0.613237	-0.697516
5	4.9138013	4.9173088	4.829523
6	0.2446742	0.2438877	0.230333
7	0.0019211	0.0019353	-0.000207
8	0.0068734	0.0066633	0.002294
9	0.0020294	0.0018184	0.005714

Values of S_A and S_D of bulk generator bus out-going currents are graphically represented in Fig. 3.20 given below.

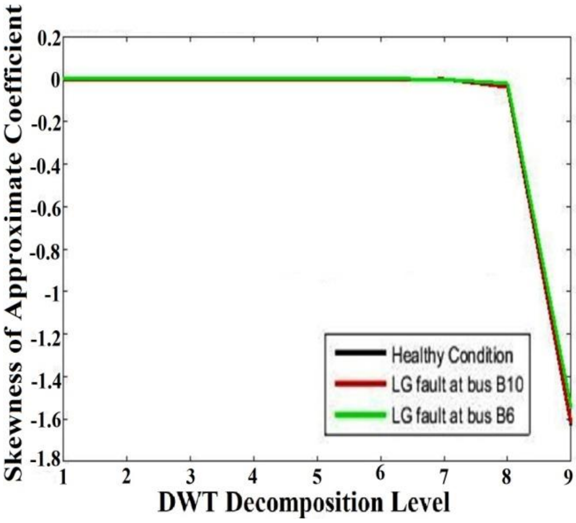

3.20(a)

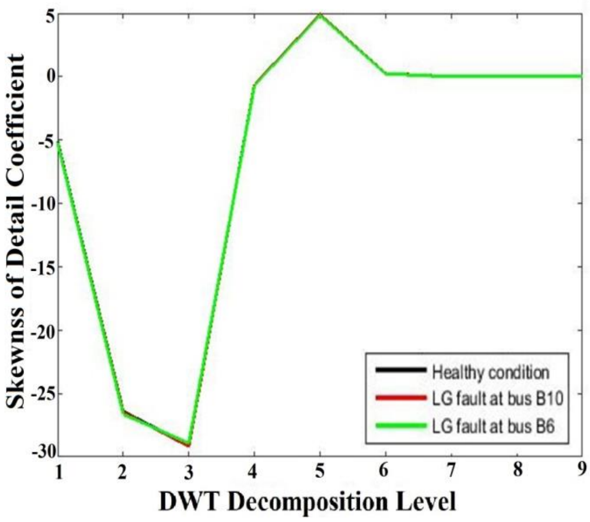

3.20 (b)

Fig. 3.20: (a) S_A and **(b)** S_D of bulk generator bus out-going currents

Values in S_A and S_D of PV Cell bus out-going currents are presented in Table 3.16 and 3.17 respectively.

Table 3.16 Values of S_A of PV Cell bus out-going currents in different conditions

DWT Decomposition Levels	S_A in Normal Condition	S_A for L-G fault in B-10	S_A for L-G fault in B-6
1	0.020065	0.014092	-0.141755
2	0.020066	0.0140938	-0.141755
3	0.020086	0.0141146	-0.141737
4	0.020115	0.0141447	-0.141705
5	0.020122	0.0141516	-0.141738
6	0.020372	0.0145358	-0.141972
7	0.021064	0.00770101	-0.186132
8	0.017331	0.00738380	-0.521970
9	-2.09286	-2.0544134	0.061531

Table 3.17 Values of S_D of PV Cell bus out-going currents in different conditions

DWT Decomposition Levels	S_D in Normal Condition	S_D for L-G fault in B-10	S_D for L-G fault in B-6
1	0.000253	0.000237	0.000169
2	0.893893	1.036576	0.503705
3	1.383794	1.540330	0.618097
4	0.162526	0.182866	0.111661
5	-0.16058	-0.19251	-0.20769
6	-0.08867	-0.08599	-0.05652
7	-0.01952	-0.01741	0.010429
8	-0.00229	-0.01152	0.030788
9	0.012409	-0.00030	-0.05113

Values of S_A and S_D of PV Cell bus out-going currents are graphically represented in Fig. 3.21 given below.

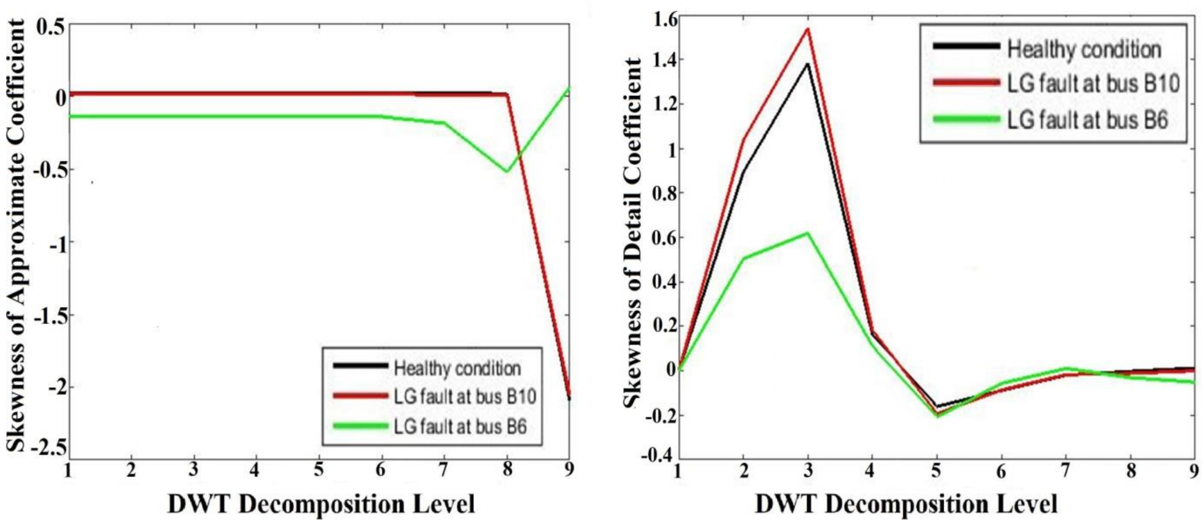

3.21(a) **3.21(b)**

Fig. 3.21: (a) S_A and **(b)** S_D of PV Cell bus out-going currents

Values in S_A and S_D of Diesel Generator 1 (DG-1) bus out-going currents are presented in Table 3.18 and 3.19 respectively.

Table 3.18 Values of S_A of Diesel Generator 1 (DG-1) bus out-going currents in different conditions

DWT Decomposition Levels	S_A in Normal Condition	S_A for L-G fault in B-10	S_A for L-G fault in B-6
1	-0.118492	-0.124689	-0.209764
2	-0.118492	-0.124689	-0.209764
3	-0.118492	-0.124689	-0.209765
4	-0.118492	-0.124689	-0.209764
5	-0.118491	-0.124688	-0.209762
6	-0.118580	-0.124781	-0.209836
7	-0.117041	-0.123943	-0.224723
8	-0.862525	-0.885866	-0.992595
9	-2.724684	-2.705611	-2.153905

Table 3.19 Values of S_D of Diesel Generator 1 (DG-1) bus out-going currents in different conditions

DWT Decomposition Levels	S_D in Normal Condition	S_D for L-G fault in B-10	S_D for L-G fault in B-6
1	0.112880	0.113882	0.112175
2	0.218731	0.226977	-0.00979
3	1.155593	1.229759	0.798434
4	-0.21969	-0.28423	-0.14522
5	-0.12489	-0.13449	-0.37739
6	-0.01299	-0.01036	-0.01833
7	-0.01072	-0.00795	0.011930
8	0.017485	0.016856	0.001402
9	0.059639	0.058663	0.064959

Values of S_A and S_D of Diesel Generator 1 (DG-1) bus out-going currents are graphically represented in Fig. 3.22 given below.

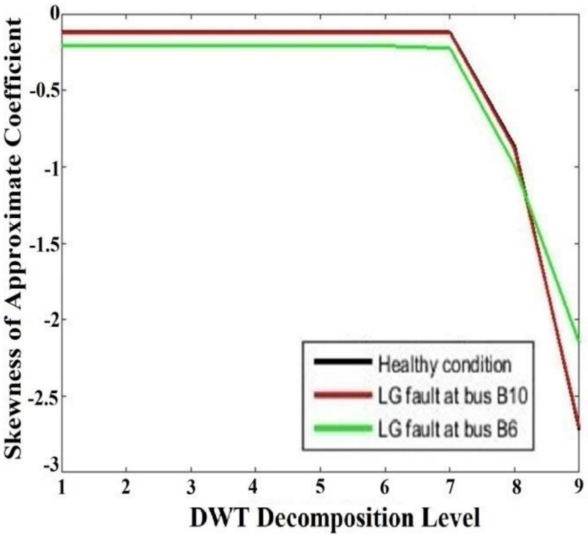

3.22(a)

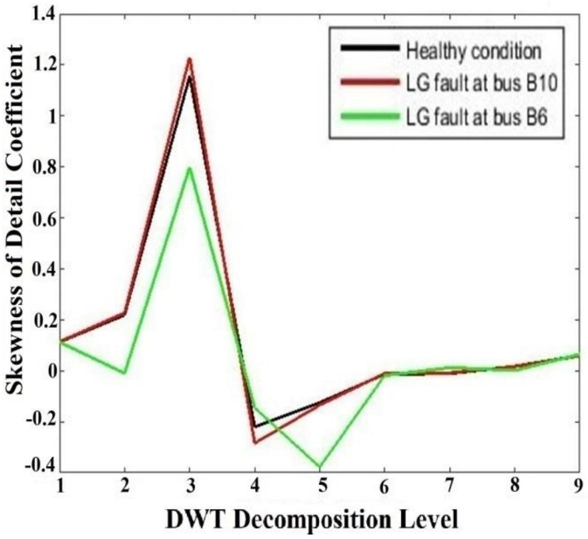

3.22(b)

Fig. 3.22: (a) S_A and **(b)** S_D of Diesel Generator 1 (DG-1) bus out-going currents

Values in S_A and S_D of Diesel Generator 2 (DG-2) bus out-going currents are presented in Table 3.20 and 3.21 respectively.

Table 3.20 Values of S_A of Diesel Generator 2 (DG-2) bus out-going currents in different conditions

DWT Decomposition Levels	S_A in Normal Condition	S_A for L-G fault in B-10	S_A for L-G fault in B-6
1	0.074092	0.074023	0.074088
2	0.074096	0.074027	0.074093
3	0.074121	0.074052	0.074118
4	0.074146	0.074077	0.074143
5	0.074092	0.074023	0.07409
6	0.073395	0.073326	0.073398
7	0.076965	0.07683	0.076423
8	1.347537	1.346999	1.345278
9	5.037982	5.037908	5.040535

Table 3.21 Values of S_D of Diesel Generator 2 (DG-2) bus out-going currents in different conditions

DWT Decomposition Levels	S_D in Normal Condition	S_D for L-G fault in B-10	S_D for L-G fault in B-6
1	-0.0101	-0.0119	-0.0091
2	-9.9876	-10.005	-9.8015
3	-26.443	-26.573	-26.446
4	2.13731	2.13526	2.22922
5	2.94884	2.94851	2.95578
6	0.07626	0.0762	0.07546
7	-0.0015	-0.0014	-0.0023
8	0.00686	0.00681	0.00666
9	-0.014	-0.014	-0.013

Values of S_A and S_D of Diesel Generator 2 (DG-2) bus out-going currents are graphically represented in Fig. 3.23 given below.

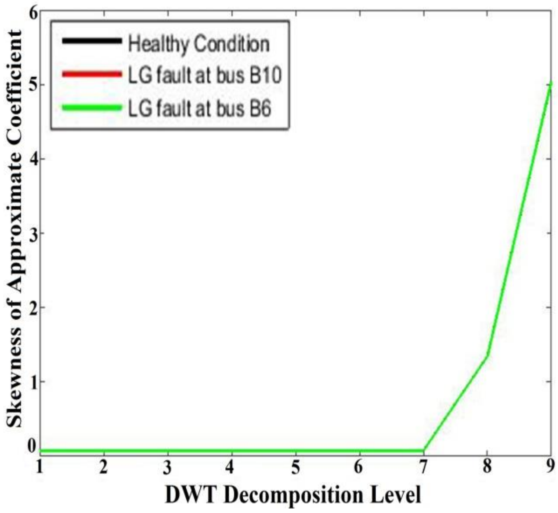

3.23(a)

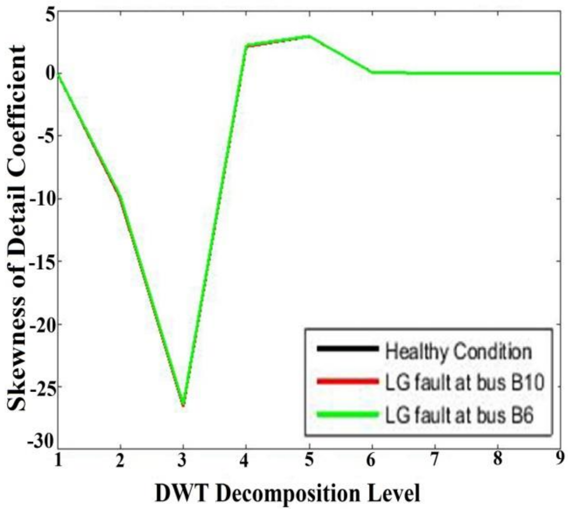

3.23(b)

Fig. 3.23: (a) S_A and **(b)** S_D of Diesel Generator 2 (DG-2) bus out-going currents

3.6.3 DWT based kurtosis value comparison

For every generator bus kurtosis of approximate coefficients (K_A) and details coefficients (K_D) are acquired from DWT decomposition of the out-going currents at different conditions. K_A and K_D of bulk generator bus out-going currents are presented in Table 3.22 and 3.23 respectively.

Table 3.22 Values of S_A of bulk generator bus out-going currents in different conditions

DWT Decomposition Levels	K_A in Normal Condition	K_A for L-G fault in B-10	K_A for L-G fault in B-6
1	1.531025	1.530954	1.536128
2	1.531026	1.530954	1.536128
3	1.531022	1.530951	1.536125
4	1.531023	1.530952	1.536126
5	1.53108	1.531008	1.536178
6	1.53233	1.532254	1.537299
7	1.660443	1.531008	1.668288
8	1.864604	1.532254	1.858123
9	6.629905	1.660301	6.384423

Table 3.23 Values of K_D of bulk generator bus out-going currents in different conditions

DWT Decomposition Levels	K_D in Normal Condition	K_D for L-G fault in B-10	K_D for L-G fault in B-6
1	1432.2182	1459.7879	1433.9772
2	4003.4216	4014.5174	4027.6859
3	1644.9619	1653.0373	1635.81
4	605.2368	607.44979	602.0019
5	182.55724	182.7254	178.69004
6	4.382273	4.3723058	4.2114371
7	1.810483	1.8105862	1.8184565
8	1.914653	1.9146983	1.9251367
9	1.842204	1.8420638	1.8496452

Values of K_A and K_D of bulk generator bus out-going currents are graphically represented in Fig. 3.24 given below.

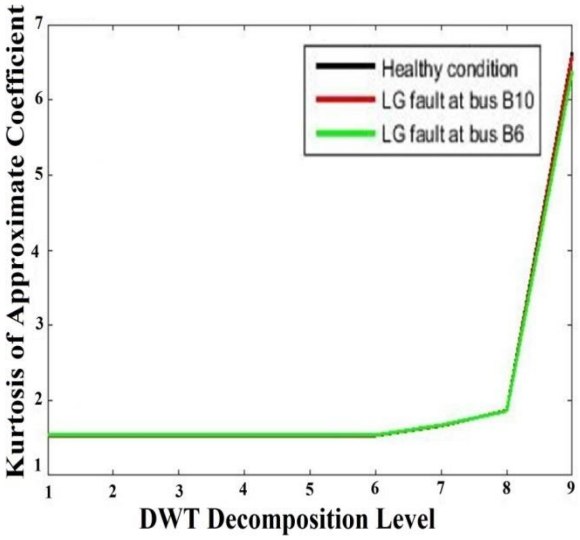

3.24(a)

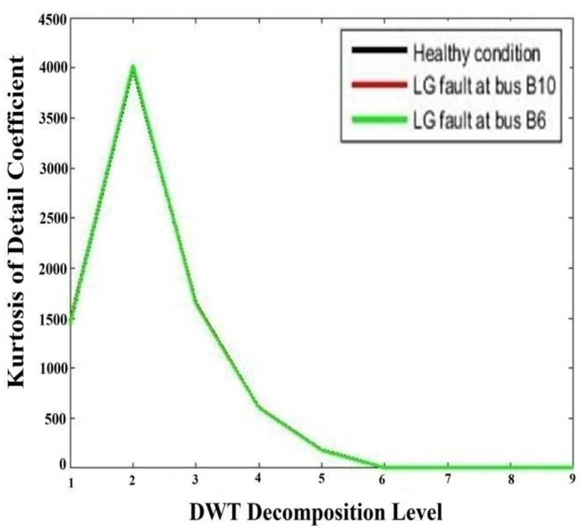

3.24(b)

Fig. 3.24: (a) K_A and **(b)** K_D of bulk generator bus out-going currents

Values in K_A and K_D of PV Cell bus out-going currents are presented in Table 3.24 and 3.25 respectively.

Table 3.24 Values of K_A of PV Cell bus out-going currents in different conditions

DWT Decomposition Levels	K_A in Normal Condition	K_A for L-G fault in B-10	K_A for L-G fault in B-6
1	1.531557	1.552359	1.755400
2	1.531556	1.5523585	1.755399
3	1.531539	1.5523396	1.755366
4	1.531527	1.5523217	1.755342
5	1.531717	1.5524868	1.755498
6	1.533962	1.5546058	1.756961
7	1.638494	1.6554564	1.861974
8	2.004640	2.0795917	3.540747
9	8.029416	8.0128110	4.137452

Table 3.25 Values of K_D of PV Cell bus out-going currents in different conditions

DWT Decomposition Levels	K_D in Normal Condition	K_D for L-G fault in B-10	K_D for L-G fault in B-6
1	1.037749	1.049369	1.159159
2	129.5949	148.7196	71.63288
3	58.12038	65.77484	33.51641
4	13.51176	16.62983	16.22892
5	6.058103	7.547240	7.079476
6	4.548036	4.961729	4.918043
7	1.912964	1.932182	2.271467
8	1.931419	1.947305	2.303672
9	1.867205	1.911355	3.046855

Values of K_A and K_D of PV Cell bus out-going currents are graphically represented in Fig. 3.25 given below.

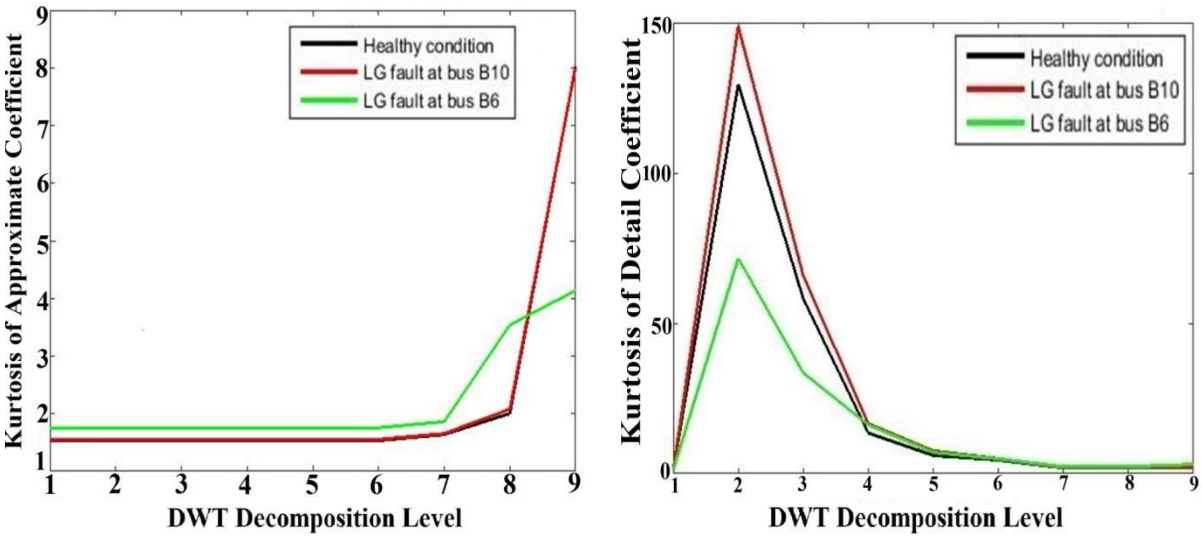

3.25(a) **3.25(b)**

Fig. 3.25: (a) K_A and **(b)** K_D of PV Cell bus out-going currents

Values in K_A and K_D of Diesel Generator 1 (DG-1) bus out-going currents are presented in Table 3.26 and 3.27 respectively.

Table 3.26 Values of K_A of Diesel Generator 1 (DG-1) bus out-going currents in different conditions

DWT Decomposition Levels	K_A in Normal Condition	K_A for L-G fault in B-10	K_A for L-G fault in B-6
1	1.900491	1.917519	2.0712466
2	1.900489	1.917519	2.0712462
3	1.900488	1.917517	2.0712449
4	1.900486	1.917515	2.0712418
5	1.900519	1.917549	2.0712582
6	1.902483	1.919587	2.0729035
7	1.981913	1.998469	2.1501003
8	4.126498	4.190374	4.3720811
9	10.67707	10.49652	8.3324921

Table 3.27 Values of K_D of Diesel Generator 1 (DG-1) bus out-going currents in different conditions

DWT Decomposition Levels	K_D in Normal Condition	K_D for L-G fault in B-10	K_D for L-G fault in B-6
1	477.684555	479.742204	476.469556
2	158.951951	164.541045	132.641762
3	106.341700	114.059899	91.1167610
4	14.2018668	16.7118883	22.1017647
5	3.90244973	4.01568294	8.03770022
6	2.35250157	2.34333922	2.45944139
7	1.83710304	1.83818579	1.92245458
8	1.91075222	1.91150639	1.98397564
9	1.87725151	1.87740269	1.97669764

Values of K_A and K_D of Diesel Generator 1 (DG-1) bus out-going currents are graphically represented in Fig. 3.26 given below.

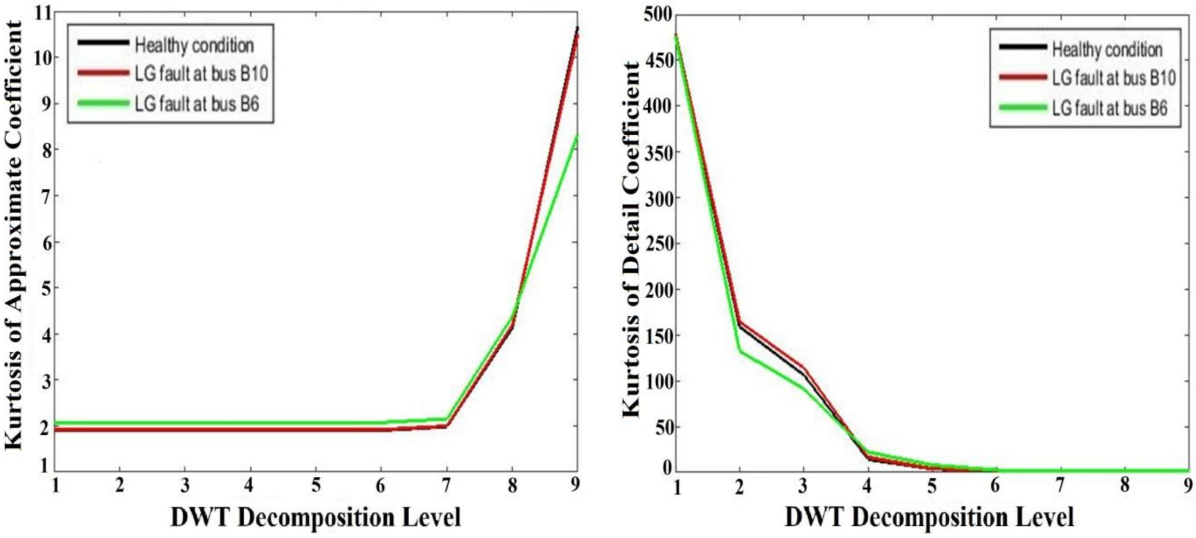

3.26(a) **3.26(b)**

Fig. 3.26: (a) K_A and **(b)** K_D of Diesel Generator (DG-1) bus out-going currents

Values in K_A and K_D of Diesel Generator 2 (DG-2) bus out-going currents are presented in Table 3.28 and 3.29 respectively.

Table 3.28 Values of K_A of Diesel Generator 2 (DG-2) bus out-going currents in different conditions

DWT Decomposition Levels	K_A in Normal Condition	K_A for L-G fault in B-10	K_A for L-G fault in B-6
1	1.7441	1.7439	1.74343
2	1.74412	1.74391	1.74344
3	1.74419	1.74399	1.74352
4	1.74426	1.74406	1.74359
5	1.74409	1.74389	1.74342
6	1.74212	1.74191	1.74142
7	1.87258	1.87239	1.87206
8	8.211043	8.207943	8.190337
9	30.12842	30.12777	30.14393

Table 3.29 Values of K_D of Diesel Generator 2 (DG-2) bus out-going currents in different conditions

DWT Decomposition Levels	K_D in Normal Condition	K_D for L-G fault in B-10	K_D for L-G fault in B-6
1	4.79641	7.08527	5.76519
2	2467.57	2469.57	2449.61
3	1420.05	1429.81	1419.46
4	592.627	592.606	595.051
5	93.7179	93.7054	93.8841
6	2.71572	2.71618	2.72137
7	1.85696	1.85697	1.8566
8	1.91746	1.91748	1.91816
9	1.856	1.85591	1.85519

Values of K_A and K_D of Diesel Generator 2 (DG-2) bus out-going currents are graphically represented in Fig. 3.27 given below.

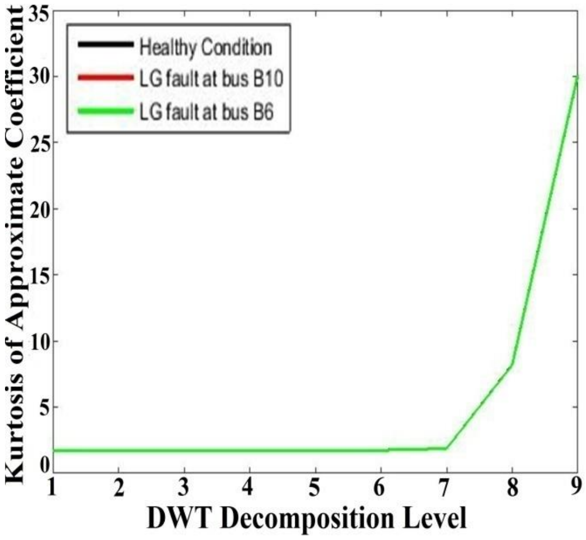

3.27(a)

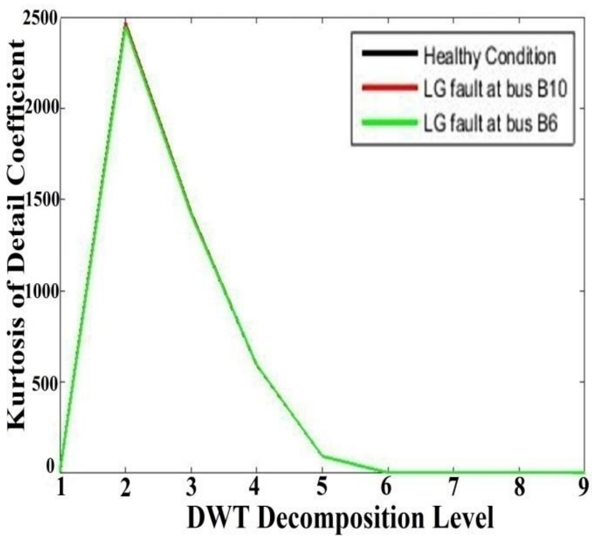

3.27(b)

Fig. 3.27: (a) K_A and **(b)** K_D of Diesel Generator (DG-2) bus out-going currents

3.7 Observations from DWT based Analysis

Several observations can be made from the results of DWT based statistical parameter analysis presented in the earlier sections.

3.7.1 General Consideration

Existence of higher and lower order harmonics inside a signal results in high values of RMS_A and RMS_D respectively. Lack of symmetry in distribution of approximate and details coefficients cause the value of skewness to deviate from zero. Whereas, peakedness of the distribution of approximate and details coefficients decide the kurtosis values.

It is clear from Fig. 3.16 – 3.27 that with occurrence of L-G fault at bus B-10 and B-6, different parameters of particular generator bus current experiences different values of deviations from their own values at normal condition. Hence, the place of occurrence of the L-G fault can be determined by the degree of deviation experienced by these parameters. Calculation of percentage deviation of different parameters from their respective normal condition value is done with the help of equation (3.2) given below.

$$\%\ \text{Deviation} = \left|\frac{(\text{Healthy value}) - (\text{Faulty value})}{\text{Healthy value}}\right| \times 100 \tag{3.2}$$

3.7.2 Percentage Deviation of Six Parameters of Bulk Generator Bus

Percentage deviation of six parameters (RMS_A, RMS_D, S_A, S_D, K_A and K_D) of bulk generator bus out-going current are calculated for occurrence of L-G fault at B-10 and B-6 using equation (3.2) and shown below in Fig. 3.28. Here, x-axis represents the percentage deviation of the aforementioned parameters from their respective normal condition values and y-axis DWT decomposition levels.

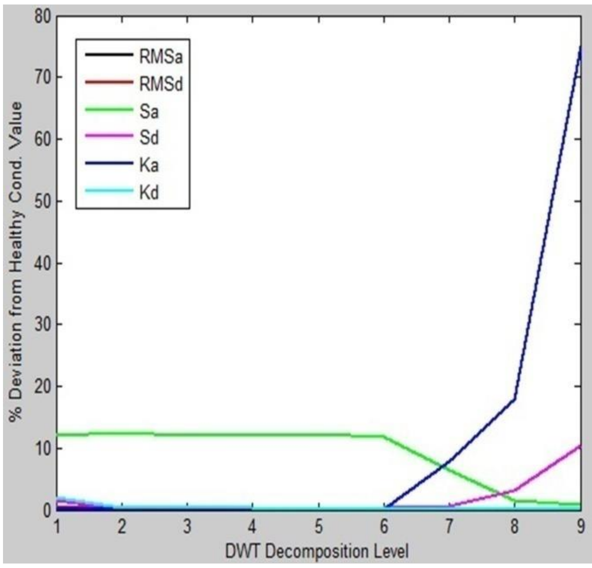

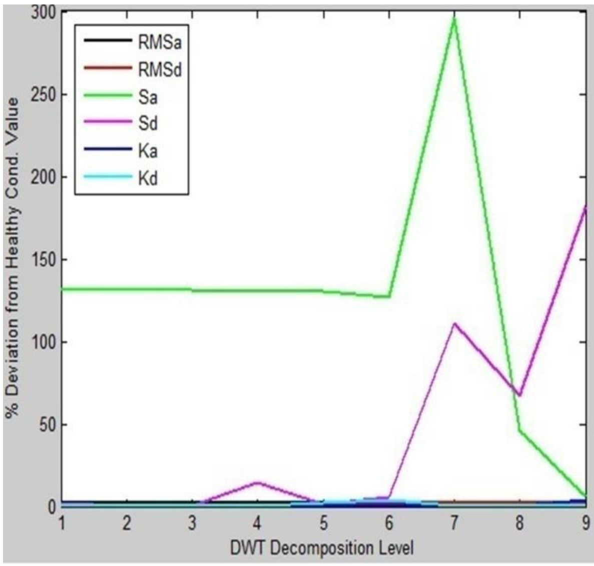

3.28(a) **3.28(b)**

Fig. 3.28: Comparison of % deviations of different parameters of Bulk Generator bus for **(a)** L-G fault at B-10 and **(b)** L-G fault at B-6

From Fig. 3.28(a) it is seen that K_A has the maximum value of deviation from normal condition value at 9^{th} level of decomposition but from Fig 3.28(b) it observed that amongst all the six parameters, S_A possesses maximum deviation at 7^{th} level. So, maximum amount of deviation in K_A at 9^{th} level of bulk generator bus suggests occurrence of L-G fault at B-10 and maximum deviation of S_A at 7^{th} level indicates occurrence of L-G fault at B-6.

3.7.3 Percentage Deviation of Six Parameters of PV Cell Bus

Percentage deviation of six parameters (RMS_A, RMS_D, S_A, S_D, K_A and K_D) of PV Cell bus out-going current are calculated for occurrence of L-G fault at B-10 and B-6 using equation (3.2) and shown below in Fig. 3.29. Here, x-axis represents the percentage deviation of the aforementioned parameters from their respective normal condition values and y-axis DWT decomposition levels.

Fig. 3.29(a) given shows that amongst all the six parameters, L-G fault at B-10 cause maximum deviation in S_D at 8^{th} level and Fig. 3.29 (b) shows that L-G fault at B-6 causes maximum deviation in S_A at 8^{th} level of decomposition.

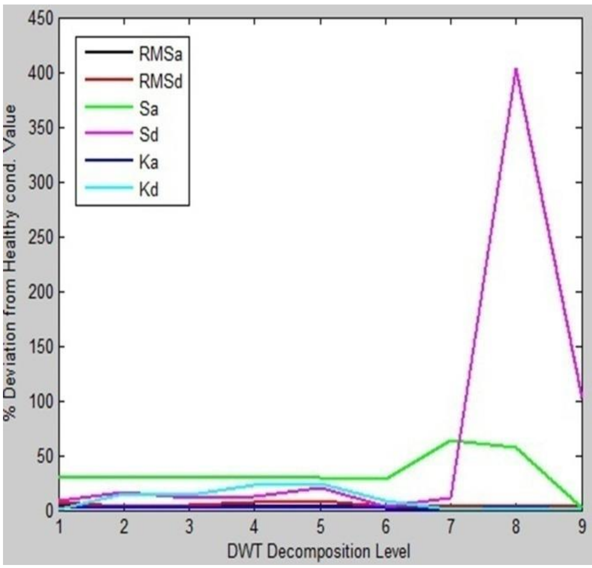

3.29(a)

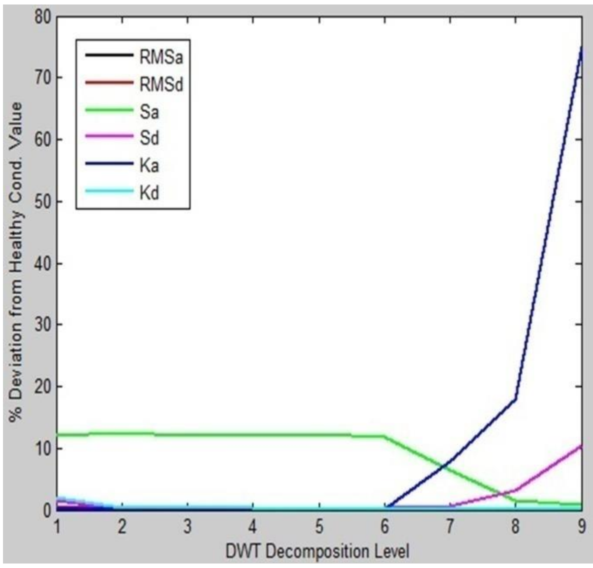

3.29(b)

Fig. 3.29: Comparison of % deviations of different parameters of PV Cell bus for **(a)** L-G fault at B-10 and **(b)** L-G fault at B-6

So, maximum deviation of S_D of the out-going current of PV Cell bus at 8th level indicates L-G fault at B-10 and maximum deviation in S_A at 8th level indicates L-G fault at B-6.

3.7.4 Percentage Deviation of Six Parameters of Diesel Generator 1 (DG-1) Bus

Percentage deviation of the six different parameters of DG-1 bus out-going current are calculated for occurrence of L-G fault at B-10 and B-6 using equation (3.2) and presented below in in Fig. 3.30. Here, x-axis represents the percentage deviation of the aforementioned parameters from their respective normal condition values and y-axis DWT decomposition levels.

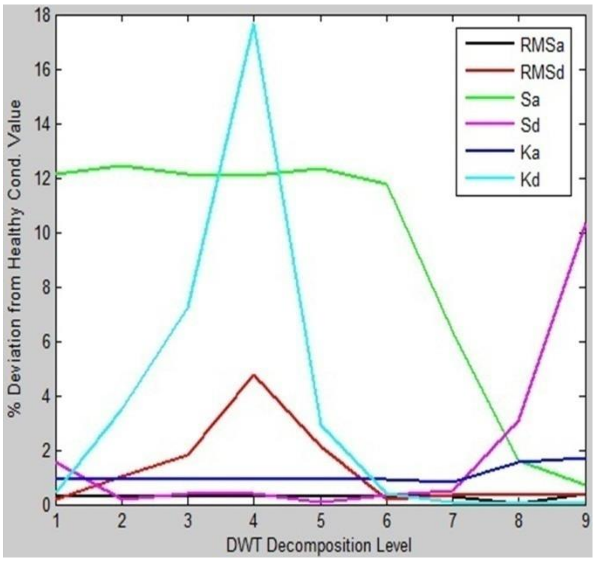

3.30(a)

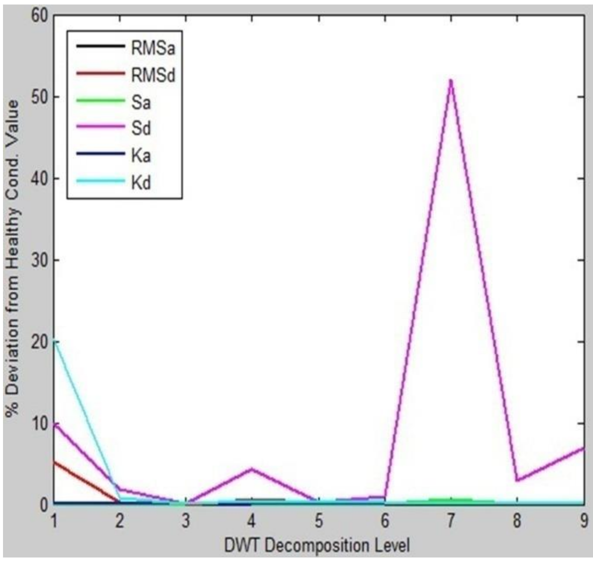

3.30(b)

Fig. 3.30: Comparison of % deviations of different parameters of DG-1 bus for **(a)** L-G fault at B-10 and **(b)** L-G fault at B-6

Fig. 3.30(a) shows that in comparison with the other parameters, K_D has the highest amount of deviation at 4th level of decomposition and Fig. 3.30 (b) shows that deviation in S_A is the maximum at 7th level. Hence, for DG-1 bus, highest deviation in K_D at 4th level indicates L-G fault at B-10 and highest deviation in S_A at 7th level suggests L-G fault at B-6.

3.7.5 Percentage Deviation of Six Parameters of Diesel Generator 2 (DG-2) Bus

Percentage deviation of the six different parameters of DG-2 bus out-going current are calculated for occurrence of L-G fault at B-10 and B-6 using equation (3.2) and presented below in Fig. 3.31. Here, x-axis represents the percentage deviation of the aforementioned parameters from their respective normal condition values and y-axis DWT decomposition levels.

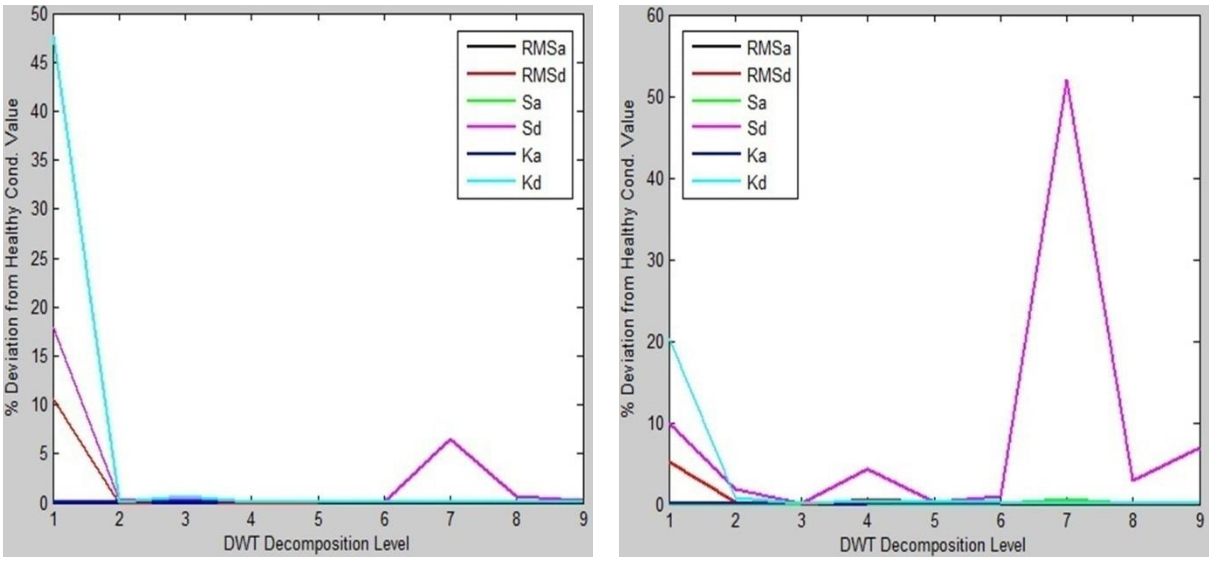

3.31(a) **3.31(b)**

Fig. 3.31: Comparison of % deviations of different parameters of DG-2 bus for **(a)** L-G fault at B-10 and **(b)** L-G fault at B-6

From Fig. 3.31 (a) it is observed that occurrence of L-G fault at B-10 cause appreciable amount of deviation of RMS_D, S_D and K_D at 1st level of decomposition. However, in comparison with all the parameters, K_D exhibits the maximum deviation at 1st level. Fig. 3.31(b) shows that occurrence of L-G fault at B-6 results into the maximum percentage deviation in S_D at 7th level. Hence, for DG-2 bus, highest deviation in K_D at 1st level indicates L-G fault at B-10 and highest deviation in S_D at 7th level suggests L-G fault at B-6.

3.8 Outcome of parametric & level optimization of statistical parameters

In the preceding section, optimization of both parameters and levels for six statistical parameters derived from DWT analysis of out-going currents from various generator buses under different conditions was conducted. It is observed that, under a specific condition, a particular statistical parameter for a given generator bus current exhibits the highest percentage deviation from its normal condition value. The outcomes of this parameter and level optimization are presented in Table 3.30 below, in the form of a rule set. This rule set helps to detect L-G fault locations by observing the out-going current of any generator bus.

Table 3.30 Rule Set

Observation from	Parameter	Level	Indication
Bulk Generator	Highest percentage deviation in K_A	9	L-G fault at B-10 bus
	Highest percentage deviation in S_A	7	L-G fault at B-6 bus
PV Cell	Highest percentage deviation in S_D	8	L-G fault at B-10 bus
	Highest percentage deviation in S_A	8	L-G fault at B-6 bus
DG-1	Highest percentage deviation in K_D	4	L-G fault at B-10 bus
	Highest percentage deviation in S_A	7	L-G fault at B-6 bus
DG-2	Highest percentage deviation in K_D	1	L-G fault at B-10 bus
	Highest percentage deviation in S_D	7	L-G fault at B-6 bus

3.9 Summary

This study introduces a technique utilizing FFT and DWT to pinpoint the location of L-G faults. It is noticed that approaches relying solely on FFT yield inadequate outcomes, primarily due to the non-stationary characteristics of current signals under fault scenarios, which FFT struggles to handle effectively.

To address this, a statistical analysis based upon DWT is performed to the currents exiting various generator buses in different conditions. Percentage deviations are calculated for each statistical parameter, comparing normal and faulty condition values and based upon these calculations parametric and level optimization was done. The rule set presented here is derived from these optimizations.

To streamline the investigation, the analysis focused exclusively on L-G faults and concentrated on just two specific load bus: the furnace (B-6) and the non-linear load bus (B-10). Nevertheless, the methodology holds potential for broader application, encompassing diverse fault categories and the full array of generator and load buses within the microgrid system. Upon such expansion, the developed rule set could reliably identify both the occurrence and position of any fault throughout the microgrid network.

Compared to traditional approaches, the suggested technique provides multiple benefits. It functions independently of the voltage and current levels across the system. Moreover, changes in fault resistance have no impact on its performance. Consequently, arc resistances of ground faults do not influence the effectiveness of the outlined rules. This makes the technique particularly effective for identifying ground faults within microgrid networks. In addition, it supports fault identification from remote ends, given that faults were happening at load buses while monitoring occurred at the generator bus.

Publication:

S. Datta, A. Chattopadhyaya, S. Chattopadhayay & A. Das, "Harmonic Distortion, Inter-harmonic Group Magnitude and Discrete Wavelet Transformation based Statistical Parameter Estimation for Line to Ground Fault Analysis in Microgrid System", Michael Faraday International India Summit (MFIIS) 2020, Kolkata, 3rd & 4th October.

Chapter 4

S-Transform based Kurtosis Analysis for Detection of L-G and L-L Faults

The work presented here, shows a method for identifying fault locations and distinguishing fault types within a microgrid network. Stockwell Transform (S-Transform) based kurtosis analysis is performed and subsequently a unique algorithm is developed for this purpose.

4.1 Introduction

Faults detection in microgrid networks using traditional approaches is challenging due to their inherently low current magnitudes. Ground faults exacerbate this issue by causing chapter voltage reductions, which further complicates identification within these systems. This study introduces an innovative technique for identification of fault locations and classifying fault types. IEEE standard 14 bus microgrid network is utilized for this purpose. Faults are simulated at two designated load buses, followed by examination of the currents exiting from two generator buses during different conditions. The S-Transform is applied to these outgoing current signals and the kurtosis values derived from the resulting matrices are computed. An algorithm is developed to determine both the type and site of the faults. Its effectiveness is confirmed through testing in various unanticipated situations. All modelling and analysis are conducted via MATLAB on the IEEE standard 14 bus microgrid network. This strategy holds potential for enhancing protection schemes used in microgrid environments.

IEEE Standard 14 Bus Microgrid System is shown in Fig. 3.1. Line to Ground (L-G) fault is made between phase ‘C’ and ground on load bus B-10 (Non-linear load bus) and B-6 (furnace bus), one at a time; while the other load buses were left healthy. Similarly, Line to Line (L-L) fault is also made to occur between phase ‘B’ and phase ‘C’ of load bus B-10 and B-6 one at a time. Currents exiting from bulk generator and P-V Cell bus are examined from phase ‘C’ through the Data Capture Units (DCU). 1000 Hz of sampling frequency is taken to rule out any possibility of aliasing. With occurrence of fault the current waveform shifts from steady state to transient state. Once the fault is cleared, the current waveform again shifts back to its steady state. To fully examine this complete transition — from steady state through the transient state and back to steady state — the duration of the fault is constrained to be 0.15 – 0.35 seconds. The total fault simulation time is set at 0.5 seconds. The simulation time has been deliberately shortened to minimize the amount of data produced.

4.2 Fault Classification using Kurtosis

The S-Transform analysis was conducted on the currents going out from phase ‘C’ of various generator buses across five distinct scenarios: healthy, L-G faults occurring at buses B-10 and B-6, and L-L faults at the same locations. Application of the S-Transform to these current signals produced corresponding S-transformation matrices, where the rows represent frequency and the columns indicate time. Following the computation of the S-Transformation of currents from the various generator buses, kurtosis was derived under each scenario. These kurtosis values were plotted against time. Resulting graphs demonstrating the variation in kurtosis values with respect to time are given below. Kurtosis vs. Time plots, derived from the S-Transform matrices of output currents from the bulk generator and P-V Cell bus under healthy condition, are given in Fig 4.1(a) and 4.1(b), respectively.

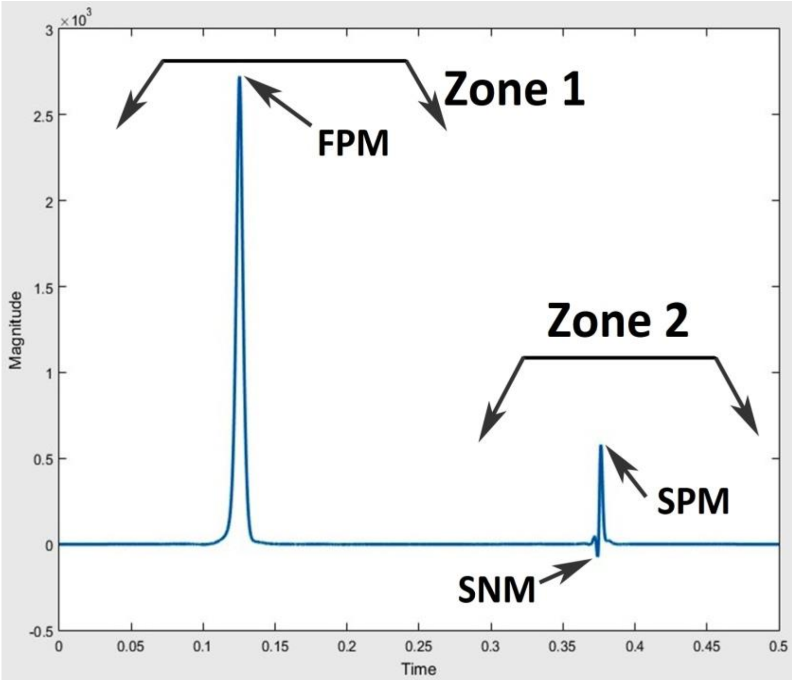

4.1(a)

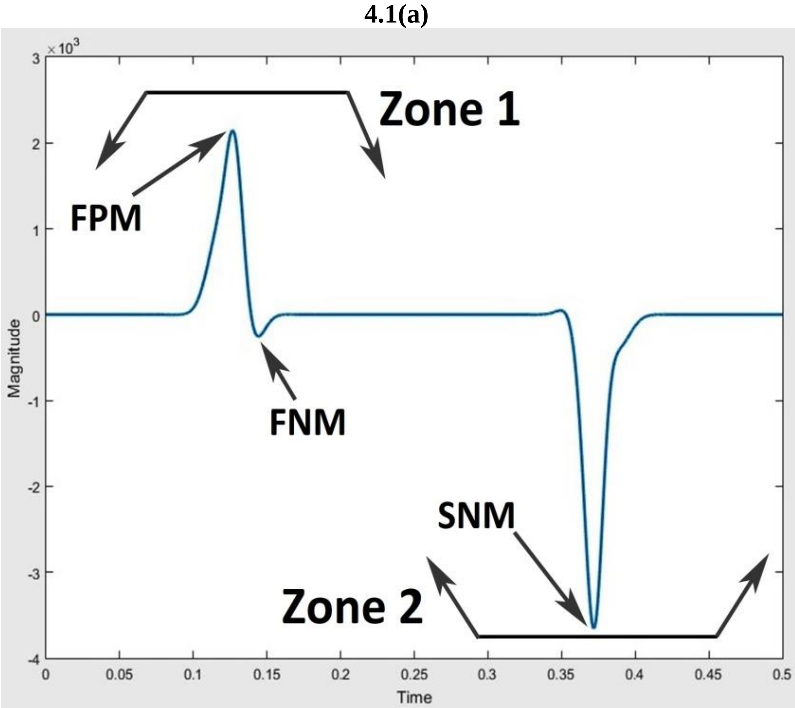

4.1(b)

Fig 4.1: Kurtosis vs. time (in seconds) plot of S – Transform results of outgoing currents from **(a)** bulk generator bus and **(b)** P-V Cell bus at healthy condition.

In Fig. 4.1(a) and 4.1(b), x – axis represent time in seconds and y – axis represent the kurtosis magnitudes. Analysis of Figures 4.1(a) and 4.1(b) indicates the presence of up to four distinct peaks in the waveforms: the first positive peak (F.P.P.), the first negative peak (F.N.P.), the second positive peak (S.P.P.), and the second negative peak (S.N.P.). Not all waveforms necessarily exhibit all four peaks. Additionally, these peaks are observed to occur within two clearly defined regions, referred to as Zone-1 and Zone-2, which are labelled in Fig. 4.1(a) and 4.1(b). Specifically, Fig. 4.1(a) displays the F.P.P., S.P.P., and S.N.P., while Figure 4.1(b) shows the F.P.P., F.N.P., and S.N.P.

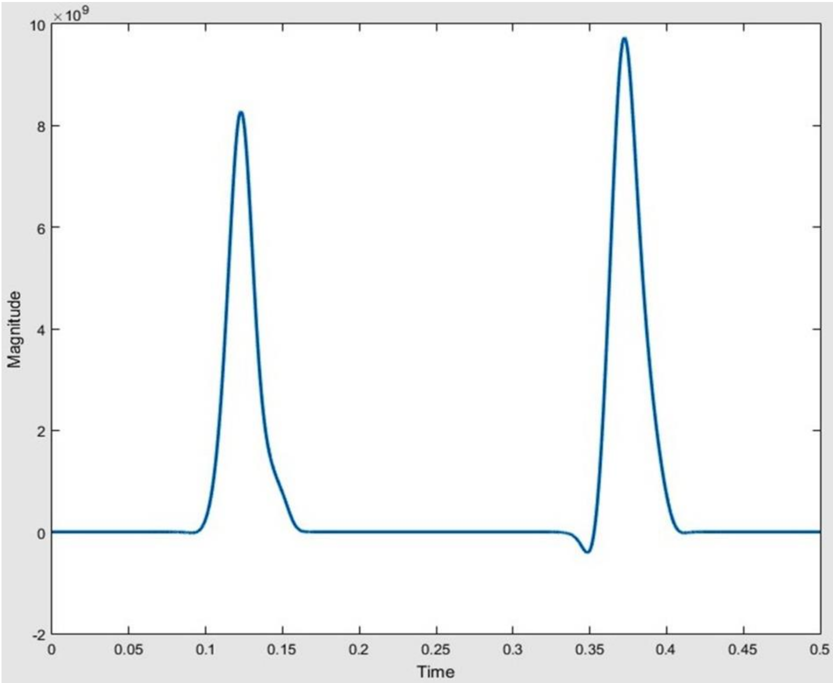

4.2(a)

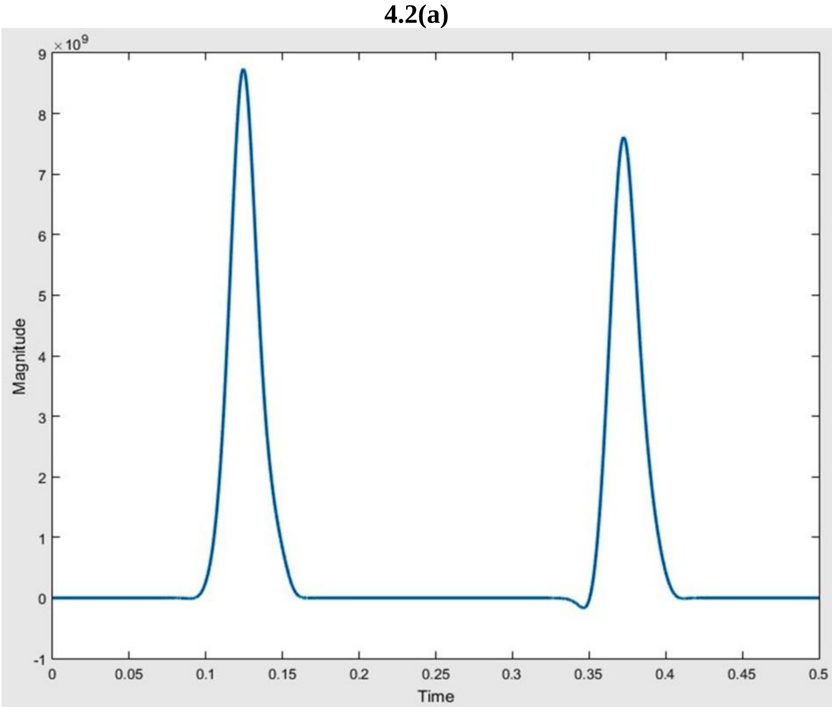

4.2(b)

Fig. 4.2: Kurtosis vs. time (in seconds) plot of S – Transform results of outgoing currents from bulk generator bus for **(a)** L-G at B-6 and **(b)** L-G at B-10

Fig. 4.2(a) and 4.2(b) show kurtosis vs. time plots of S – Transform matrices of outgoing currents from bulk generator bus when L-G fault occurs at B-6 and B-10 respectively.

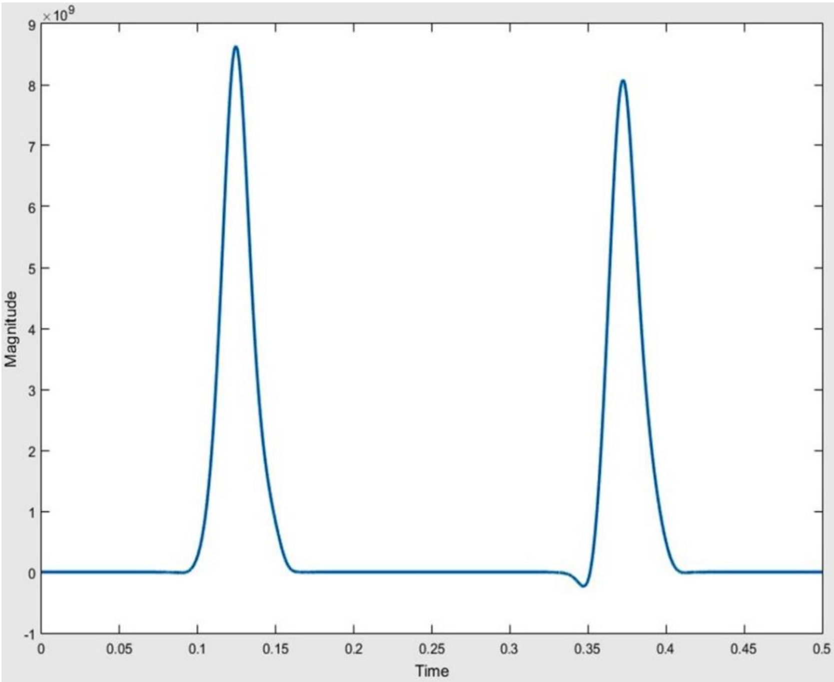

4.3(a)

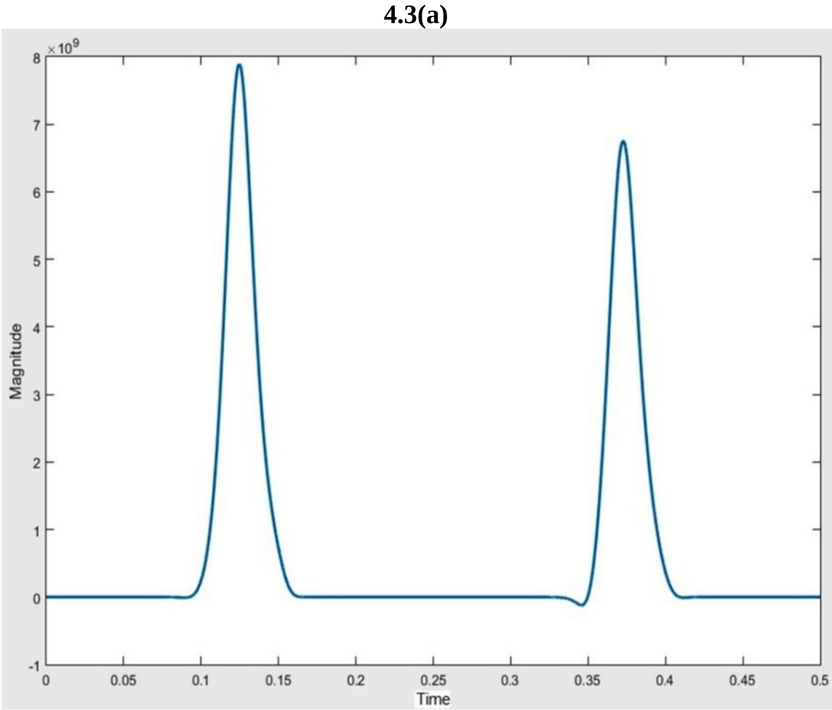

4.3(b)

Fig. 4.3: Kurtosis vs. time (in seconds) plot of S – Transform results of outgoing currents from bulk generator bus for **(a)** L-L at B-6 and **(b)** L-L at B-10

Kurtosis vs. time plots of S – Transform results of outgoing currents from bulk generator bus when L-L fault occurs at B-6 and B-10 are shown in Fig. 4.3(a) and 4.3(b) respectively. In the Kurtosis vs. time plot derived from the S-Transform of outgoing currents from the Bulk Generator bus, zone-1 exhibits a single peak, similar to the healthy condition. In contrast, zone-2 displays both a positive and a negative peak. Consequently, zone-1 yields only one parameter, F.P.M., while zone-2 provides two parameters, S.P.M. and S.N.M. Further analysis reveals that, despite the plots appearing quite similar across various fault conditions, the peak magnitudes show significant variations.

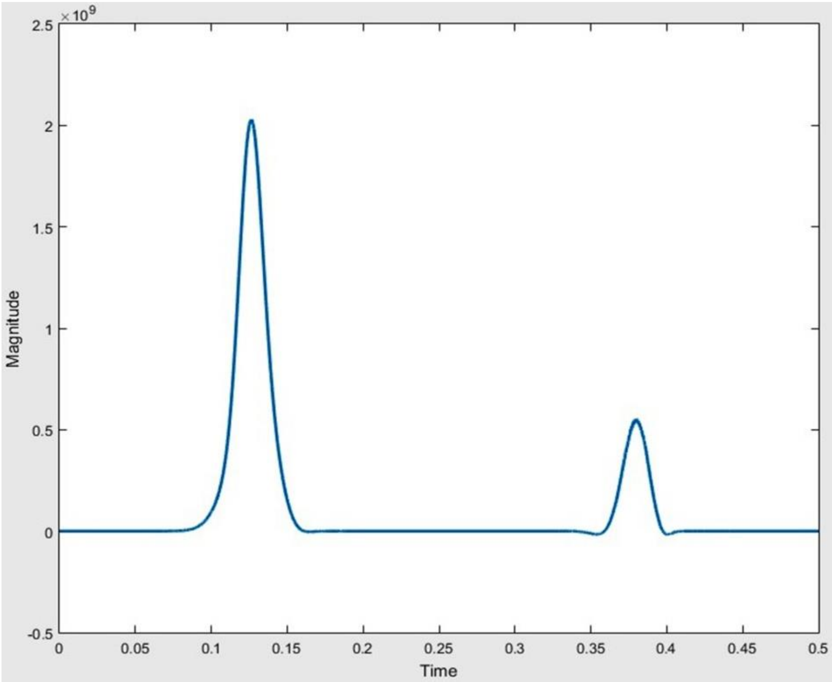

4.4(a)

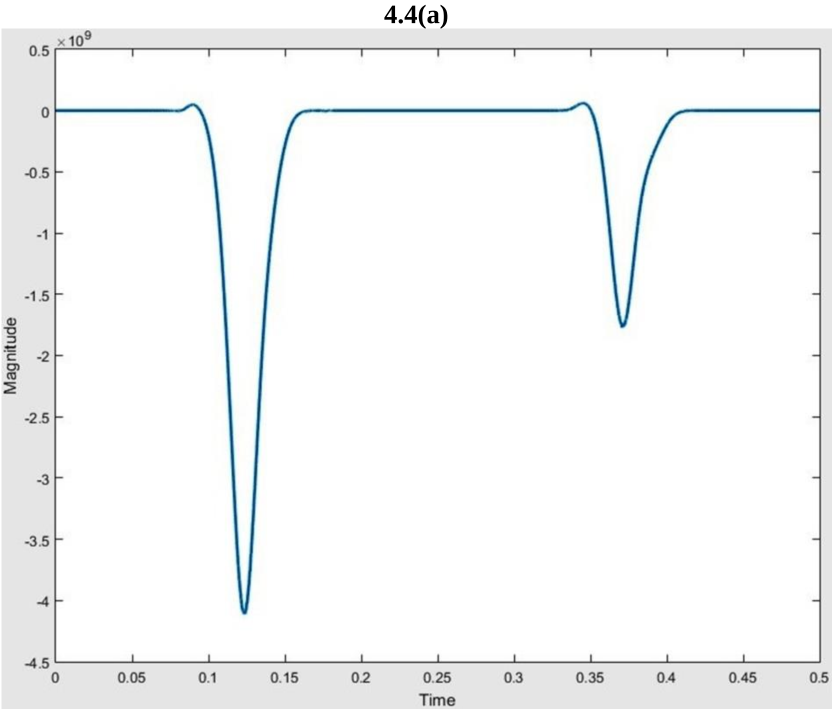

4.4(b)

Fig. 4.4: Kurtosis vs. time (in seconds) plot of S – Transform results of outgoing currents from P-V Cell bus for **(a)** L-G at B-6 and **(b)** L-G at B-10

In Fig. 4.4 (a) and 4.4 (b) kurtosis vs. time plots of S - Transform matrices of outgoing currents from PV Cell bus are depicted when L-G fault occurs at B-6 and B-10 respectively.

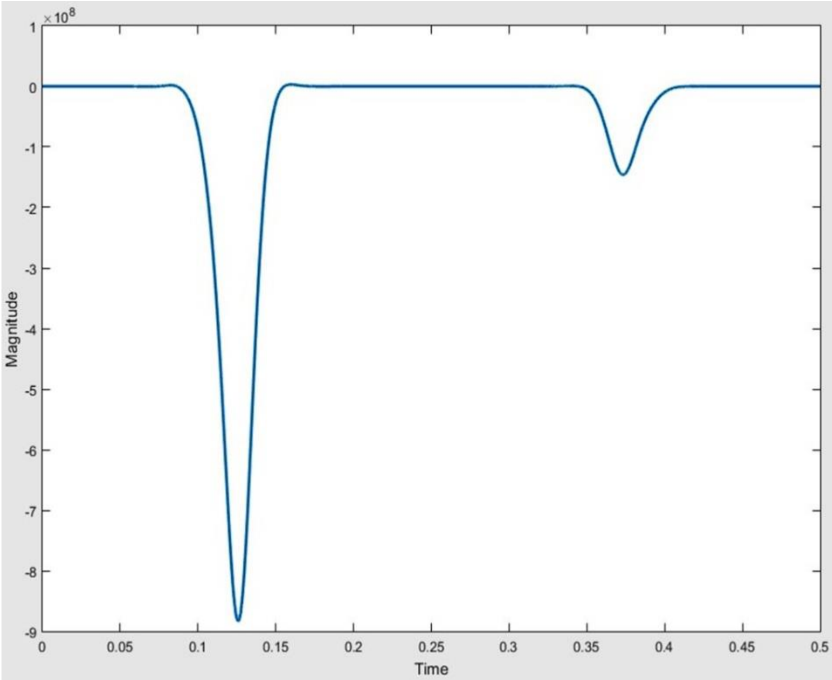

4.5(a)

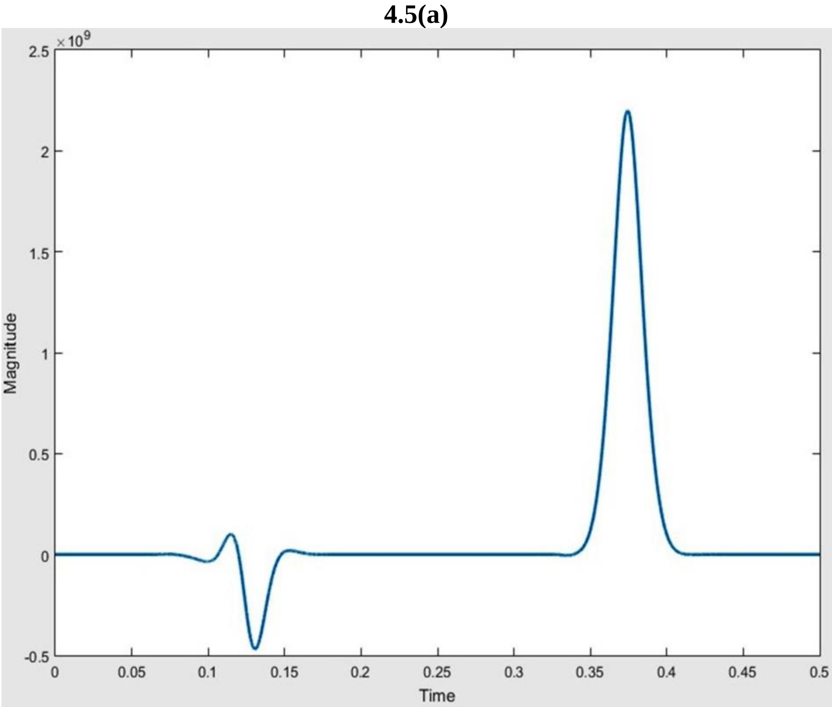

4.5(b)

Fig. 4.5: Kurtosis vs. time (in seconds) plot of S – Transform results of outgoing currents from P-V Cell bus for **(a)** L-L at B-6 and **(b)** L-L at B-10

Fig. 4.5(a) and 4.5(b) depicts kurtosis vs. time plots of S – Transformation results of outgoing currents from P-V Cell bus when L-L fault takes place at B-6 and B-10 respectively. The graphs exhibit unique characteristics, each showcasing distinct patterns that set them apart from one another. Additionally, the peak values of these plots vary significantly, reflecting substantial differences influenced by the specific conditions under which they were generated.

4.3 Establishment of Novel Parameters for Comparison

Based on the distinct characteristics of the graphs shown in the previous section, six novel parameters have been established.

First Positive Maximum (FPM):

The magnitude of the first positive peak of the graph is termed as the First Positive Peak (FPM).

First Negative Maximum (FNM):

The magnitude of the first negative peak of the graph is defined as the First Negative Peak (FNM).

Difference of First Zone Maximums (DZ_1)

It is the difference between FPM and FNM i.e.

$$\mathrm{DZ}_1 = (\mathrm{FPM} - \mathrm{FNM})$$

Second Positive Maximum (SPM)

The magnitude of the second positive peak of the graph is termed as the Second Positive Peak (SPM).

Second Negative Maximum (SNM)

The magnitude of the second negative peak of the graph is defined as the Second Negative Peak (SNM).

Difference of Second Zone Maximums (DZ_2)

It is the difference between SPM and SNM i.e.

$$\mathrm{DZ}_2 = (SPM - \mathrm{SNM})$$

The parameters FPM, FNM, and DZ_1 are derived from Zone-1, while SPM, SNM, and DZ_2 originate from Zone-2. In cases where one or two peaks are missing in a graph, the corresponding parameter values are set to zero; for instance, in Fig. 4.2 and 4.3, the absence of first negative maximums results in FNM being assigned a value of zero.

4.4 Discrimination between Healthy and Faulty conditions

In Table 4.1, FPM, FNM, DZ_1 values of bulk generator bus outgoing currents in different conditions have been presented.

Table 4.1 FPM, FNM, and DZ_1 Values of Outgoing Current from bulk generator bus

Condition		Zone-1		
		FPM	FNM	DZ_1
Healthy		2.72×10^3	0	2.72×10^3
LG	At B6	8.16×10^5	0	8.16×10^5
	At B10	8.73×10^5	0	8.73×10^5
LL	At B6	8.62×10^5	0	8.62×10^5
	At B10	8.52×10^5	0	8.52×10^5

Table 4.1 shows that in all instances, the FNM values are consistently zero, resulting in FPM and DZ1 values being equal to each other. The FPM values, corresponding to various conditions as listed in Table 4.1, are visually represented as a bar chart in Fig. 4.6.

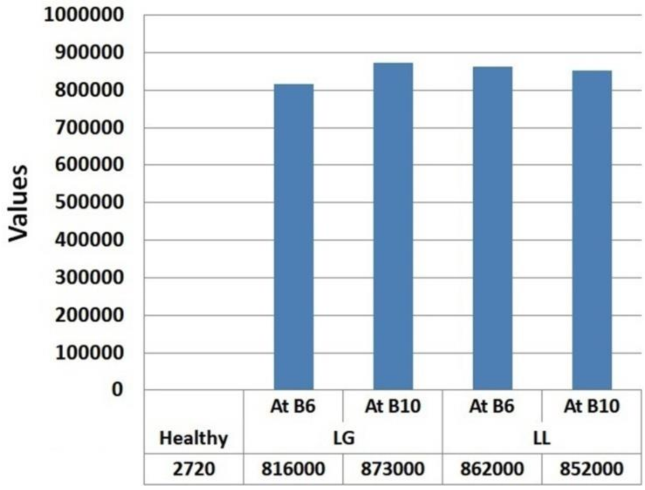

Fig. 4.6: FPM of bulk generator bus at different conditions

Table 4.2 shows, SPM, SNM and DZ_2 values of bulk generator bus outgoing currents in different conditions.

Table 4.2 SPM, SNM, and DZ_2 Values of Outgoing Current from bulk generator bus

Condition		Zone-1		
		SPM	SNM	DZ_2
Healthy		0.5×10^3	-0.007×10^3	0.507×10^3
LG	At B6	9.78×10^5	-0.34×10^5	10.12×10^5
	At B10	7.6×10^5	-0.28×10^5	7.88×10^5
LL	At B6	8.16×10^5	-0.30×10^5	8.46×10^5
	At B10	7.35×10^5	0	7.35×10^5

The SPM, SNM and DZ_2 values for different conditions given in Table 4.2; are plotted as a bar graph in Fig. 4.7, 4.8 and 4.9.

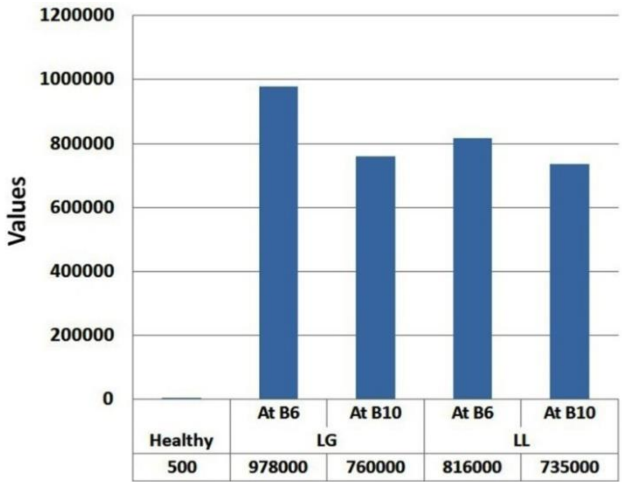

Fig. 4.7: SPM of bulk generator bus at different conditions

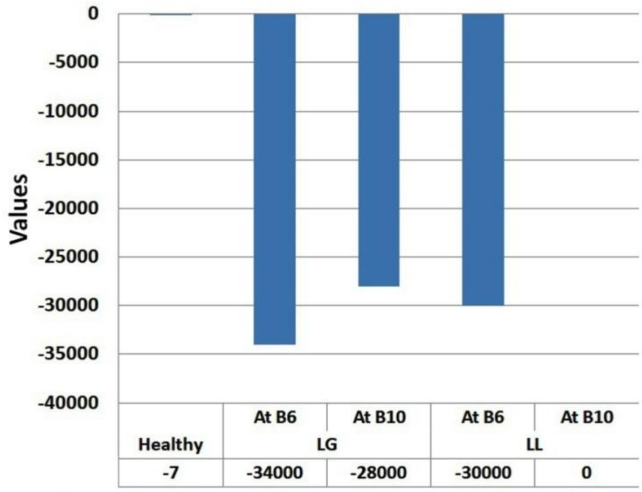

Fig. 4.8: SNP of bulk generator bus at different conditions

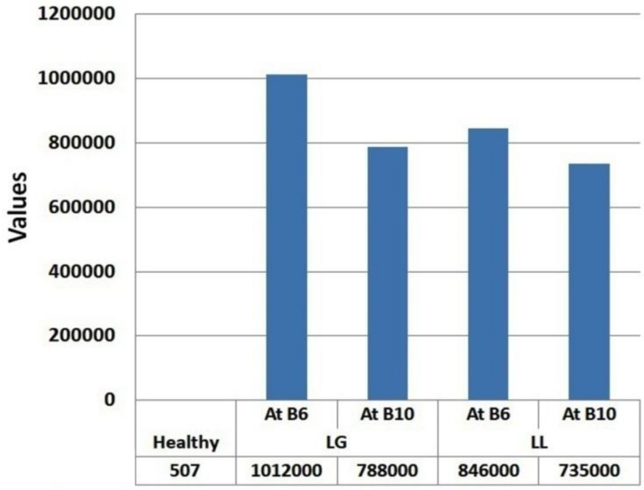

Fig. 4.9: DZ_2 of bulk generator bus at different conditions

Table 4.3 shown below lists the values of FPM, FNM and DZ_1 of P-V Cell bus outgoing currents, at different conditions.

Table 4.3 FPM, FNM, and DZ_1 Values of Outgoing Current from P-V Cell bus

Condition		Zone-1		
		FPM	FNM	DZ_1
Healthy		2.14×10^3	-0.25×10^3	2.39×10^3
LG	At B6	2.04×105	0	2.04×10^5
	At B10	0	-4.08×10^5	-4.08×10^5
LL	At B6	0	8.89×10^4	8.89×10^4
	At B10	0.09×10^5	-0.48×10^5	0.57×10^5

The data for FPP, FNP, and DZ_1 in various conditions, as presented in Table 4.3, are visually represented as a bar graph in Fig. 4.10, 4.11 and 4.12. This graphical depiction illustrates the variations in these parameters, providing a clear and comparative view of their values under different scenarios.

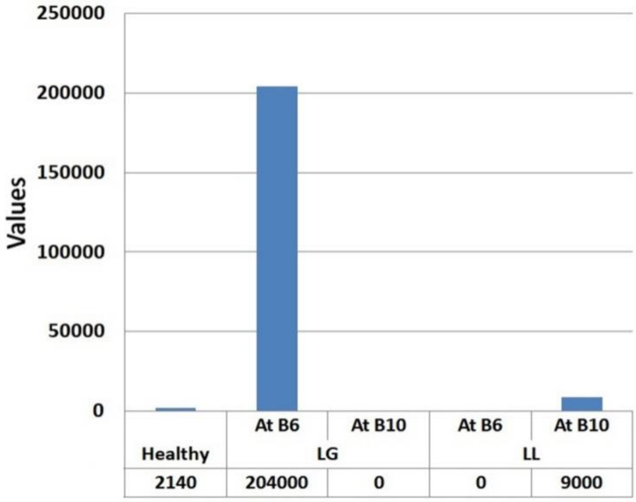

Fig. 4.10: FPM of P-V Cell bus at different conditions

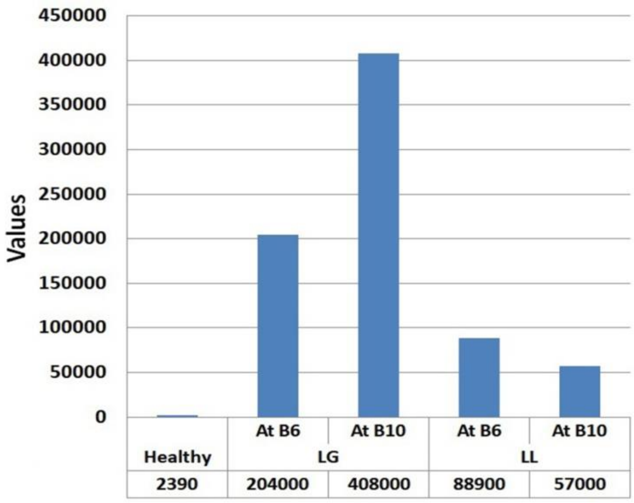

Fig. 4.11: FNM of P-V Cell bus at different conditions

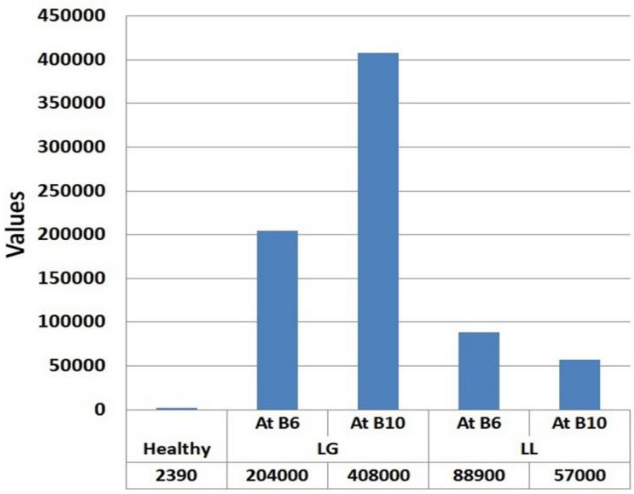

Fig. 4.12: DZ_1 of P-V Cell bus at different conditions

Table 4.4 presents the values of SPM, SNM, and DZ_2 for the outgoing currents of the PV Cell bus across a range of conditions.

Table 4.4 SPM, SNM, and DZ_2 Values of Outgoing Current from P-V Cell bus

Condition		Zone-1		
		SPM	SNM	DZ_2
Healthy		0	-3.6×10^3	3.6×10^3
LG	At B6	0.51×10^5	0	0.51×10^5
	At B10	0	-1.74×10^5	1.74×10^5
LL	At B6	0	-1.5×10^4	1.5×10^4
	At B10	2.19×10^5	0	2.19×10^5

Values SPM, SNM, and DZ_2 of P-V Cell bus are listed above in Table 4.4 for various conditions. These values are visually depicted as bar graphs in Figure 4.13, 4.14 and 4.15, providing a clear representation of their variations across the different scenarios.

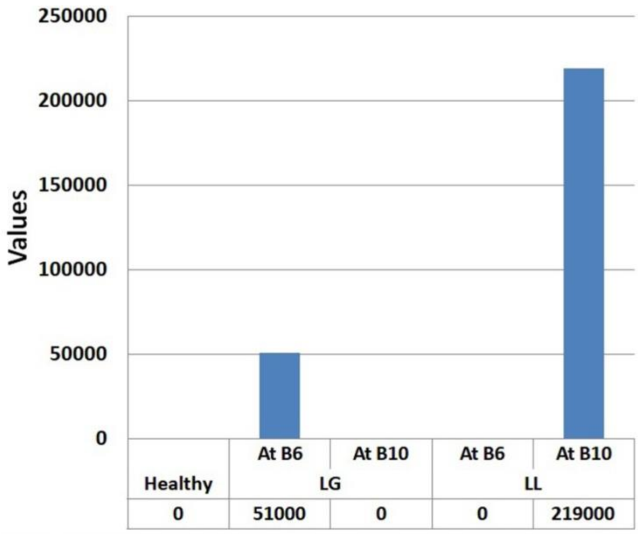

Fig. 4.13: SPM of P-V Cell bus at different conditions

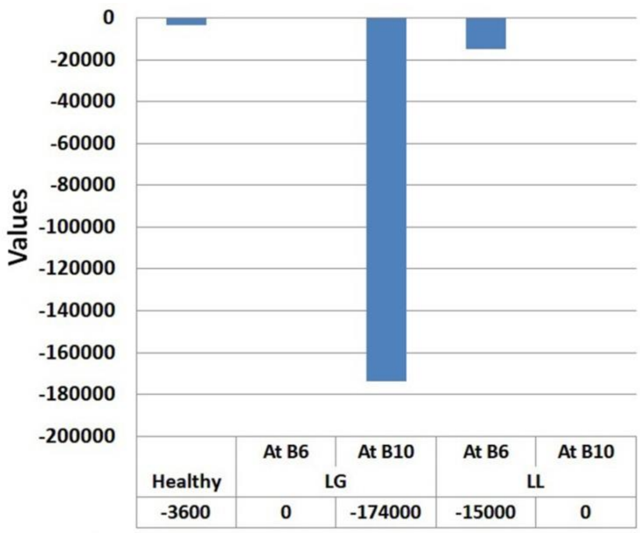

Fig. 4.14: SNM of P-V Cell bus at different conditions

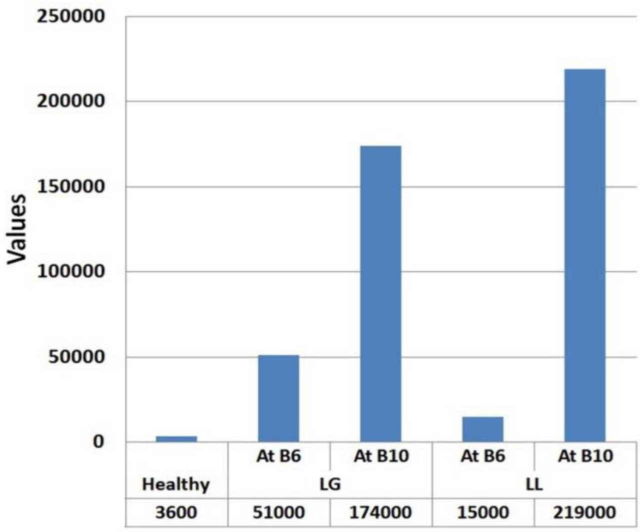

Fig. 4.15: DZ_2 of bulk generator bus at different conditions

With the help of figures provided above, the best parameter selection is done in the following section.

4.5 Selection of the Best Parameter

Fig. 4.6 indicates that in the kurtosis versus time plots for zone-1, only FPM was acquired. It is also noticed that the FPM values do not exhibit clear variations across different conditions. In contrast, Fig. 4.9 demonstrates that the variations in DZ_2 are significantly more pronounced. Hence, DZ_2 can be effectively employed to distinguish the fault type and recognize its location. Similarly, Fig. 4.18 reveals that DZ_2 exhibits clear variations for different conditions as well.

Table 4.5 Selection of Best Parameter

Observation made from	Parameters Considered	Best Parameter for identification of fault location and discrimination of fault
Bulk Generator Bus	FPP, FNP, DZ_1, SPP, SNP, DZ_2	DZ_2
PV Cell Bus	FPP, FNP, DZ_1, SPP, SNP, DZ_2	DZ_2

Based on the analysis, DZ_2 was determined to be the most effective parameter for identifying fault locations and distinguishing fault types, as indicated in Table 4.5. The evaluated parameters included FPM, FNM, DZ_1, SPM, SNM, and DZ_2.

4.6 Formation of Algorithm

Algorithm for detecting location of fault and identifying type of fault from bulk generator and P-V Cell bus is as follows:

- Capture outgoing current signal from the bus where observation is made and consider per unit value.
- Perform S – Transform.
- Determine skewness values of the S – Transform matrix.
- Determine DZ_2 and locate fault and identify fault type in both the cases of bulk generator and PV Cell bus.

The processing time of this algorithm is notably small, having execution duration of 0.02 seconds. Flowchart for detection of fault type and location by applying the above algorithm on outgoing current of bulk generator bus is given below:

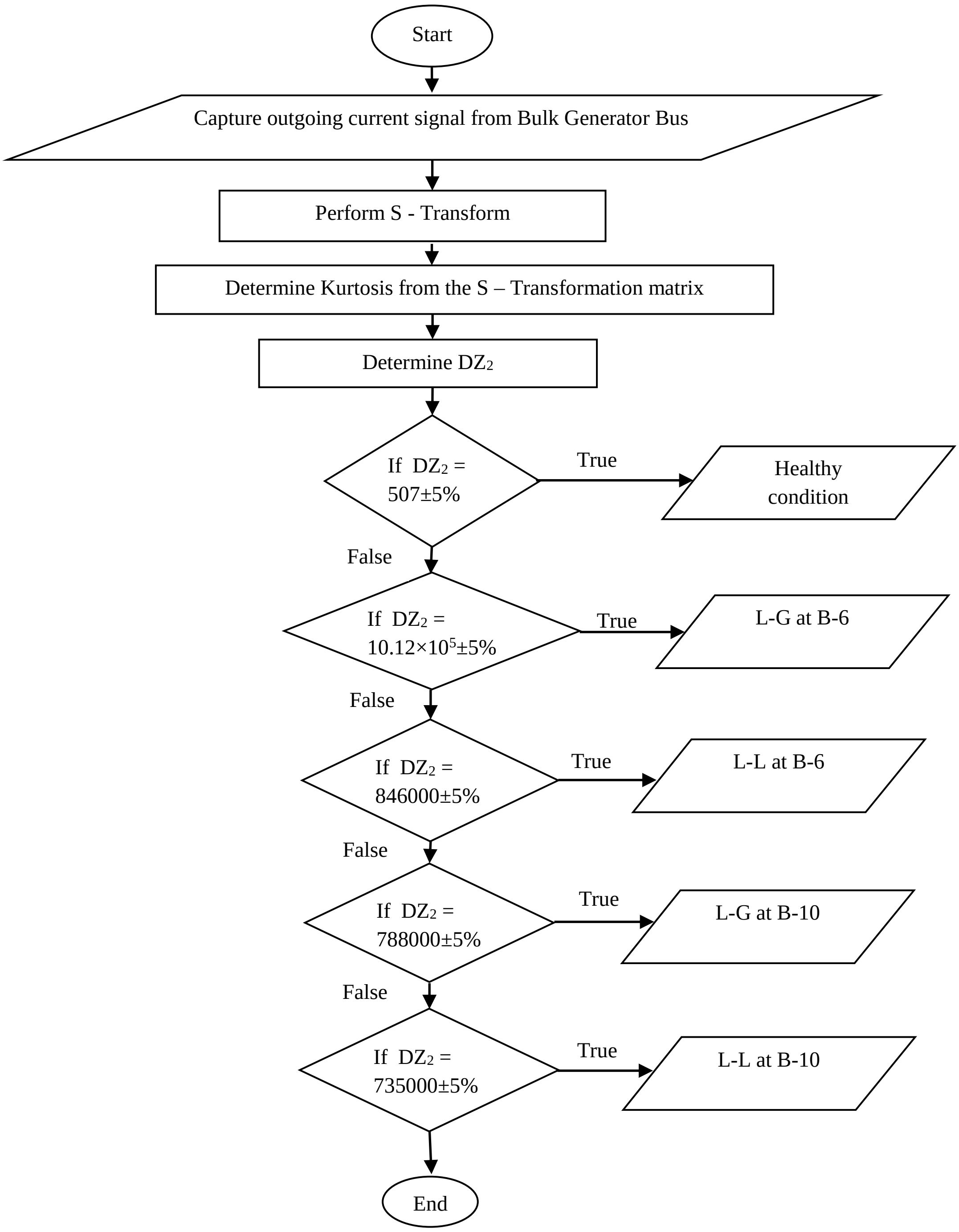

Flowchart for detection of fault type and location by applying the above algorithm on outgoing current of P-V Cell Bus is given below:

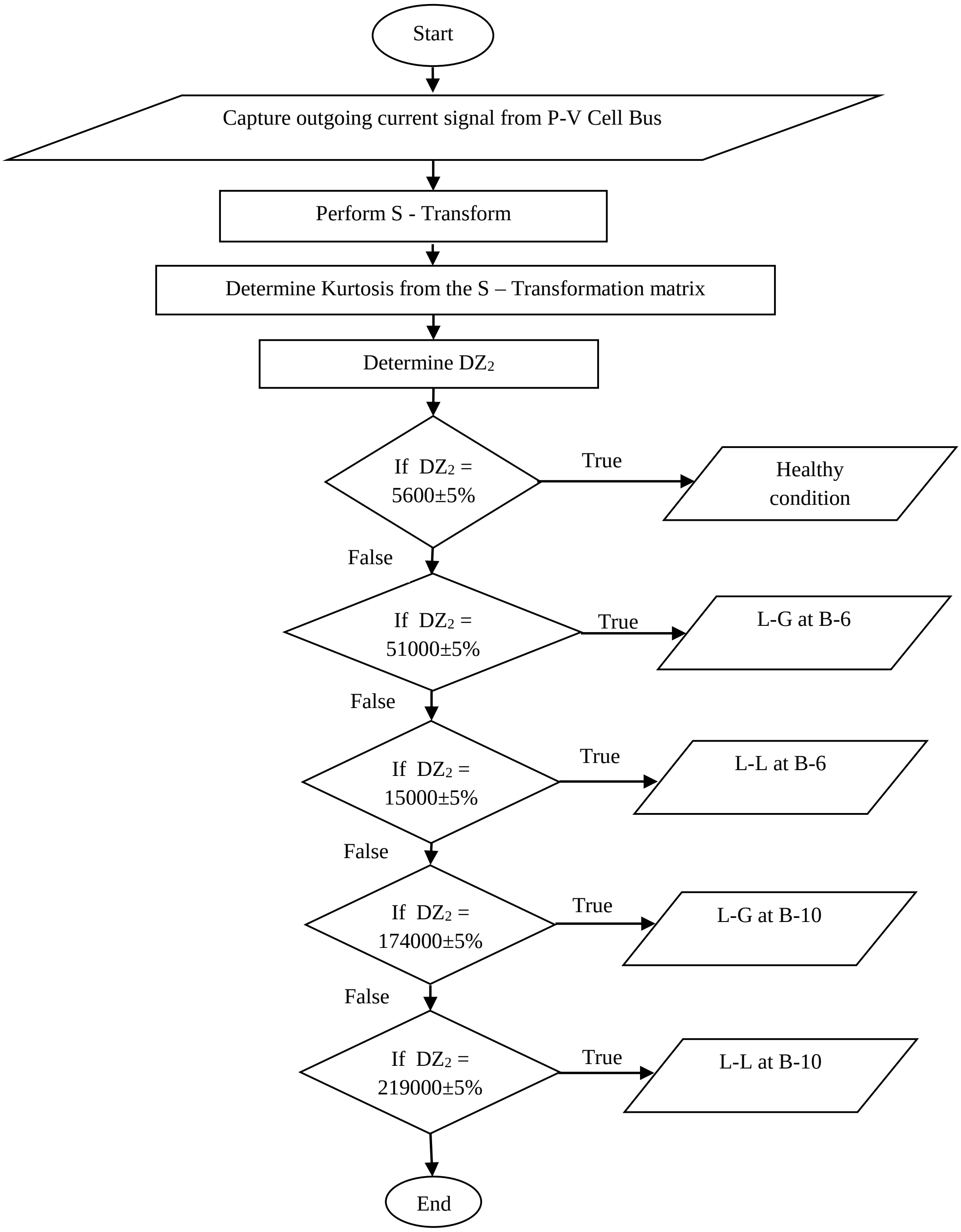

4.7 Case Studies and Validation

Validating the proposed algorithm in a real-world laboratory setting is not feasible. Therefore, to assess its performance, simulations of L-G and L-L faults were conducted within the IEEE standard 14-bus microgrid network. The simulations considered four distinct pre-fault scenarios: both load buses B-6 and B-10 active, only one of the load buses active, and both load buses inactive. In each scenario, an L-G fault was simulated on phase 'C,' and an L-L fault was simulated between phases

'C' and 'B' at buses B-6 and B-10. Current signals recorded from the bulk generator and P-V Cell buses were analyzed using S-Transformation to extract the parameters outlined in section 4.3. The algorithm was then applied to identify the fault type and its location. Results, as presented in Table 4.6, demonstrate that the algorithm accurately identified the fault type and location, matching the predefined conditions in all cases.

Table 4.6 Validation of the Algorithm

Known Facts			Observation as per proposed algorithm		
Pre-fault Condition	Fault Type	Fault Location	Observed From	DZ_2 Value	Inference
100% Furnace load (at B6) and 100% Non-Linear Load (at B10)	L-G	B-10	Bulk Generator Bus	7.86×10^5	L-G Fault has occurred at B10
			P-V Cell Bus	1.77×10^5	
100% Furnace load (at B6) and 100% Non-Linear Load (at B10)	L-L	B-6	Bulk Generator Bus	8.5×10^5	L-L Fault has occurred at B6
			P-V Cell Bus	1.48×10^4	
100% Furnace load (at B6) and Non-Linear Load (at B10) is Off	L-G	B-6	Bulk Generator Bus	10.19×10^5	L-G Fault has occurred at B-6
			PV Cell Bus	0.54×10^5	
100% Furnace load (at B6) and Non-Linear Load (at B10) is Off	L-L	B-10	Bulk Generator Bus	7.32×10^5	L-L Fault has occurred at B-10
			P-V Cell Bus	2.22×10^5	
Furnace load (at B6) is Off and Non-Linear Load (at B10) is 100%	L-G	B-10	Bulk Generator Bus	7.9×10^5	L-G Fault has occurred at B-10
			P-V Cell Bus	1.71×10^5	
Furnace load (at B6) is Off and Non-Linear Load (at B10) is 100%	L-G	B-6	Bulk Generator Bus	10.11×10^5	L-G Fault has occurred at B-6
			P-V Cell Bus	0.53×10^5	
Furnace load (at B6) is Off and Non-Linear Load (at B10) is 100%	L-L	B-10	Bulk Generator Bus	7.37×10^5	L-L Fault has occurred at B-10
			P-V Cell Bus	2.18×10^5	
Furnace load (at B6) is Off and Non-Linear Load (at B10) is 100%	L-L	B-6	Bulk Generator Bus	8.44×10^5	L-L Fault has occurred at B-6
			P-V Cell Bus	1.47×10^4	

4.8 Summary

The work presented above involves generating kurtosis vs. time plots by applying the S-Transformation to the outgoing currents of various generator buses under different conditions and computing the kurtosis of S-Transform matrices. The resulting plots consistently display two distinct regions, referred to as Zone-1 and Zone-2. Within these zones, up to four unique peaks may be observed: the first positive maximum, the first negative maximum, the second positive maximum, and the second negative maximum. Not all plots necessarily exhibit all four peaks. While the overall patterns of the plots are similar, the peak magnitudes differ across various scenarios. Consequently, six distinct parameters have been established based on these peaks. Analysis indicates that the DZ_2 parameter is the most effective for distinguishing fault types and recognizing fault locations. An algorithm has been developed based on these findings, and its effectiveness has been tested and confirmed.

For simplicity, this study focuses solely on Line-to-Ground (L-G) and Line-to-Line (L-L) faults, considering only two generator buses — Bulk Generator and P-V Cell bus—and two load buses—Furnace bus (B-6) and Non-linear load bus (B-10). However, the methodology can be expanded to include all fault types and additional generator and load buses within the network. Such an extension would enable the algorithm to accurately detect and locate any fault type across the entire network.

.

Publication:

S. Datta, A. Chattopadhyaya, S. Chattopadhayay & A. Das, "S-Transform Based Kurtosis Analysis for Detection of LG and LL Faults in 14 Bus Microgrid System," IETE Journal of Research, June 2020, DOI: 10.1080/03772063.2020.1779619

Chapter 5

Fault Assessment through S – Transform based Skewness Computation of Current Signature

The work presented here, shows a method for identifying fault locations and distinguishing fault types within a microgrid network. Stockwell Transform (S-Transform) based skewness analysis is performed and subsequently a unique algorithm is developed for this purpose.

5.1 Introduction

Detecting faults in microgrid networks with traditional methods is ineffective due to minimal current and voltage levels. This study explores fault location and type identification using the Stockwell Transform (S-Transform) to calculate the skewness of outgoing current signals from various generator buses. The analysis is conducted on an IEEE – Standard 14 bus microgrid network. Faults are evaluated at the electric furnace bus and nonlinear load bus. Current signals from two generator buses are analyzed and an algorithm is developed to determine fault location and type by examining these out-going currents, which is impervious to variations in fault-resistance. The algorithm is validated across various unknown scenarios, yielding satisfactory results. Simulations are carried out in MATLAB, modelling the IEEE – Standard 14 bus microgrid system. This work offers valuable insights for developing robust protection strategies for microgrid systems.

5.2 Details of Fault Simulation

IEEE Standard 14 Bus Microgrid System is shown in Fig. 3.1. To create a Line-to-Ground (L-G) fault on bus B-6 (furnace bus) and B-10 (non-linear load bus), phase 'C' and ground are utilized. Likewise, Line-to-Line (L-L) and Line-to-Line-to-Ground (L-L-G) faults involve phases 'B' and 'C' of the aforementioned load buses. A three-phase (L-L-L) fault is also considered at these specified load buses. During fault simulation on B-6 and B-10, all other buses remain in a healthy state. For simplicity in analysis, only two of the five load buses are taken into account. Current signals from phase 'C' of two specific generator buses – bulk generator bus and P-V Cell bus are monitored. The total simulation duration is set to 0.5 seconds, with faults occurring between 0.15 and 0.35 seconds. A high sampling frequency of 1000 Hz is employed to prevent aliasing. A compact data size is achieved by using a short simulation period.

5.3 Fault Classification using Skewness

Currents from phase 'C' of bulk generator bus and P-V Cell bus are evaluated under seven different scenarios - healthy, L-G, L-L, L-L-G, and L-L-L faults at buses B-6 and B-10, using the S-Transform resulting in formation of S-Transformation matrices. These matrices capture the current magnitudes across various frequencies at specific time instants. Skewness values were computed from the S-Transformation matrices for each scenario. Subsequently, plots of skewness versus time were created. Occurrence of faults causes the harmonic components of the current signals to shift, leading to alterations in the S-Transformation matrix elements and their corresponding skewness values.

5.3.1 Healthy Condition

The S-Transform was applied to currents exiting the bulk generator and P-V Cell buses under healthy conditions, with the resulting skewness values from the S-Transform matrices plotted against time (in seconds) on the x-axis and skewness on the y-axis, as shown in Figures 5.1(a) and 5.1(b).

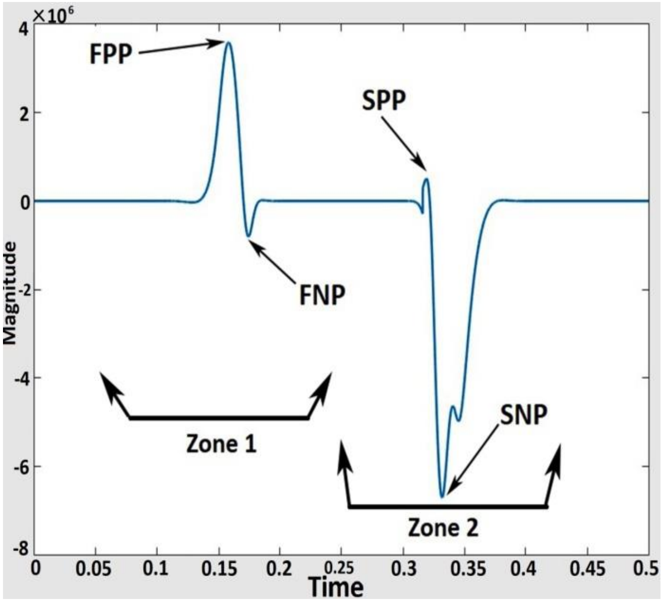

5.1(a)

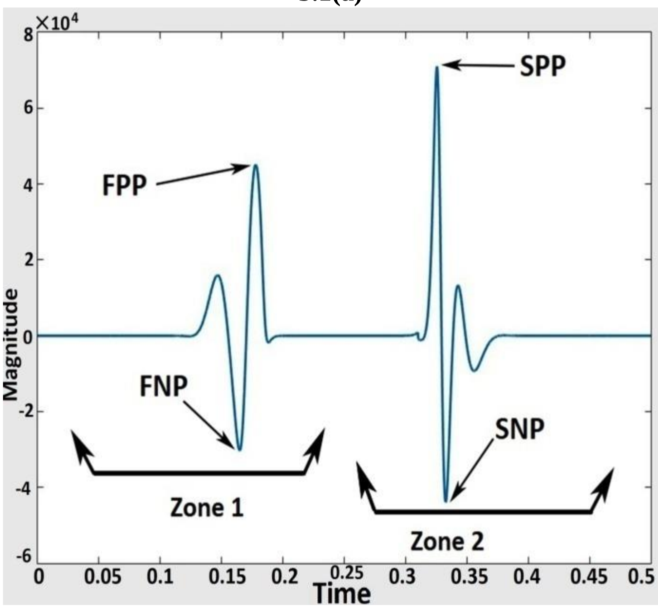

5.1(b)

Fig. 5.1: Skewness vs. Time (in seconds) plot of S – Transformation results of currents flowing out of **(a)** bulk generator, **(b)** P-V Cell bus in healthy state

Fig. 5.1(a) and 5.1(b) display four distinct peaks labelled as First Positive Peak (FPP), First Negative Peak (FNP), Second Positive Peak (SPP), and Second Negative Peak (SNP). These peaks are highlighted within the aforementioned figures. Furthermore, the peaks appear across two distinct areas, referred to as zone-1 and zone-2.

5.3.2 Establishment of Novel Parameters for Comparison

Based on the features of the graphs shown in Fig. 5.1(a) and 5.1(b), six different parameters are formed.

First Positive Peak (FPP):

The magnitude of the first positive peak of the graph is termed as the First Positive Peak (FPP).

First Negative Peak (FNP):

The magnitude of the first negative peak of the graph is defined as the First Negative Peak (FNP).

Difference of First Zone Peaks (DZ_1)

It is the difference between FPP and FNP i.e.

$$\mathrm{DZ}_1 = (\mathrm{FPP} - \mathrm{FNP})$$

Second Positive Peak (SPP)

The magnitude of the second positive peak of the graph is termed as the Second Positive Peak (SPP).

Second Negative Peak (SNP)

The magnitude of the second negative peak of the graph is defined as the Second Negative Peak (SNP).

Difference of Second Zone Peaks (DZ_2)

It is the difference between SPP and SNP i.e.

$$\mathrm{DZ}_2 = (\mathrm{SPP} - \mathrm{SNP})$$

The parameters FPP, FNP and DZ_1 are associated with Zone-1, while SPP, SNP and DZ_2 are linked to Zone-2. If any peak is missing in a plot, the corresponding parameter is assigned a value of zero. Using these parameters, it is possible to distinguish a healthy state from various fault conditions. The method for differentiating between these conditions is thoroughly explained in the subsequent sections.

5.3.3 Fault Conditions

Initially, the load buses B-6 and B-10 are selected for fault simulation. The currents flowing out from the B-Gen and P-V Cell buses under different conditions are subjected to S-Transformation, and plots of skewness against time for the resulting S-Transform matrices are produced.

Observation from Bulk Generator bus

Fig. 5.3 and 5.4 display graphs of skewness vs. time, derived from the S-Transformation matrices of currents exiting the B-Gen bus during an L-G fault at buses B-6 and B-10, respectively.

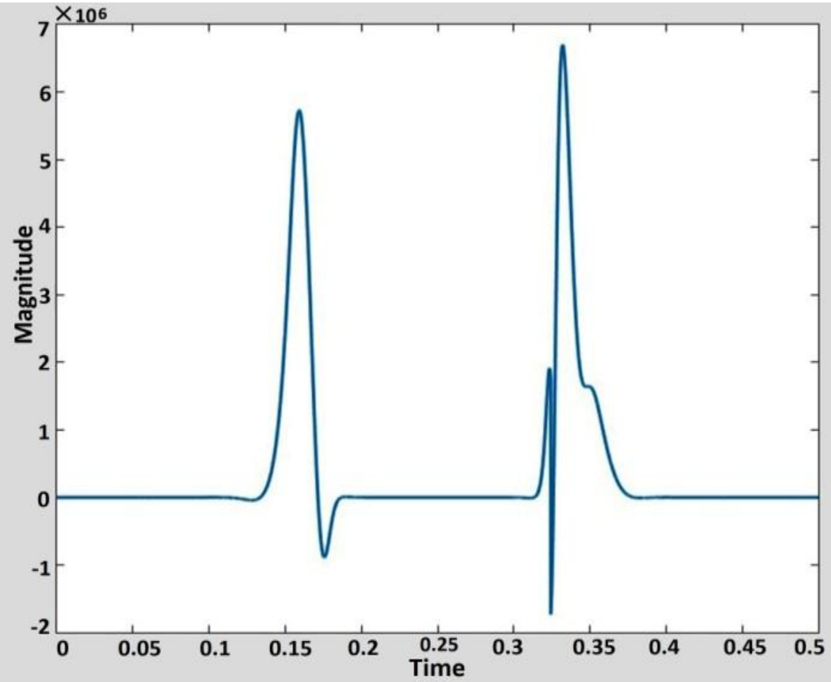

Fig. 5.2: Skewness vs. Time (in seconds) graphs of S – Transformation results of outbound currents from B-Gen bus for L-G at B-6

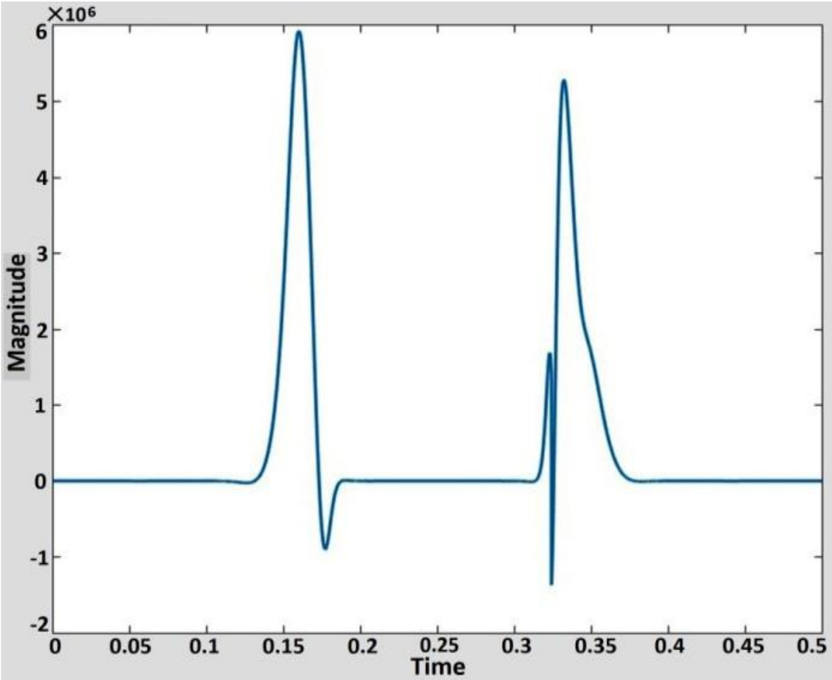

Fig. 5.3: Skewness vs. Time (in seconds) graphs of S – Transformation results of outbound currents from B-Gen bus for L-G at B-10

Fig. 5.5 and 5.6 illustrate skewness vs. time plots for the S-Transformation results of currents outbound from the B-Gen bus during an L-L fault at buses B-6 and B-10, respectively.

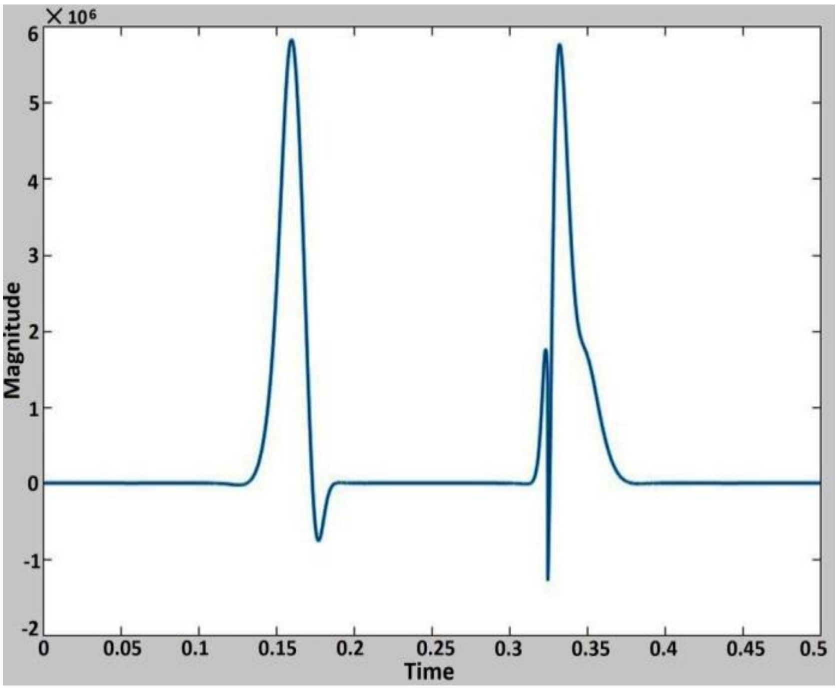

Fig. 5.4: Skewness vs. Time (in seconds) graphs of S – Transformation results of outbound currents from B-Gen bus for L-L at B-6

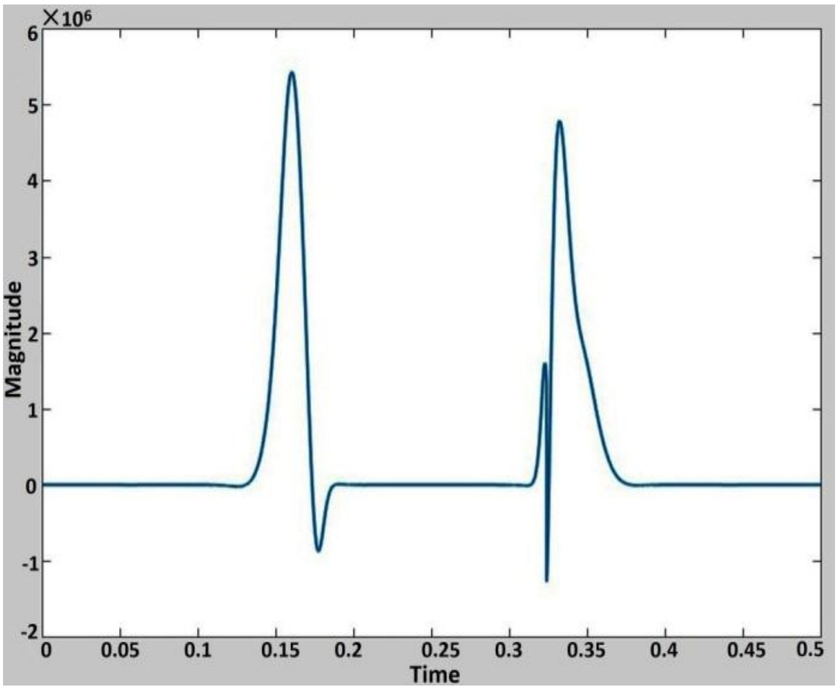

Fig. 5.5: Skewness vs. Time (in seconds) graphs of S – Transformation results of outbound currents from B-Gen bus for L-L at B-10

Fig. 5.6 and 5.7 illustrate the skewness vs. time plot derived from the application of S-Transformation to currents exiting the B-Gen bus during an L-L-G fault at buses B-6 and B-10, respectively. These plots provide a visual representation of the skewness of S-Transformation matrices under specific fault conditions.

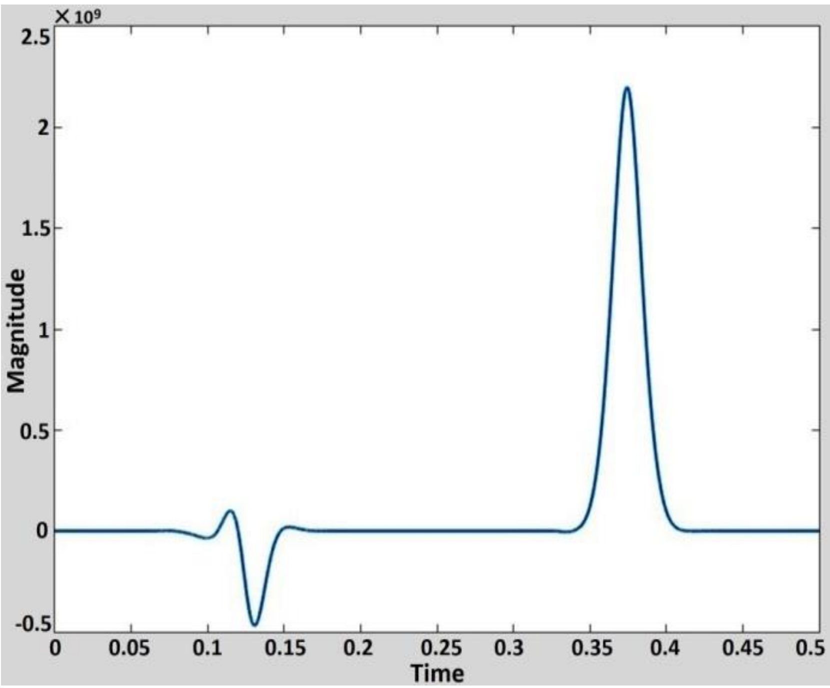

Fig. 5.6: Skewness vs. Time (in seconds) graphs of S – Transformation results of outbound currents from B-Gen bus for L-L-G at B-6

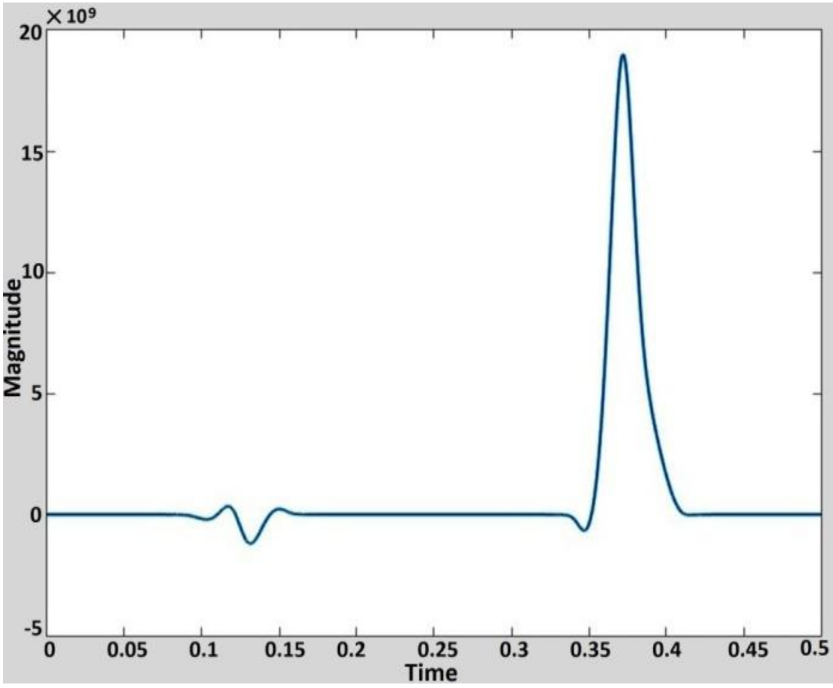

Fig. 5.7: Skewness vs. Time (in seconds) graphs of S – Transformation results of outbound currents from B-Gen bus for L-L-G at B-10

Similarly, Fig. 5.8 and 5.9 depict the skewness vs. time graphs for the S-Transformation results of currents flowing out from the B-Gen bus during an L-L-L fault at buses B-6 and B-10, respectively.

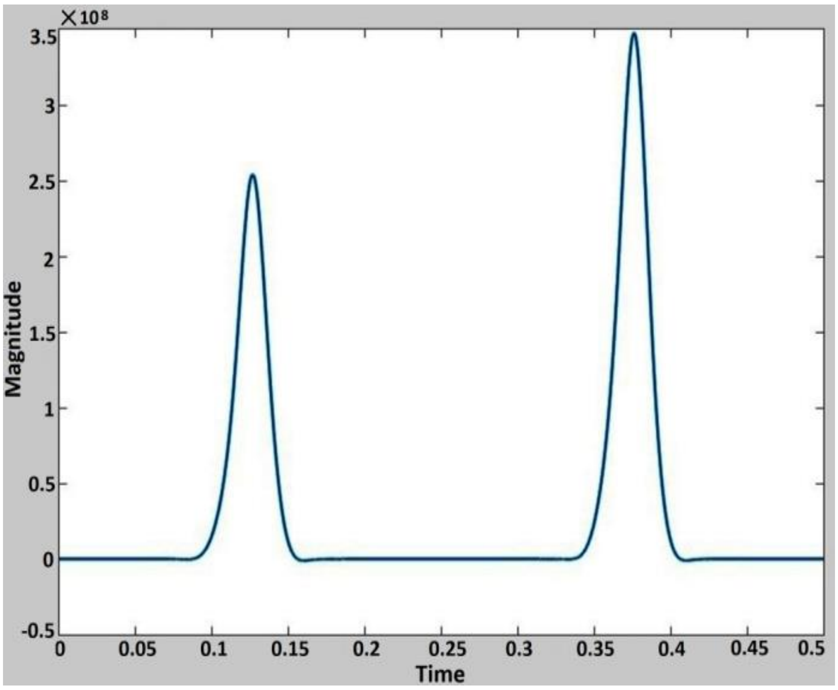

Fig. 5.8: Skewness vs. Time (in seconds) graphs of S – Transformation results of outbound currents from B-Gen bus for L-L-L at B-6

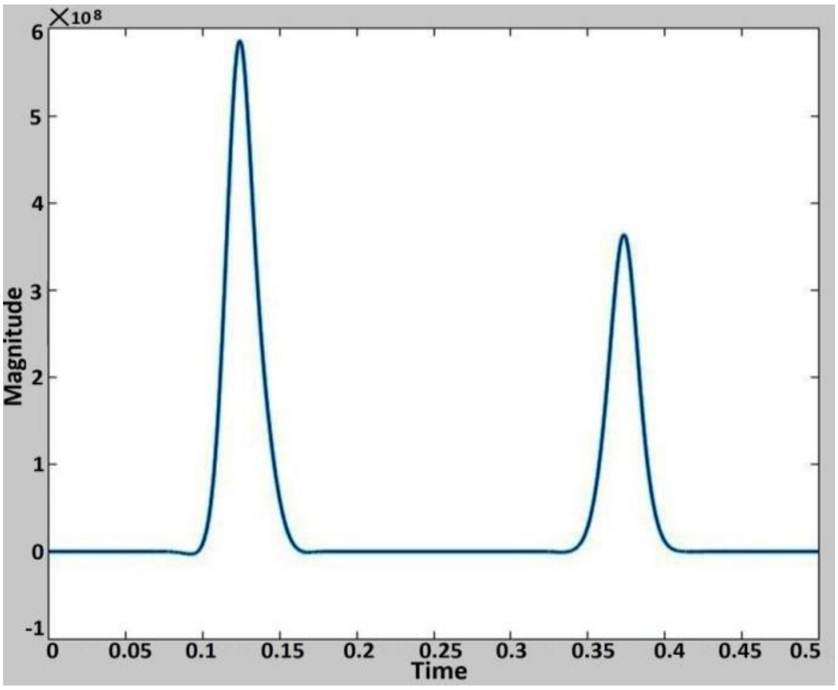

Fig. 5.9: Skewness vs. Time (in seconds) graphs of S – Transformation results of outbound currents from B-Gen bus for L-L-L at B-10

Observation from P-V Cell bus

Fig.5.10 and 5.11 showcase the skewness over time plots, derived from the S-Transformation of currents flowing out from the P-V Cell bus during an L-G fault at buses B-6 and B-10, respectively. Similarly, Fig. 5.12 and 5.13 present the skewness plots for the S-Transformation results of outbound currents from the P-V Cell bus when an L-L fault occurs at buses B-6 and B-10, respectively. These diagrams provide a detailed visualization of the current behaviour under specific fault conditions.

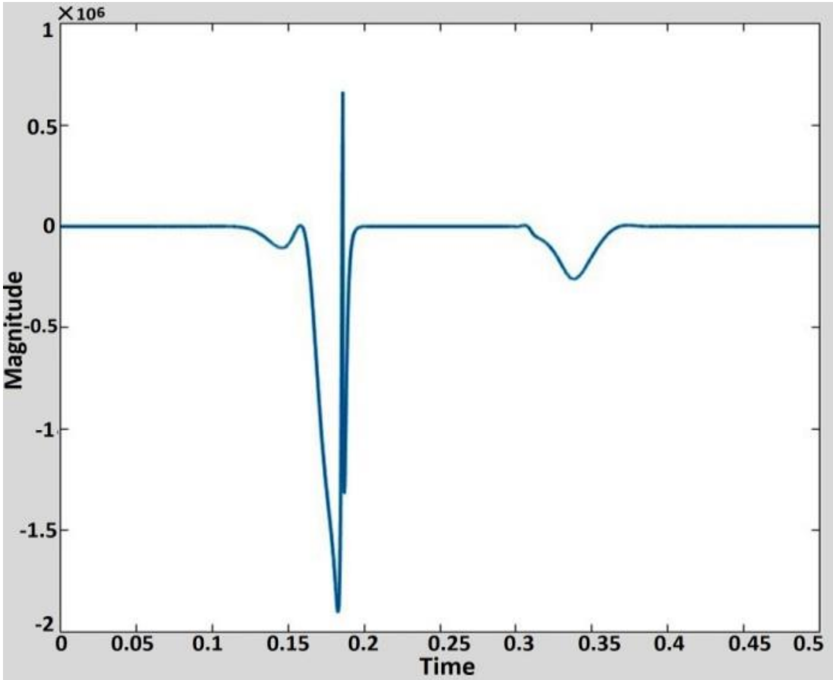

Fig. 5.10: Skewness vs. Time (in seconds) graphs of S – Transformation results of outbound currents from P-V Cell bus for L-G at B-6

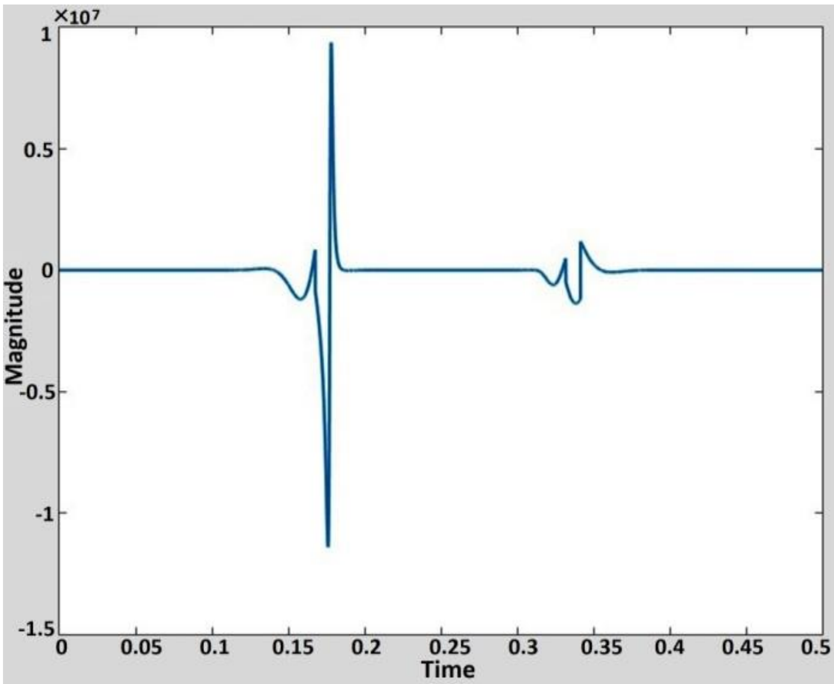

Fig. 5.11: Skewness vs. Time (in seconds) graphs of S – Transformation results of outbound currents from P-V Cell bus for L-G at B-10

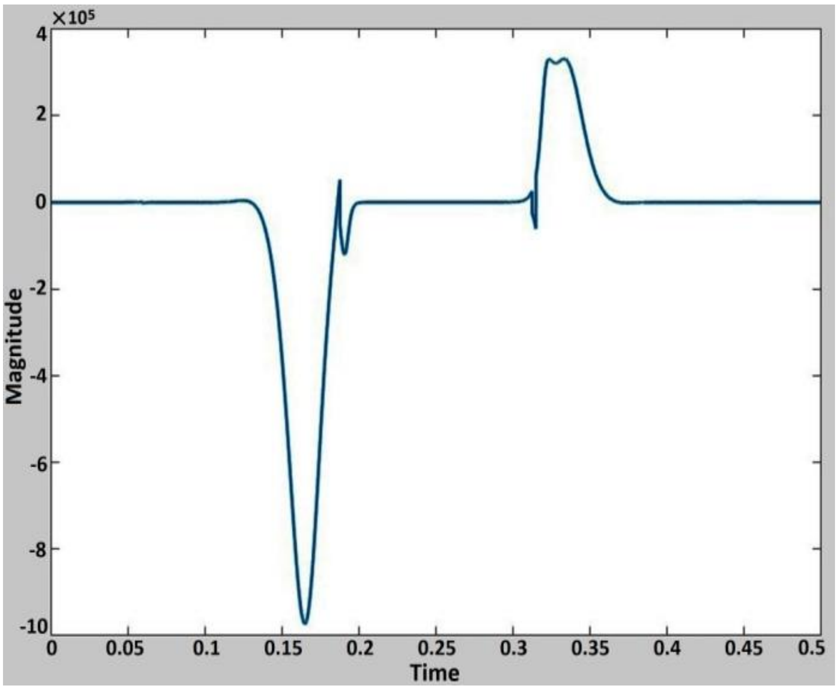

Fig. 5.12: Skewness vs. Time (in seconds) graphs of S – Transformation results of outbound currents from P-V Cell bus for L-L at B-6

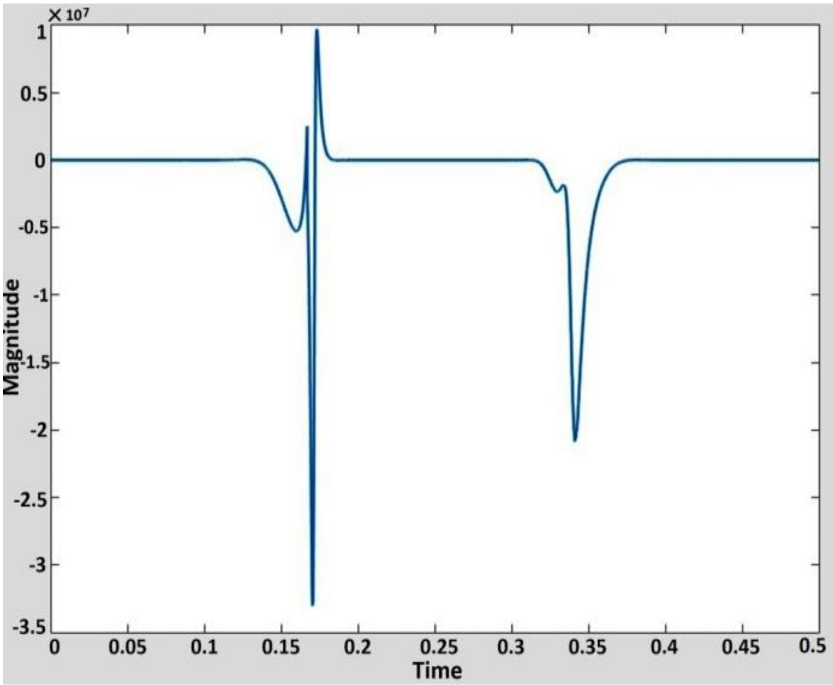

Fig. 5.13: Skewness vs. Time (in seconds) graphs of S – Transformation results of outbound currents from P-V Cell bus for L-L at B-10

Fig. 5.14 and 5.15 illustrate the skewness over time, calculated from the S-Transformation of currents exiting the P-V Cell bus during an L-L-G fault at buses B-6 and B-10, respectively. Likewise, Figures 5.16 and 5.17 depict the skewness plots derived from the S-Transformation of outbound currents from the P-V Cell bus when an L-L-L fault occurs at buses B-6 and B-10, respectively.

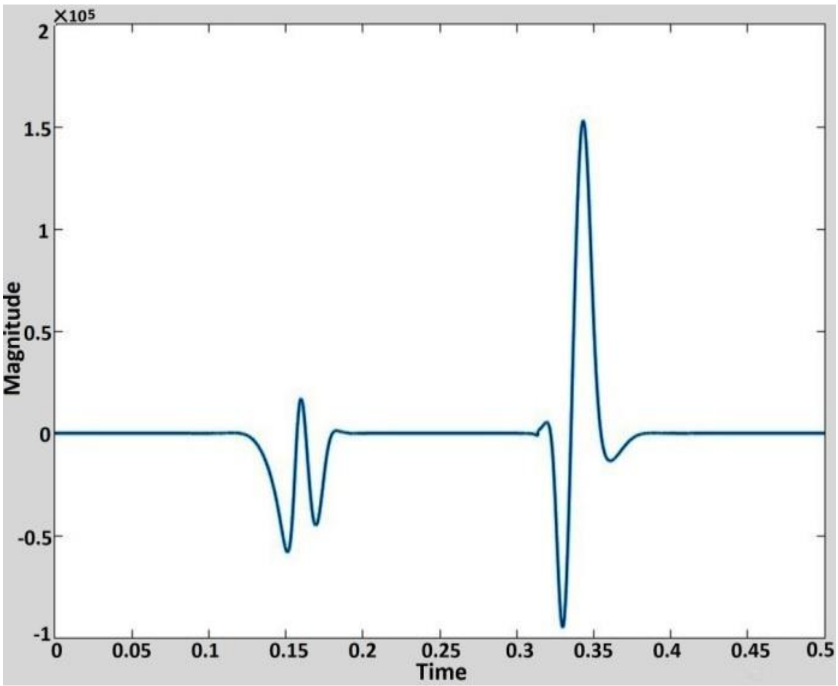

Fig. 5.14: Skewness vs. Time (in seconds) graphs of S – Transformation results of outbound currents from P-V Cell bus for L-L-G at B-6

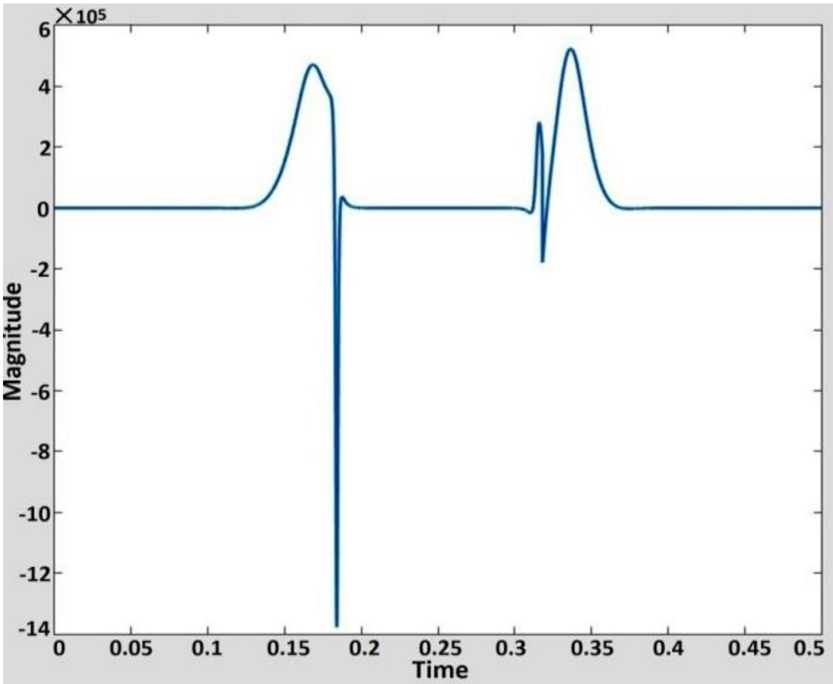

Fig. 5.15: Skewness vs. Time (in seconds) graphs of S – Transformation results of outbound currents from P-V Cell bus for L-L-G at B-10

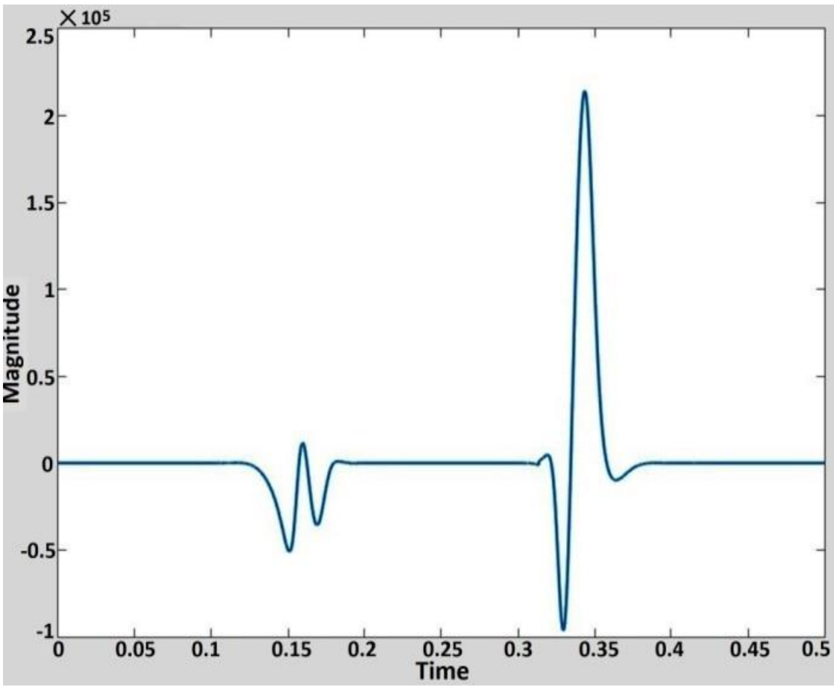

Fig. 5.16: Skewness vs. Time (in seconds) graphs of S – Transformation results of outbound currents from P-V Cell bus for L-L-L at B-6

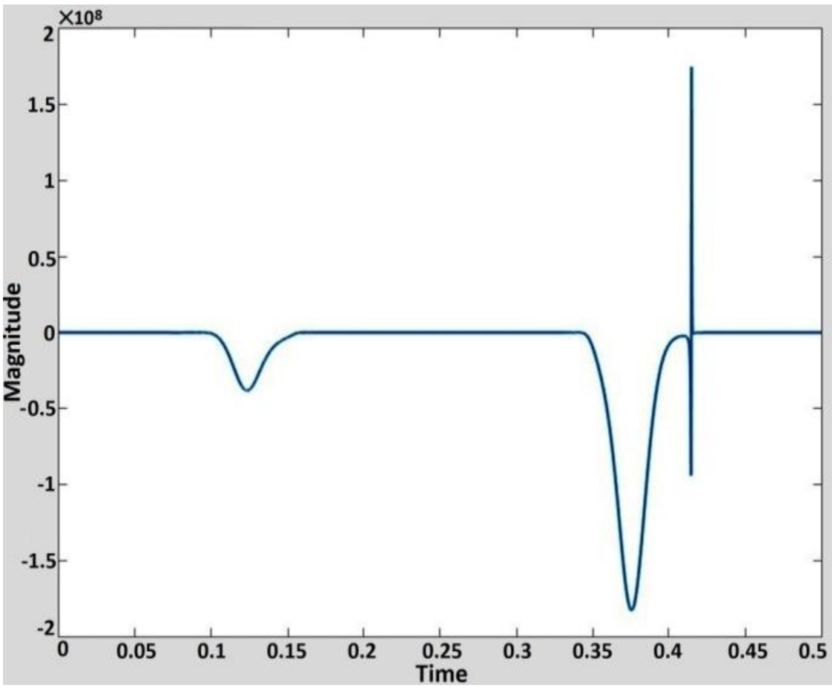

Fig. 5.17: Skewness vs. Time (in seconds) graphs of S – Transformation results of outbound currents from P-V Cell bus for L-L-L at B-10

5.4 Discrimination between Healthy and Faulty conditions

Table 5.1 shows, FPP, FNP and DZ_1 values of currents flowing out from B- Gen bus in various conditions. Whereas, Table 5.2 shows, SPP, SNP, DZ_2 values of currents flowing out from B- Gen bus in various conditions.

Table 5.1 FPP, FNP, and DZ_1 Values of B-Gen Bus Outbound Currents

Condition		Zone-1		
		FPP	FNP	DZ_1
Healthy		3.58×10^{6}	-8×10^{5}	4.38×10^{6}
L-G	At B-6	5.66×10^{6}	-9.9×10^{5}	6.66×10^{6}
	At B-10	5.99×10^{6}	-9.2×10^{5}	6.91×10^{6}
L-L	At B-6	5.86×10^{6}	-9.8×10^{5}	6.84×10^{6}
	At B-10	5.78×10^{6}	-9.77×10^{5}	6.76×10^{6}
L-L-G	At B-6	0.12×10^{9}	-0.48×10^{9}	0.60×10^{9}
	At B-10	0.04×10^{9}	-0.11×10^{9}	0.15×10^{9}
L-L-L	At B-6	2.53×10^{8}	0	2.53×10^{8}
	At B-10	5.98×10^{8}	0	5.98×10^{8}

Table 5.2 SPP, SNP, and DZ_2 Values of B-Gen Bus Outbound Currents

Condition		Zone-2		
		SPP	SNP	DZ_2
Healthy		4×10^{5}	-6.7×10^{6}	7.1×10^{6}
L-G	At B-6	6.65×10^{6}	-1.9×10^{6}	8.55×10^{6}
	At B-10	5.29×10^{6}	-1.34×10^{6}	6.63×10^{6}
L-L	At B-6	5.97×10^{6}	-1.38×10^{6}	7.35×10^{6}
	At B-10	4.9×10^{6}	-1.35×10^{6}	6.25×10^{6}
L-L-G	At B-6	2.23×10^{9}	0	2.23×10^{9}
	At B-10	19.2×10^{9}	-0.02×10^{9}	19.22×10^{9}
L-L-L	At B-6	3.44×10^{8}	0	3.44×10^{8}
	At B-10	3.9×10^{8}	0	3.9×10^{8}

Table 5.3 shows, FPP, FNP and DZ_1 values of currents flowing out from P-V Cell bus in various conditions.

Table 5.3 FPP, FNP, and DZ_1 Values of P-V Cell Bus Outbound Currents

Condition		Zone-1		
		FPP	FNP	DZ_1
Healthy		4.50×10^{6}	-3.02×10^{6}	7.52×10^{6}
L-G	At B-6	6.80×10^{5}	-1.89×10^{6}	2.57×10^{6}
	At B-10	9.30×10^{7}	-1.24×10^{7}	10.54×10^{7}
L-L	At B-6	6.50×10^{4}	-9.96×10^{5}	1.06×10^{6}
	At B-10	9.80×10^{6}	-3.40×10^{7}	43.8×10^{6}
L-L-G	At B-6	0.21×10^{5}	-0.52×10^{5}	0.73×10^{5}
	At B-10	4.88×10^{5}	-13.95×10^{5}	18.83×10^{5}
L-L-L	At B-6	0.1×10^{5}	-0.51×10^{5}	0.52×10^{5}
	At B-10	0	-0.48×10^{8}	-0.48×10^{8}

Whereas, Table 5.4 shows, SPP, SNP, DZ_2 values of currents flowing out from P-V Cell bus in various conditions.

Table 5.4 SPP, SNP, and DZ_2 Values of P-V Cell Bus Outbound Currents

Condition		Zone-2		
		SPP	SNP	DZ_2
Healthy		7.09×10^{6}	-4.30×10^{6}	11.4×10^{6}
L-G	At B-6	0	-3.4×10^{5}	3.4×10^{5}
	At B-10	1.80×10^{6}	-1.20×10^{6}	3×10^{6}
L-L	At B-6	3.64×10^{5}	-3.30×10^{4}	3.97×10^{5}
	At B-10	0	-2.22×10^{7}	2.22×10^{7}
L-L-G	At B-6	1.51×10^{5}	-0.93×10^{5}	2.44×10^{5}
	At B-10	5.48×10^{5}	-1.97×10^{5}	7.45×10^{5}
L-L-L	At B-6	2.13×10^{5}	-0.98×10^{5}	3.11×10^{5}
	At B-10	1.74×10^{8}	-1.55×10^{8}	3.29×10^{8}

The information provided above has been used to identify the most well suited parameter. The methodology for this selection is detailed in the subsequent section.

5.5 Best Parameter Selection

The data in Table 5.1 suggests minimal observable differences in FPP, FNP, and DZ_1, indicating they are not distinctly varied. Conversely, Table 5.2 demonstrates clear and identifiable differences in SPP values. This parameter can therefore be utilized to differentiate fault locations and fault types from the B-Gen bus.

Table 5.3 reveals that Zone-1 parameters—FPP, FNP, and DZ_1 exhibit no notable changes across different fault conditions. In contrast, Table 5.4 shows that DZ_2 values display significant variations under various conditions.

Table 5.5 Selection of the Best Parameter

Observation made from	Parameters Considered	The Best Parameter for detection of ‘fault-location’ and ‘fault-type’
B-Gen Bus	F.P.P., F.N.P., DZ_1, S.P.P., S.N.P., DZ_2	S.P.P.
P-V Cell Bus	F.P.P., F.N.P., DZ_1, S.P.P., S.N.P., DZ_2	DZ_2

Table 5.5 indicates that two parameters are optimally suited for identifying the fault location and determining the fault type. The parameters evaluated include FPP, FNP, DZ_1, SPP, SNP, and DZ_2. For observations from the B-Gen bus, SPP is identified as the most effective parameter for detecting fault locations and distinguishing fault types. However, at the P-V Cell bus, DZ_2 proves to be the most reliable parameter, as it effectively identifies fault locations and differentiates between fault types. A tolerance of ±2% is applied to both SPP and DZ_2 values. The total execution time for the process is 0.015 seconds.

5.6 Formation of Algorithm

Following the steps given below, fault-location and fault-type can be detected from B-Gen as well as P-V Cell bus:

- Record the outbound current waveform from the observation bus (B-Gen or P-V Cell) and convert to per unit values.
- Carry out S – Transform.
- Calculate skewness of the S – Transformation matrix.
- If observation is from B-Gen bus, determine S.P.P. to get fault-location and fault-type.
- If observation is from P-V Cell bus, find out DZ_2 to get fault-location and fault-type.

Discrimination between faulty and healthy states, recognition of the fault- type (L-G, L-L, L-L-G and L-L-L) and detection of fault- location (B-6 or B-10) can be done with the help of aforementioned algorithm.

5.7 Case Studies and Validation

Since real-time validation in a laboratory setting is not feasible, the proposed algorithm was validated through fault simulations on the IEEE-standard 14 bus microgrid system. Faults including L-G, L-L, L-L-G, and L-L-L were simulated on buses B-6 and B-10 under various pre-fault conditions. Measurements were taken from both the B-Gen and P-V Cell buses. Outbound currents from these buses were processed using S-Transformation, and relevant parameters, as outlined in Table 5.5, were computed. The algorithm successfully identified both the fault location and fault type. Table 5.6 presented below, summarizes these findings, confirming that the fault locations and types detected by the proposed method align with the known conditions.

The uncertainties associated with distributed energy resources (D.E.R.), such as P-V cells, batteries, and diesel generators, were accounted for, as variations in their generation levels impact the short-circuit level of the network. The outputs of these D.E.R.s were tested at three levels: 100%, 80%, and 50%. Across all tested conditions, individual current harmonic components exhibited variations in magnitude. However, the skewness values derived from the S-Transformation matrices remained largely unchanged. Consequently, the proposed algorithm demonstrated robust performance in accurately determining fault locations and types, even with varying D.E.R. outputs.

Table 5.6 Selection of the Best Parameter

Known Facts			Observations according to the algorithm		
Pre-fault Condition	Fault Type	Fault Location	Observation Bus	Observation	Inference
100% Non-Linear Load (B-10) and 100% Furnace load (B-6)	L-G	B-10	B-Gen Bus P-V Cell Bus	$SPP = 5.26\times10^6$ $DZ_2 = 3.03\times10^6$	L-G at B-10
100% Non-Linear Load (B-10) and 100% Furnace load (B-6)	L-L	B-6	B-Gen Bus P-V Cell Bus	$SPP = 5.91\times10^6$ $DZ_2 = 3.93\times10^5$	L-L at B-6
Non-Linear Load (B-10) is Off and 100% Furnace load (B-6)	L-L-G	B-10	B-Gen Bus P-V Cell Bus	$SPP = 2.23\times10^9$ $DZ_2 = 2.45\times10^5$	L-L-G at B-10
Non-Linear Load (B-10) is Off and 100% Furnace load (B-6)	L-L-L	B-10	B-Gen Bus P-V Cell Bus	$SPP = 3.9\times10^8$ $DZ_2 = 3.3\times10^8$	L-L-L at B-10
100% Non-Linear Load (B-10) and Furnace load (B-6) is Off	L-G	B-10	B-Gen Bus P-V Cell Bus	$SPP = 5.25\times10^6$ $DZ_2 = 2.98\times10^6$	L-G at B-10
100% Non-Linear Load (B-10) and Furnace load (B-6) is Off	L-G	B-6	B-Gen Bus P-V Cell Bus	$SPP = 6.58\times10^6$ $DZ_2 = 3.44\times10^5$	L-G at B-6
100% Non-Linear Load (B-10) and 50% Furnace load (B-6)	L-L-G	B-10	B-Gen Bus P-V Cell Bus	$SPP = 19.2\times10^9$ $DZ_2 = 7.44\times10^5$	L-L-G at B-10
50% Non-Linear Load (B-10) and 100% Furnace load (B-6)	L-L-L	B-6	B-Gen Bus P-V Cell Bus	$SPP = 3.43\times10^8$ $DZ_2 = 3.11\times10^5$	L-L-L at B-6

The aforementioned algorithm is also tested by using it in 'IEC 61850-7-420' microgrid. In that network faults have been made to occur at load buses and outgoing currents from the bulk generator bus and also Photovoltaic (P-V Cell) bus are analysed with the method proposed here and the algorithm is applied. Alike 'IEEE standard 14 bus network' in this microgrid network also the results obtained through the algorithm proved to be very much satisfactory.

5.8 Summary

In this study, the skewness of outbound currents from the generator bus in the IEEE standard14 bus microgrid system was computed using S-Transformation, and corresponding skewness versus time graphs were generated. These graphs consistently displayed two distinct regions, Zone-1 and Zone-2, each characterized by two prominent peaks labelled as FPP, FNP, SPP and SNP. Additionally, two further parameters, DZ_1 and DZ_2, were defined based on these peaks. Analysis revealed that SPP is the most effective parameter for the bulk generator bus, while DZ_2 is optimal for the P-V Cell bus. Based on these findings, an algorithm was proposed and validated.

The algorithm utilizes skewness values derived from S-Transformation matrices, which capture the magnitude of currents across various frequencies at different time instants. Fault occurrences alter the harmonic content of the outbound currents from generator buses, leading to corresponding changes in the S-Transformation matrix and its skewness values. The proposed method offers several key advantages:

- It does not require knowledge of line parameters or wave velocity.
- Compared to prior S-Transformation-based techniques, it is significantly faster, requiring fewer parameters to identify fault locations and types, with a computational time of 0.015 seconds.
- The method is unaffected by fault resistance, as it relies on the statistical analysis of harmonic content in generator bus outbound currents, which is independent of resistive elements in the network.
- It is particularly effective for earth faults, as these are not influenced by arcing resistance, making it highly suitable for detecting earth faults in short-length lines commonly found in microgrid environments.

Here, the observations are made only from the B-Gen and P-V Cell bus, and the faults are created on furnace bus (B-6) and non-linear load bus (B-10). However, this work can be further developed to consider the observation from the other generator buses and with suitable modifications of the algorithm it can be applied to successfully identify fault-type and its location from any generator bus of the microgrid networks.

Publication:

S. Datta, A. Chattopadhyaya, S. Chattopadhayay & A. Das, "S-Transform Based Skewness Computation of Current Signature for Fault Assessment in IEEE Standard 14 Bus Microgrid System at Remote Terminals," IE Series (B). [Communicated]

Chapter 6

ANN based Adaptive Fog Computing using Wavelet based Statistical Scanning for Supervision of Remote End Fault in Internet of Microgrid Network

This chapter presents an artificial neural network-based fog computing approach for remote fault supervision in an IEEE Standard 14 bus microgrid, using Discrete Wavelet Transform (DWT) for statistical analysis of currents to develop a robust rule-based system that effectively detects Line-to-Ground (L-G) and Line-to-Line (L-L) faults at load buses, with reliable performance across varying fault resistances and reduced cloud storage needs.

6.1 Introduction

Work presented here explores a fog computing approach utilizing artificial neural networks for remote fault supervision in microgrid systems. The research introduces an adaptive fault monitoring system based on Artificial Neural Networks, designed for L-G and L-L faults within an IEEE Standard 14 bus microgrid network. Statistical analysis of outgoing currents from various generator buses is conducted using DWT under both healthy and fault conditions. Faults are made to happen at load buses, and a rule-based system is developed to identify fault type as well as fault locations. This rule set remains robust despite changes in fault resistance, making it highly effective for ground fault detection. The system has been tested on various unknown scenarios, yielding reliable outcomes. Incorporating a fog computing layer enables rapid processing and reduces the need for extensive cloud storage.

6.2 Fault Simulation

IEEE Standard 14 bus microgrid network is shown in Fig. 3.1. To simulate faults, a L-G fault is induced between phase ‘C’ and ground and a L-L fault is triggered between phases ‘B’ and ‘C’ on load buses B-6 (furnace bus) and B-10 (non-linear load) individually; while keeping other load buses operational. Only two buses are selected for simplicity. Phase ‘C currents from all the generator buses are monitored over a 0.8 second of simulation duration, with faults occurring between 0.2 and 0.4 seconds, using a 2000 Hz sampling frequency to prevent aliasing. Duration of fault simulation is kept small to minimize data size. Fifteen cycles of generator bus currents are analyzed, capturing the shift of the waveforms from steady to transient state during faults and back to steady state post-fault, with a 0.5 second. DWT is applied because of the non-stationary nature of current waveforms under faulty conditions. Current signals are decomposed into nine levels of approximate and detail coefficients using low-pass and high-pass filters, targeting the first twenty harmonics (1–1000 Hz). Each level is down-sampled to extract low-frequency (approximate) and high-frequency (detail) components, from which RMS, skewness, and kurtosis are calculated, denoted as RMS_A, S_A, K_A for approximate and

RMS_D, S_D, K_D for detail coefficients. Daubechies-4 (DB-4) is chosen as the optimal mother wavelet after testing alternatives like DB-3 and DB-10. In both healthy and faulty states, currents flowing out from the generator buses are captured via the Data Concentrator Unit (DCU) shown in Fig. 3.1, followed by DWT based parameter computation.

6.3 Topology of Remote End Fault Supervision in Internet of Microgrid Network

Internet of microgrid network framework is structured as depicted in Fig. 6.1 given below, with four Data Capturing Units (DCUs) linked to four buses associated with bulk generator (B-Gen), photovoltaic (P-V), and diesel generators (DG-1 and DG-2). These DCUs constitute the physical layer of the setup. Unlike traditional IoT systems, where physical layers connect directly to the cloud via internet for data storage and processing; a fog computing layer is integrated, as shown in Fig. 6.2, to enhance processing speed. The configuration for remote fault supervision within this IoT-based microgrid system is illustrated in Fig. 6.3.

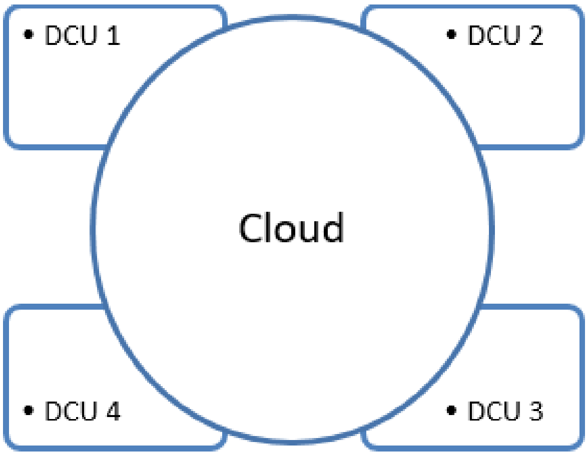

Fig. 6.1: Internet of microgrid through four DCU

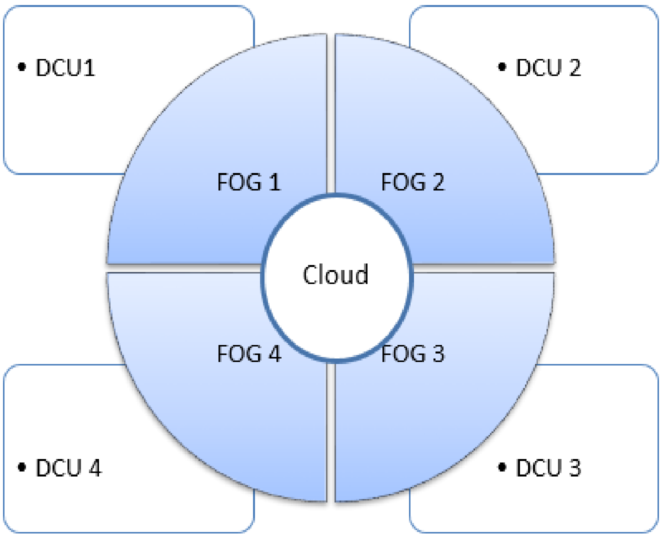

Fig. 6.2: Internet of microgrid through four DCU and fog layer

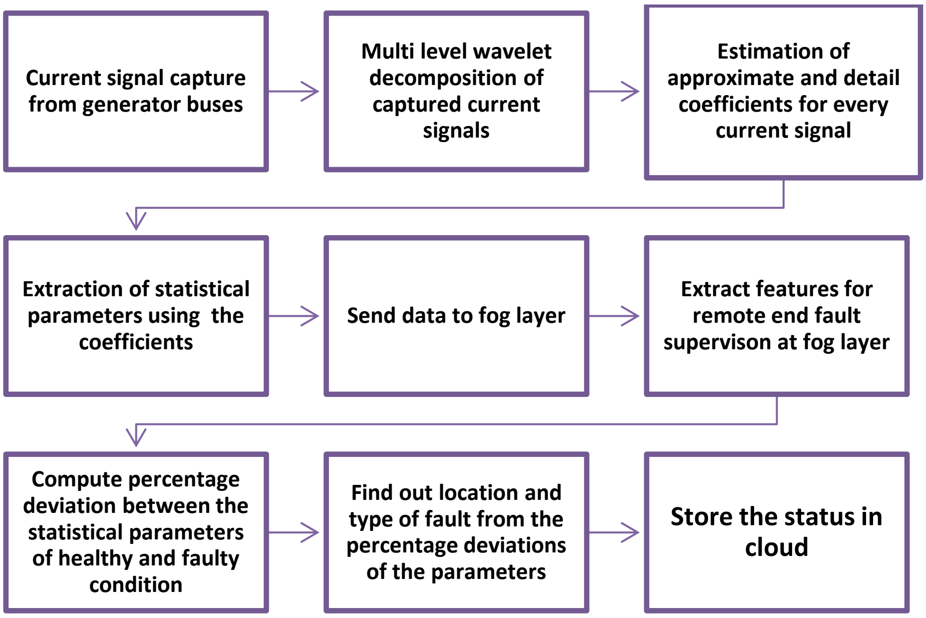

Fig. 6.3: Topology of remote end fault supervision in internet of microgrid system

6.4 Observations Made from Generator Buses

Observed current waveforms of the different generator buses at different conditions have been presented below. In all these waveforms x-axis shows time in seconds and y-axis current in ampere.

6.4.1 Observation from B-Gen Bus

Waveforms of current going out from B-Gen bus at healthy, L-G at B-6 and L-G at B-10 conditions have been shown below in Fig. 6.4, 6.5 and 6.6 respectively.

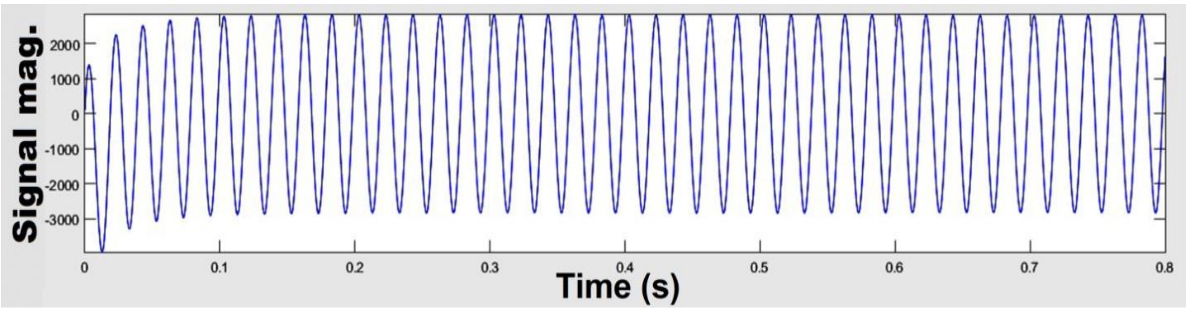

Fig. 6.4: Outgoing current waveform from B-Gen bus at healthy condition

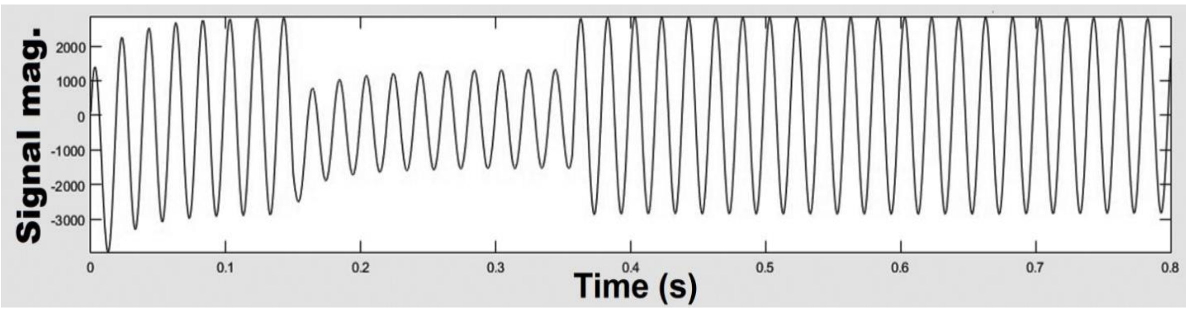

Fig. 6.5: Outgoing current waveform from B-Gen bus with L-G at B-6

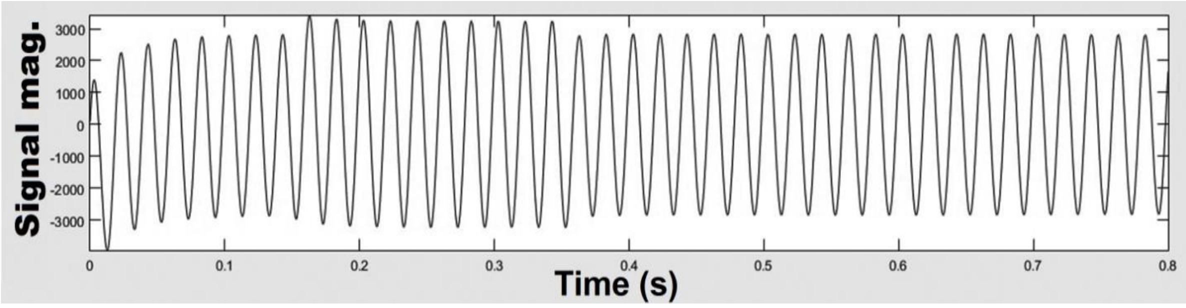

Fig. 6.6: Outgoing current waveform from B-Gen bus with L-G at B-10

6.4.2 Observation from P-V Cell Bus

Waveforms of current going out from B-Gen bus at healthy, L-G at B-6 and L-G at B-10 conditions have been shown below in Fig. 6.7, 6.8 and 6.9 respectively.

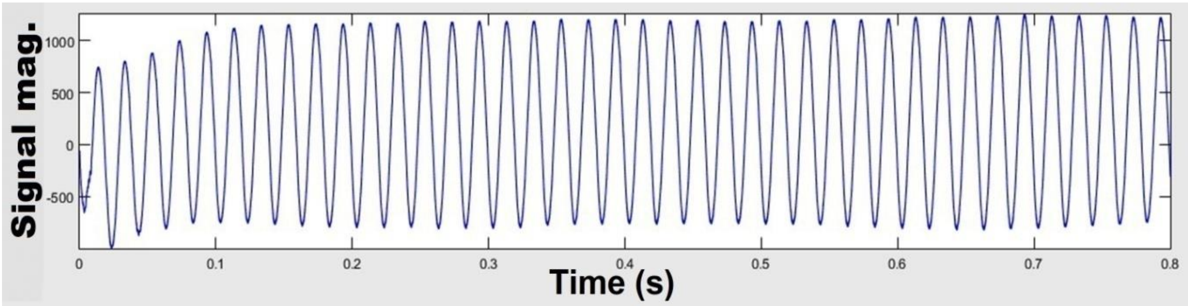

Fig. 6.7: Outgoing current waveform from P-V Cell bus at healthy condition

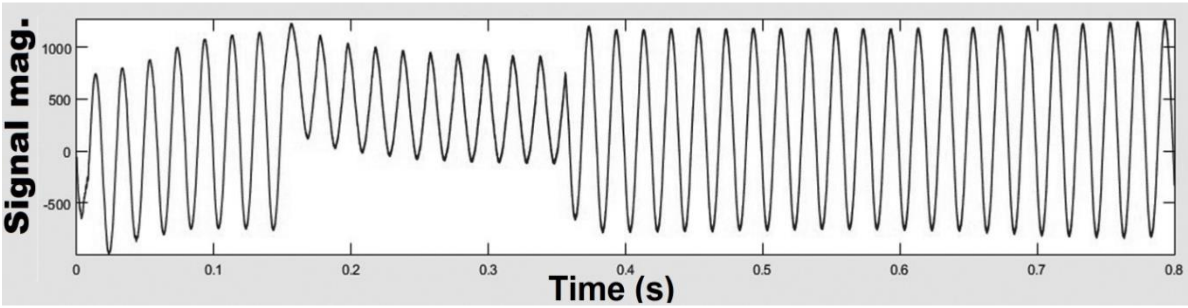

Fig. 6.8: Outgoing current waveform from P-V Cell bus with L-G at B-6

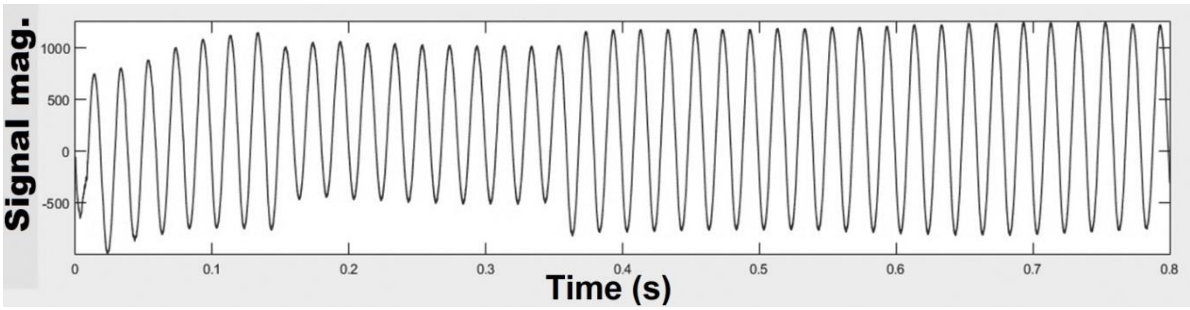

Fig. 6.9: Outgoing current waveform from P-V Cell bus with L-G at B-10

6.4.3 Observation from Diesel Generator – 1 (DG-1) Bus

Waveforms of current going out from DG-1 bus at healthy, L-G at B-6 and L-G at B-10 conditions have been shown below in Fig. 6.10, 6.11 and 6.12 respectively.

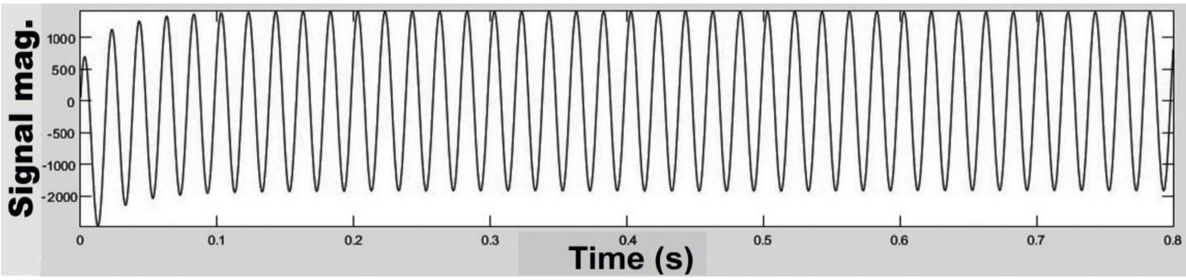

Fig. 6.10: Outgoing current waveform from DG-1 bus at healthy condition

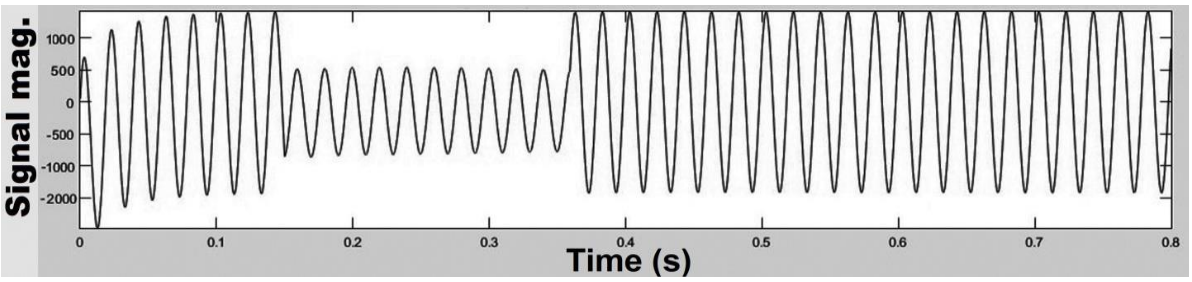

Fig. 6.11: Outgoing current waveform from DG-1 bus with L-G at B-6

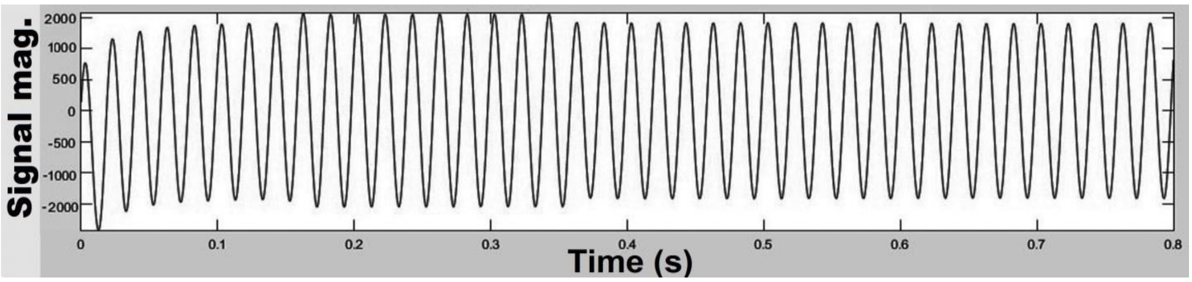

Fig. 6.12: Outgoing current waveform from DG-1 bus with L-G at B-10

6.4.4 Observation from Diesel Generator – 2 (DG-2) Bus

Waveforms of current going out from DG-2 bus at healthy, L-G at B-6 and L-G at B-10 conditions have been shown below in Fig. 6.13, 6.14 and 6.15 respectively.

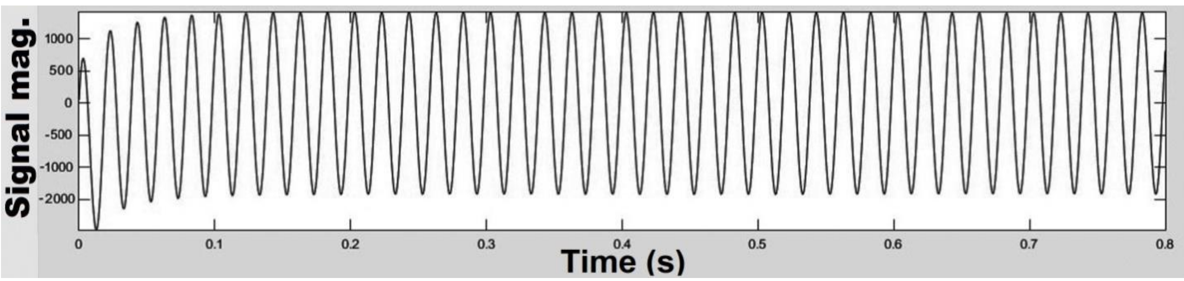

Fig. 6.13: Outgoing current waveform from DG-2 bus at healthy condition

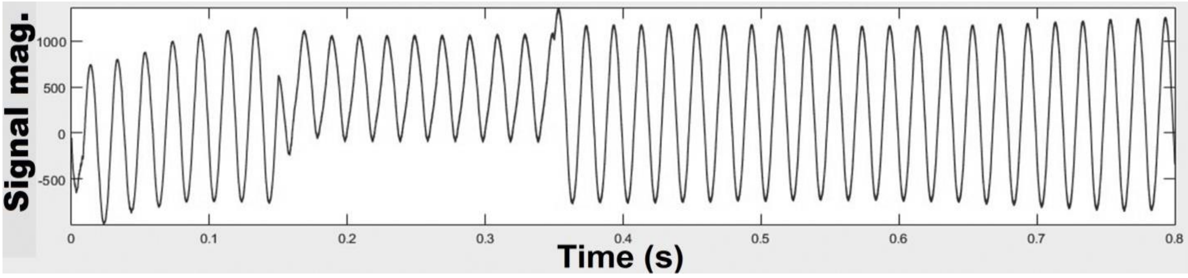

Fig. 6.14: Outgoing current waveform from DG-1 bus with L-G at B-6

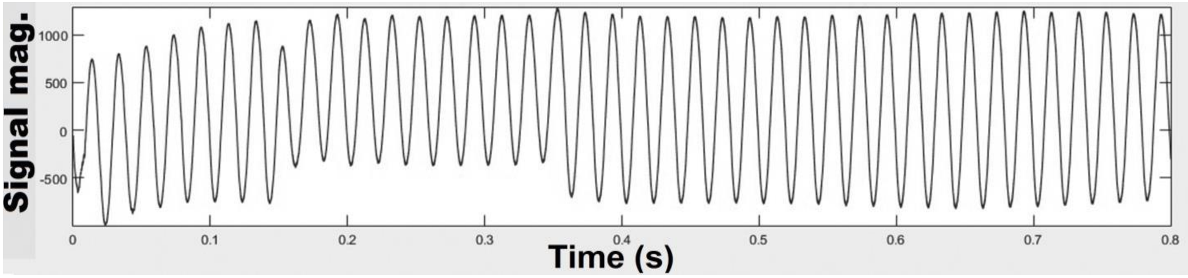

Fig. 6.15: Outgoing current waveform from DG-2 bus with L-G at B-10

The analysis of Fig. 6.4 – 6.15 reveals that the current waveforms exiting various generator buses experience distinct forms of distortion triggered by a fault. DWT was applied to these waveforms and the Root Mean Square (RMS), skewness, and kurtosis values were computed for both approximate and detail coefficients. This methodology was also applied to L-L faults at buses B-6 and B-10. The outcomes of this analysis are discussed in the subsequent section.

6.5 Decision Making

The findings from the DWT derived statistical parameters reveal several key insights. Elevated RMS_A values point to the existence of higher-order harmonics in the current signal, whereas increased RMS_D reflects the presence of lower-order harmonics. A skewness value that strays from zero indicates asymmetry in the spread of both approximate and detail coefficients. Meanwhile, kurtosis measures the peakedness or flatness in the distribution of these coefficients.

Analysis shows that, for currents at specific generator buses, the statistical parameters exhibit varying degrees of shift from their healthy baselines during L-G and L-L faults at buses B-6 and B-10. Consequently, the extent of these shifts can help identify the fault location and type. The relative change from healthy conditions is determined via equation 6.1, as outlined below.

$$\% \text{ Deviation} = \left| \frac{(\text{Healthy value}) - (\text{Faulty value})}{\text{Healthy value}} \right| \times 100 \tag{6.1}$$

6.5.1 Percentage Deviation of Different Parameters of Bulk Generator Bus

The percentage deviations in the outgoing current from the B-Gen bus were determined for six key parameters — RMS_A, RMS_D, S_A, S_D, K_A, and K_D — during L-G and L-L faults at buses B-10 and B-6. These values were derived via equation (6.1) and are depicted in Fig. 6.16 and 6.17, respectively.

In Figure 6.16(a), K_A displays the largest departure from the baseline healthy value among all parameters, occurring at level 9. By comparison, Figure 6.16(b) highlights S_A with the greatest deviation at level 7. Consequently, the prominent deviation in K_A at level 9 for the B-Gen bus serves as an indicator of an L-G fault at bus B-10, whereas the elevated deviation in S_A at level 7 points to an L-G fault at bus B-6. Likewise, Figures 6.17(a) and 6.17(b) illustrate that the highest deviation in S_D at level 9 on the B-Gen bus corresponds to an L-L fault at B-10, while the peak deviation in S_A at level 3 occurs due to an L-L fault at B-6.

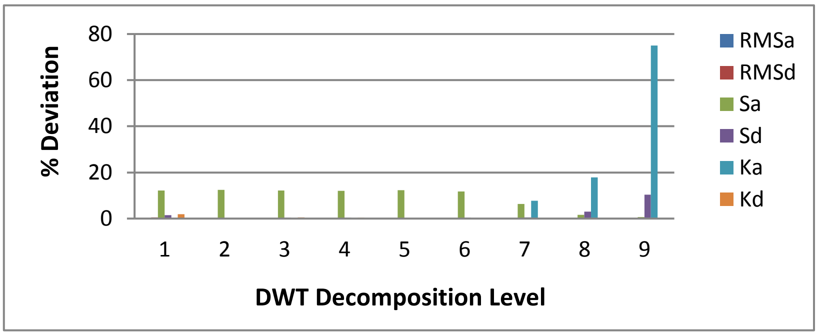

6.16(a)

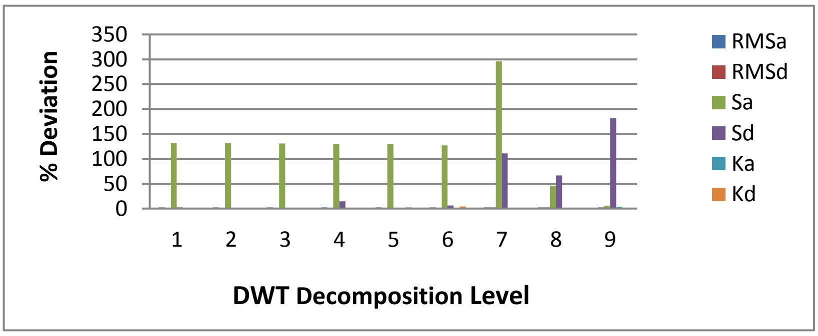

6.16(b)

Fig. 6.16: Comparison of % deviations of different parameters of B-Gen bus for **(a)** L-G fault at B-10 and **(b)** L-G fault at B-6

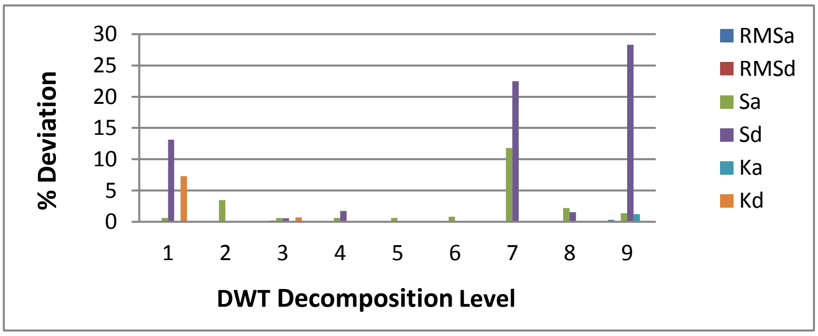

6.17(a)

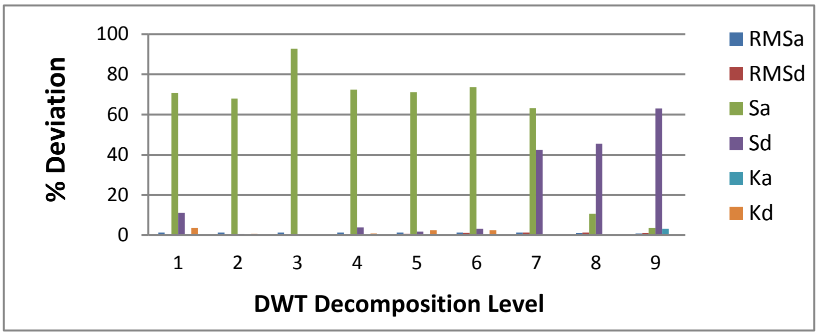

6.17(b)

Fig. 6.17: Comparison of % deviations of different parameters of B-Gen bus for **(a)** L-L fault at B-10 and **(b)** L-G fault at B-6

6.5.2 Percentage Deviation of Different Parameters of P-V Cell Bus

The percentage deviations in the outgoing current from the P-V Cell bus were determined for six key parameters — RMS_A, RMS_D, S_A, S_D, K_A, and K_D — during L-G and L-L faults at buses B-10 and B-6.

As indicated in Figure 6.18(a), S_D for the outgoing current of the P-V Cell bus experiences the greatest shift from its healthy state at decomposition level 8 when an L-G fault happens at B-10. Fig. 6.18(b) reveals that, among all parameters, S_A shows the highest degree of variation at level 8 for an L-G fault at the B-6 bus.

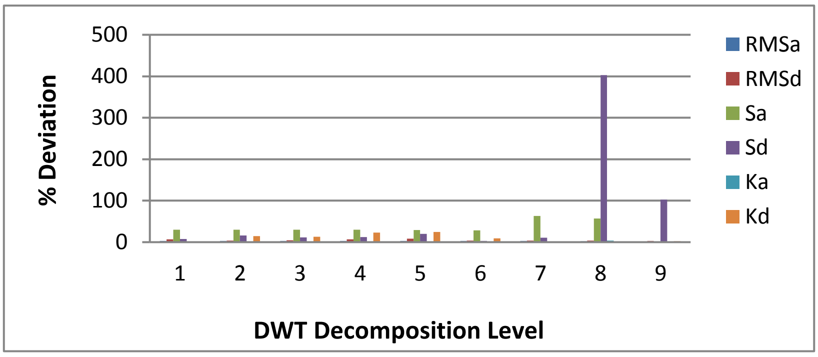

6.18(a)

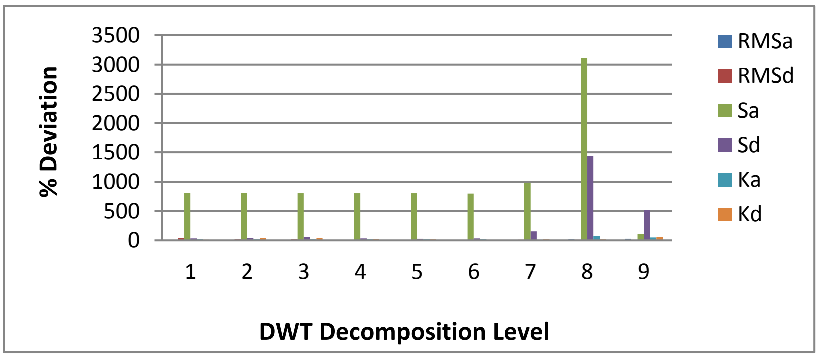

6.18(b)

Fig. 6.18: Comparison of % deviations of different parameters of P-V Cell bus for **(a)** L-G fault at B-10 and **(b)** L-G fault at B-6

Fig. 6.19(a) illustrates that a L-L fault at bus B-10 results in the greatest deviation in K_A value of outgoing current of the PV Cell bus from its value at healthy operating condition at level 9, compared to all the other parameters taken in consideration.

In contrast, Fig. 6.19(b) reveals that the S_D parameter shows the highest deviation at level 4 compared to all other parameters during an L-L fault at bus B-6. Therefore, based on Fig. 6.19(a) and 6.19(b), it can be inferred that the maximum deviation of K_A at level 9 on the P-V Cell bus corresponds to an L-L fault at B-10, while the maximum deviation of S_D at level 4 points to an L-L fault at B-6.

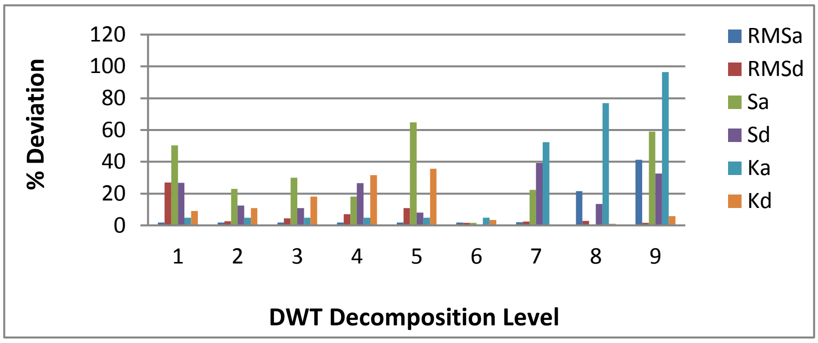

6.19(a)

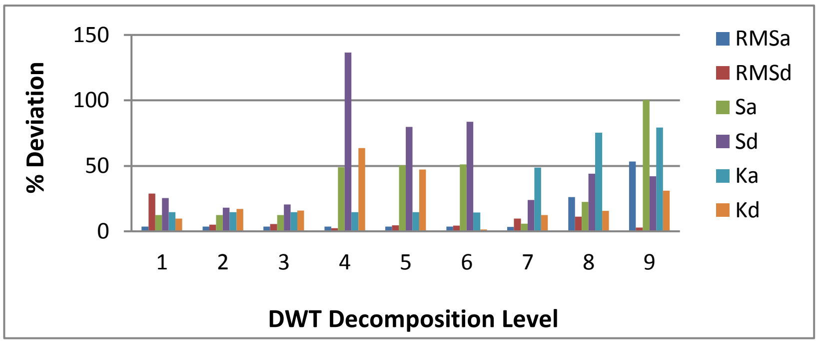

6.19(b)

Fig. 6.19: Comparison of % deviations of different parameters of P-V Cell bus for **(a)** L-L fault at B-10 and **(b)** L-G fault at B-6

6.5.3 Percentage Deviation of Different Parameters of Diesel Generator 1 Bus

Fig. 6.20 and 6.21 given below illustrate the percentage deviations of six parameters for the DG-1 bus during L-G and L-L faults at buses B-10 and B-6.

According to Fig. 6.20(a), parameters RMS_D, S_A, and K_D exhibit notable deviations at lower decomposition levels during an L-G fault at B-10. Amongst these, the K_D parameter shows the most significant deviation at level 4 compared to other parameters. In Fig. 6.20(b), the S_A parameter displays the highest deviation at level 7 when an L-G fault occurs at B-6. Thus, for the DG-1 bus outgoing currents; a maximum K_D deviation at level 4 indicates an L-G fault at B-10, while a maximum S_A deviation at level 7 suggests an L-G fault at B-6.

Figure 6.21(a) indicates that during an L-L fault at B-10, the S_D parameter of the Diesel Generator 1 (DG-1) bus outgoing current experiences the greatest deviation from its normal state at level 7. In contrast, Fig. 6.21(b) shows that the S_D parameter exhibits the most substantial deviation at level 2 among all parameters during an L-L fault at B-6. Therefore, based on the observations made from Fig. 6.21(a) and 6.21(b) it can be said that a maximum deviation in parameter S_D at level 7 for the DG-1 bus points to an L-L fault at B-10, while a maximum deviation in S_D at level 2 suggests an L-L fault at B-6.

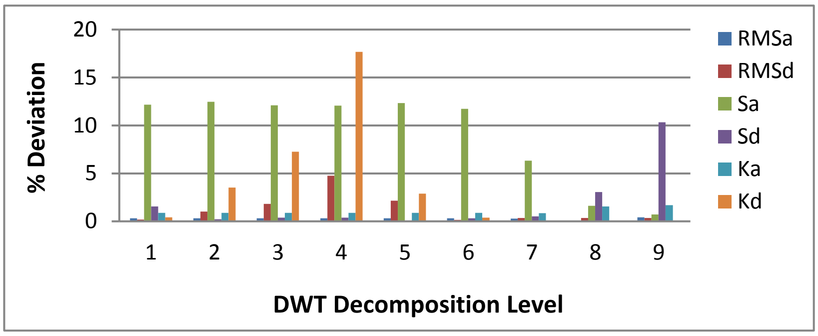

6.20(a)

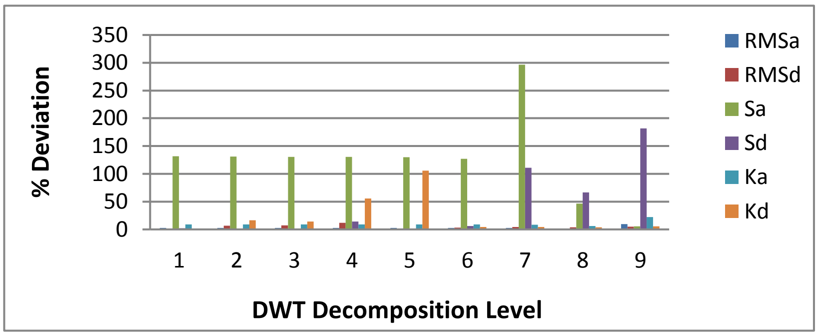

6.20(b)

Fig. 6.20: Comparison of % deviations of different parameters of DG-1 bus for **(a)** L-G fault at B-10 and **(b)** L-G fault at B-6

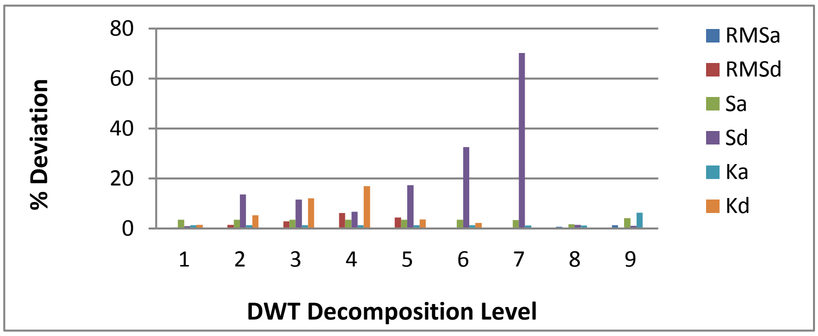

6.21(a)

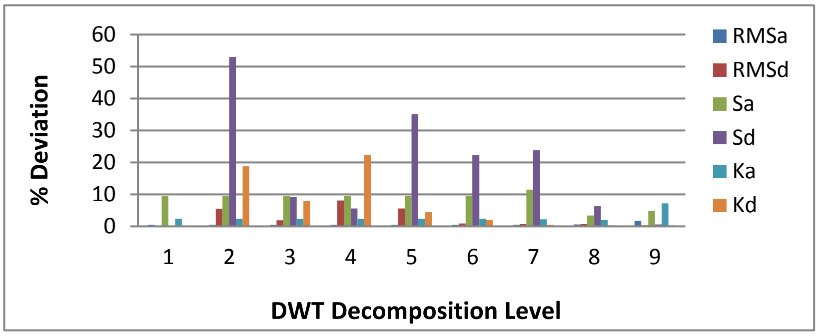

6.21(b)

Fig. 6.21: Comparison of % deviations of different parameters of DG-1 bus for **(a)** L-L fault at B-10 and **(b)** L-G fault at B-6

6.5.4 Percentage Deviation of Different Parameters of Diesel Generator 2 Bus

The variations in the output current parameters of the DG-2 bus during L-G and L-L faults at B-10 and B-6, respectively, are illustrated in Fig. 6.22 and 6.23. Fig.6.22 (a) indicates that for an L-G fault at B-10, K_D has the most substantial deviation from its healthy state value at this level. According to Fig. 6.22(b), an L-G fault at B-6 results in the S_D parameter displaying the highest percentage deviation compared to other parameters at the seventh decomposition level.

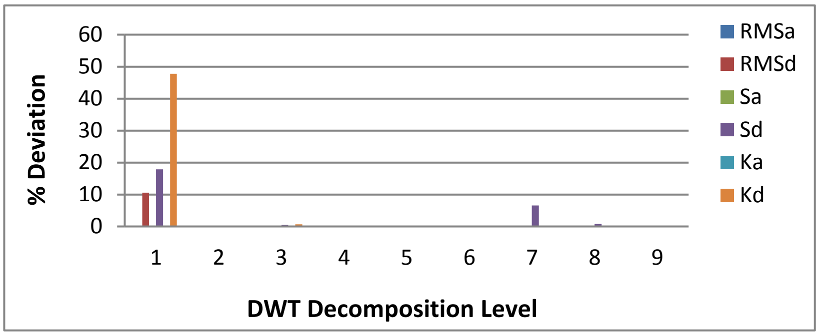

6.22(a)

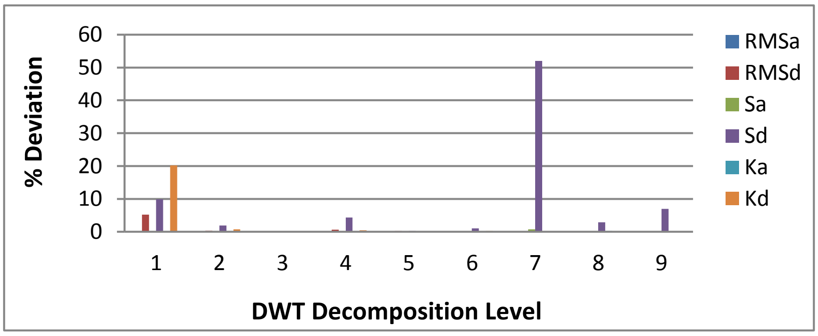

6.22(b)

Fig. 6.22: Comparison of % deviations of different parameters of DG-2 bus for **(a)** L-G fault at B-10 and **(b)** L-G fault at B-6

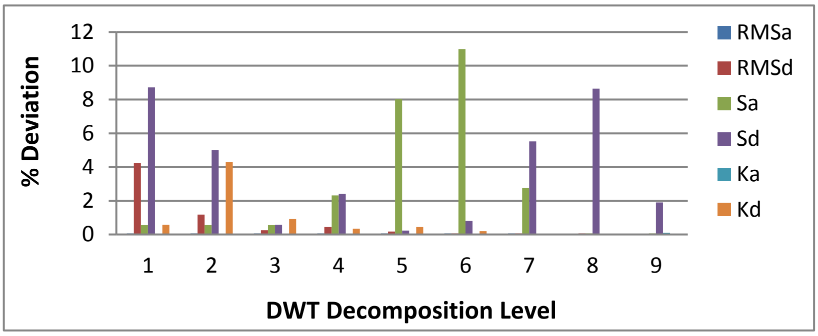

6.23(a)

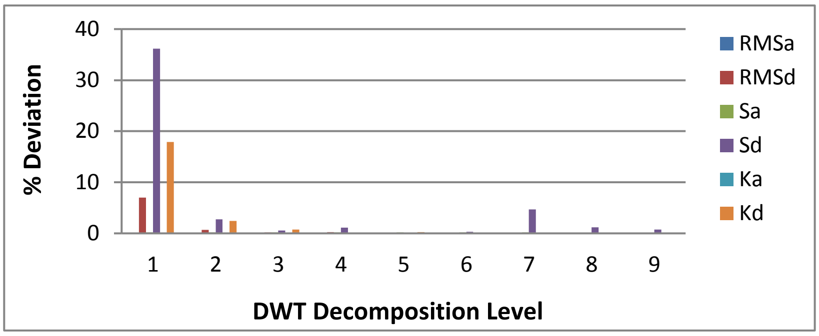

6.23(b)

Fig. 6.23: Comparison of % deviations of different parameters of DG-2 bus for **(a)** L-L fault at B-10 and **(b)** L-G fault at B-6

As depicted in Fig. 6.23(a) presented above, an L-L fault at B-10 results in the S_A parameter of the outgoing current from the DG-2 bus exhibiting the greatest deviation from its healthy state at decomposition level 6. Fig. 6.23(b), given above reveals that, for an L-L fault at B-6, the S_D parameter shows the highest deviation among all parameters at decomposition level 1. Thus, Fig. 6.23(a) and 6.23(b) collectively demonstrate that the maximum deviation of S_A at level 6 for the DG-2 bus signifies an L-L fault at B-10, while the maximum deviation of S_D at level 1 indicates an L-L fault at B-6.

6.6 ANN based Fog Computing

The preceding section conducted a parametric as well as level optimization analysis of six DWT based statistical parameters for the outgoing currents of various generator buses under different conditions. It was observed that, under specific conditions, a particular parameter of a given generator bus current exhibits the highest percentage deviation from its value at healthy condition. The outcomes of the aforementioned optimization are summarized in Table 6.1 below, presented as a rule set. This rule set facilitates the identification of fault type and location by monitoring the outgoing current of any generator bus.

Table 6.1 Rule Set

Observation from	Highest percentage deviation in parameter	Level	Inference
B-Gen	K_A	9	L-G fault at B-10 bus
	S_A	7	L-G fault at B-6 bus
	S_D	9	L-L fault at B-10 bus
	S_A	3	L-L fault at B-6 bus
P-V Cell	S_D	8	L-G fault at B-10 bus
	S_A	8	L-G fault at B-6 bus
	K_A	9	LL fault at B-10 bus
	S_D	4	L-L fault at B-6 bus
DG-1	K_D	4	L-G fault at B-10 bus
	S_A	7	L-G fault at B-6 bus
	S_D	7	L-L fault at B-10 bus
	S_D	2	L-L fault at B-6 bus
DG-2	K_D	1	L-G fault at B-10 bus
	S_D	7	L-G fault at B-6 bus
	S_A	6	L-L fault at B-10 bus
	S_D	1	L-L fault at B-6 bus

Utilizing the rule set provided in Table 6.1, an artificial neural network (ANN) architecture has been made for monitoring of remote-end faults. The eight-layer structure is depicted in Fig. 6.24 given below. The first layer corresponds to data inputs from energy sources, while the second layer represents the Data Collection Unit (DCU). In the third layer, data undergo wavelet decomposition (WD), followed by the formation of coefficient datasets (C) in the fourth layer. Statistical parameters are established in the fifth layer and transmitted to the fog layer. The sixth and seventh layers perform fog computing, extracting features as outlined in Table 6.1 for remote fault supervision. The results are subsequently forwarded to the cloud for status updates and sharing of information.

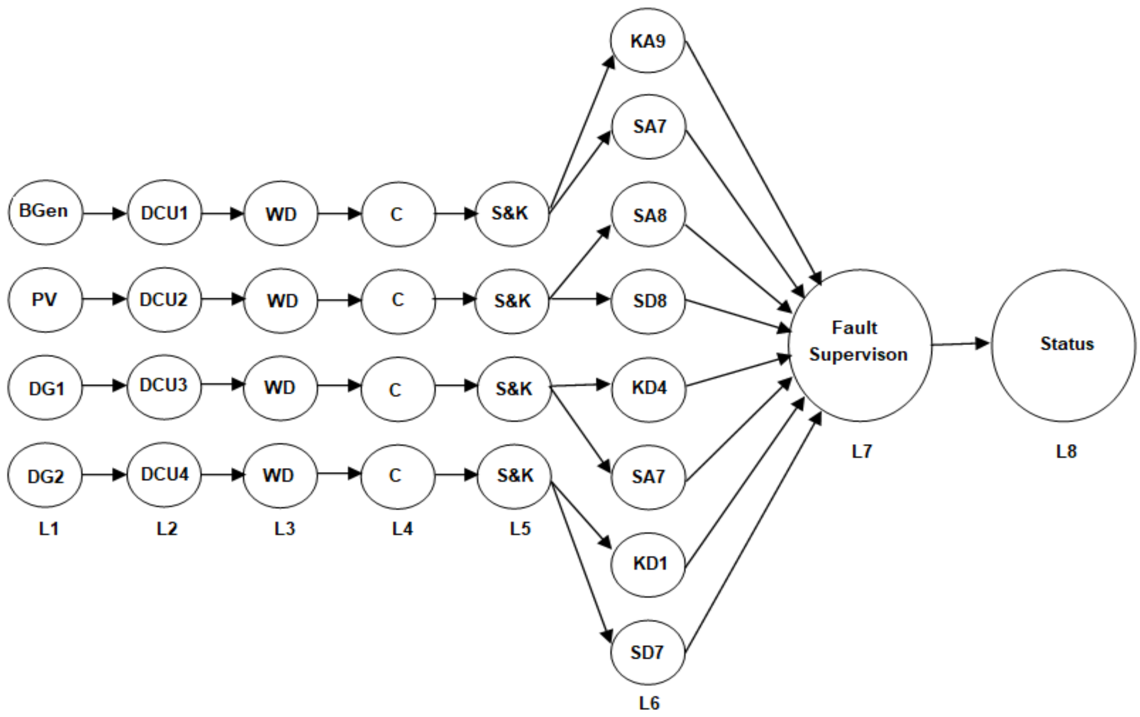

Fig. 6.24: ANN based Fog Computing Architecture

6.7 Validation

The provided rule set has undergone testing for various unspecified scenarios. The outcomes are displayed in Tables 6.2, 6.3, 6.4, and 6.5 below.

Table 6.2 displays the percentage deviation from the baseline healthy condition value recorded at the B-Gen bus. Analysis of Table 6.2 reveals that in ‘Case: 1’, the highest percentage deviation occurs at 9^{th} level of parameter K_A. By applying the rule set outlined in Table 6.1, it is determined that the fault is located at B-10 and is of the L-G type in this unidentified scenario. In ‘Case: 2’, the greatest percentage deviation is observed at 7^{th} level of parameter S_A. Based on the rule set in Table 6.11, it can be inferred that an L-G fault has occurred at B-6.

On the other hand, Table 6.3 illustrates the percentage deviation from the baseline healthy condition value recorded at the P-V Cell bus. As indicated in Table 6.3 below, the position of the L-G fault is determined from the P-V Cell bus by leveraging the findings from parametric and level optimizations.

Table 6.2 Percentage Deviation from the Healthy Condition value measured from B- Gen bus

Different Cases	DWT Level	K_A	S_A	Remarks
Case 1: Total computing time 1sec, Fault duration 0.3 - 0.5 sec	1	0.012	29.095	L-G fault at B-10
	2	0.018	28.992	
	3	0.012	28.995	
	4	0.012	27.658	
	5	0.012	27.220	
	6	0.009	21.087	
	7	0.045	16.311	
	8	23.82	9.658	
	9	**81.59**	2. 224	
Case 2: Total computing time 1.2sec, Fault duration 0.4 - 0.6 sec	1	1.733	130.4	L-G fault at B-6
	2	1.705	130.4	
	3	1.705	130.0	
	4	1.705	129.5	
	5	1.652	129.5	
	6	1.981	125.8	
	7	2.054	**338.7**	
	8	2.187	31.95	
	9	2.188	8.245	

Table 6.3 Percentage Deviation from the Healthy Condition value measured from P-V Cell bus

Different Cases	DWT Level	S_D	S_A	Remarks
Case 1: Total computing time 1sec, Fault duration 0.3 - 0.5 sec	1	0.235	41.572	L-G fault at B-10
	2	11.221	41.588	
	3	13.305	41.591	
	4	15.473	41.618	
	5	7.6924	41.777	
	6	14.899	39.953	
	7	87.992	57.884	
	8	**491.28**	57.438	
	9	231.03	11.782	
Case 2: Total computing time 1.2sec, Fault duration 0.4 - 0.6 sec	1	89.625	778.9	L-G fault at B-6
	2	91.220	778.8	
	3	95.913	778.1	
	4	95.298	776.8	
	5	80.783	776.9	
	6	77.199	776.8	
	7	229.51	920.6	
	8	852.01	**3889.2**	
	9	772.39	106.9	

Table 6.4 and 6.5 illustrate the percentage deviation from the baseline healthy condition value recorded at the DG-1 and DG-2 bus respectively. These tables demonstrate the determination of L-G fault positions in two unspecified scenarios from the DG-1 and DG-2 bus, utilizing the outcomes of parametric and level optimizations outlined in Table 6.1.

Table 6.4 Percentage Deviation from the Healthy Condition value measured from DG-1 bus

Different Cases	DWT Level	K_D	S_A	Remarks
Case 1: Total computing time 1sec, Fault duration 0.3 - 0.5 sec	1	1.757	9.532	L-G fault at B-10
	2	2.459	9.421	
	3	5.349	9.220	
	4	**19.98**	9.025	
	5	1.968	9.005	
	6	1.180	8.753	
	7	0.008	5.426	
	8	0.049	2.558	
	9	0.015	1.112	
Case 2: Total computing time 1.2sec, Fault duration 0.4 - 0.6 sec	1	1.228	78.097	L-G fault at B-6
	2	11.61	78.072	
	3	28.55	78.074	
	4	69.70	78.053	
	5	99.62	78.093	
	6	19.62	78.191	
	7	10.00	**218.55**	
	8	5.261	114.43	
	9	4.781	25.119	

Table 6.5 Percentage Deviation from the Healthy Condition value measured from DG-2 bus

Different Cases	DWT Level	K_D	S_D	Remarks
Case 1: Total computing time 1sec, Fault duration 0.3 - 0.5 sec	1	**38.271**	7.996	L-G fault at B-10
	2	7.137	2.249	
	3	5.924	2.344	
	4	3.772	1.002	
	5	3.363	0.224	
	6	1.922	0.047	
	7	2.643	7.210	
	8	0.601	0.894	
	9	0.413	0.583	
Case 2: Total computing time 1.2sec, Fault duration 0.4 - 0.6 sec	1	4.111	6.379	L-G fault at B-6
	2	1.298	5.895	
	3	1.155	1.818	
	4	1.317	1.766	
	5	1.025	1.076	
	6	1.069	22.18	
	7	1.010	**194.5**	
	8	0.823	3.529	
	9	0.731	14.99	

The power outputs of distributed energy resources (DERs) were adjusted in three stages—100%, 80%, and 50%—to account for their inherent uncertainties. Under these conditions, the magnitudes of individual current harmonic components exhibited some variation. Nonetheless, the percentage deviations of the statistical parameters, derived from the discrete wavelet transform (DWT) decomposition results compared to their baseline healthy condition values, showed minimal or no significant changes. Consequently, the rule set described here effectively identified both the fault location and fault type, even with varying DER outputs.

The suggested rule set was also evaluated under conditions involving simultaneous multiple faults, such as an L-G fault at B-6 and an L-L fault at B-10 occurring concurrently. In this multi-fault scenario, the rule set effectively identifies the type and location of the most critical fault. In the given example, the L-G fault at B-6 was determined to be the more severe of the two faults, and the rule set accurately detected it.

The rule set outlined in Table 6.1 was further validated through its application in an IEC 61850-7-420 microgrid network. L-G and L-L faults were intentionally triggered at load buses, and the outgoing currents from the conventional generator bus and photovoltaic bus were evaluated using the methods proposed in this study, with the rule set subsequently applied. Similar to the IEEE standard 14 bus network, the results obtained from the rule set in this scenario were highly satisfactory.

6.8 Summary

This study explores fault monitoring at remote ends in an IEEE 14-bus microgrid system using fog computing and discrete wavelet transform (DWT)-based statistical methods. Previous studies have employed Stockwell Transform-based approaches for fault detection. However, these methods generate large S-Transform matrices as simulation time increases, demanding significant computational memory. Consequently, in this study, S-Transform-based techniques were avoided in algorithm development due to their high memory requirements and slower processing compared to discrete wavelet transform (DWT). The DWT-based approach achieved the fastest response time, recorded at 0.014 seconds.

The analysis focuses on the outgoing current from various generator buses under normal and fault conditions, specifically when line-to-ground (L-G) or line-to-line (L-L) faults occur at load buses. For the sake of simplicity, only L-G and L-L faults are considered and only two load buses – Furnace bus (B-6) and Non-linear load bus (B-10) have been taken into account. A rule-based framework, derived from DWT analysis with optimized parameters and levels, was established, yielding reliable results for fault location identification. The proposed approach offers multiple benefits compared to traditional methods, as it operates independently of network voltage and current magnitudes and remains unaffected by variations in fault resistance, including arc resistances in earth faults. Consequently, this method is highly effective for detecting earth faults in microgrid systems. Additionally, it enables fault detection from a remote generator bus when faults occur at load buses. The integration of a fog computing layer enhances decision-making speed and reduces cloud storage demands. This approach can be further developed to analyze other fault types and enable fault detection from additional buses within the microgrid network.

Publication:

S. Datta, A. Chattopadhyaya, S. Chattopadhayay & A. Das, "ANN Based Statistical Computation for Remote End Fault Monitoring of IEEE 14 Bus Microgrid Network", IETE Journal of Research, March 2023, DOI: 10.1080/03772063.2023.2182371

Chapter 7

General Conclusion

In this thesis, some of the existing hurdles of fault type detection and fault location identification in a microgrid environment have been overcome with satisfactory accuracy. Instead of working with the magnitudes of different harmonics components present in the out-going currents from various generator buses, main focus was to examine the variations in the statistical nature of the current harmonics. Subsequent sections outline a brief summary of the work done and a comparison between the fault detection rule-sets proposed here with the existing algorithms discussed in the literature review.

7.1 Summary of Work Done

The work presented here can be categorized into two broad categories: DWT based and S – Transformation based statistical parameter analysis of various generator bus out-going currents for remote-end bus fault assessment inside a microgrid network. A brief experiment with FFT has also been carried out which produced very low accuracy in determining correct location as well as type of the fault which occurred in the load bus. FFT could not produce satisfactory results because of the non-stationary nature of the current signals during occurrence of the fault. IEEE-Standard 14 bus microgrid network is used in this work. It is shown in Fig. 3.1. However, the rule-sets formed, are tested in multiple unknown situations in IEEE-Standard 14 bus microgrid network as well as IEC 61850-7-420 network. In both networks the rule-sets worked satisfactorily.

7.1.1 DWT based Fault Assessment

To analyze generator bus out-going currents using DWT, the currents signals are examined under different conditions. Initially, the current signal is broken down into two levels — approximate and detail — by application of low-pass and high-pass filters, respectively. This process of decomposition is repeated nine times, yielding nine levels of both approximate and detail levels. The analysis focuses on the first twenty harmonics, covering current components up to 1000 Hz. Nine decomposition levels are used to capture current components within the 1–1000 Hz frequency range. After decomposition, each level is down-sampled to obtain approximate and detail coefficients, where approximate coefficients represent lower-frequency components and detail coefficients higher-frequency components. Statistical parameters, including RMS, skewness, and kurtosis, are computed for each level based on these coefficients. The Daubechies-4 (DB-4) wavelet is selected as the mother wavelet for this DWT analysis, as it proved to be the most effective after testing other wavelets such as DB-3 and DB-10.

The presence of higher and lower order harmonics within a signal leads to elevated RMS_A and RMS_D values, respectively. Asymmetry in the distribution of approximate and detail coefficients results in skewness values deviating from zero. Meanwhile, the kurtosis values are determined by the peakedness of the distribution of these approximate and detail coefficients. When fault occurs at a bus, various parameters of the out-going current from a specific generator bus exhibit distinct deviations from their normal condition values. Consequently, the location of the fault can be identified based on the extent of deviations of these parameters. The percentage deviation of each parameter from its normal condition value is computed using equation (3.2). An optimization process was carried out for parameters and decomposition levels for all the six statistical parameters (RMS_A, RMS_D, S_A, S_D, K_A and K_D) derived from DWT evaluation of currents flowing out from various generator buses in different conditions. It was noted that, in a given situation, a specific statistical parameter associated with the current at a particular generator bus demonstrates the maximum percentage deviation relative to its baseline value during normal operation. These optimization findings for parameters and levels are given in the form of a rule-set in Table 3.30.

Utilizing the proposed rule set, artificial neural network (ANN) architecture has been made for monitoring of remote-end faults. The eight-layer structure is depicted in Fig. 6.24. The results are subsequently forwarded to the cloud for status updates and sharing of information. The integration of a fog computing layer enhances decision-making speed and reduces cloud storage demands.

The power outputs of distributed energy resources (DERs) were change in three steps—100%, 80%, and 50%—to account for their inherent uncertainties. Under these conditions, the magnitudes of individual current harmonic components exhibited some variation but the percentage deviations of the statistical parameters, derived from the DWT decomposition showed minimal or no significant changes compared to their baseline healthy condition values. Consequently, the proposed rule-set effectively identified both the fault location and fault type, even with varying DER outputs.

Moreover, the proposed rule-set is also tested under scenarios with multiple simultaneous faults, such as an L-G fault at furnace bus (B-6) occurring alongside an L-L fault at the non-linear load bus (B-10) of the IEEE-Standard 14 bus network. In these multi-fault conditions, the rule set successfully determines the type and location of the most severe fault.

Compared to traditional approaches, the suggested technique provides multiple benefits.

- It functions independently of the voltage and current levels across the system.
- Changes in fault resistance have no impact on its performance. Consequently, arc resistances of ground faults do not influence the effectiveness of the outlined rules. This makes the technique particularly effective for identifying ground faults within microgrid networks.

- It supports fault identification from remote ends, given that faults were happening at load buses while monitoring occurred at the generator bus.

7.1.2 S – Transformation based Fault Assessment

Fault assessment with Stockwell Transform (S-Transform) is done to rule out mainly one problem involved with the DWT based analysis. Accuracy of DWT based analysis is heavily dependent on the correct choice of the mother wavelet. However, in S-Transform, mother wavelet selection is not needed.

Statistical analysis of the S-Transformation matrices is carried out and subsequently unique algorithms are developed for fault assessment. The IEEE-Standard 14 Bus Microgrid Network is depicted in Fig.3.1, is utilized to simulate a Line-to-Ground (L-G) fault at bus B-6 (furnace bus) and bus B-10 (non-linear load bus), phase 'C' is connected to the ground. Similarly, Line-to-Line (L-L) and Line-to-Line-to-Ground (L-L-G) faults are created using phases 'B' and 'C' at these specified load buses. Additionally, a three-phase (L-L-L) fault is evaluated at the same load buses. Only two load buses were chosen for the sake of simplicity and also to streamline the study. The current signals from phase 'C' of two generator buses — the bulk generator bus and the P-V Cell bus are observed. The simulation was run for a total of 0.5 seconds, with faults introduced between 0.15 and 0.35 seconds. To avoid aliasing, a high sampling rate of 1000 Hz is chosen. A brief simulation duration is selected to ensure a manageable data size.

Currents from phase 'C' of bulk generator bus and P-V Cell bus are evaluated at seven different conditions - healthy, L-G, L-L, L-L-G, and L-L-L faults at buses B-6 and B-10 using the S-Transform resulting in formation of S-Transformation matrices. These matrices capture the current magnitudes across various frequencies at specific time instants. The skewness and kurtosis of the S-Transformation matrices are calculated, and plots of skewness vs. time and kurtosis vs. time are created. Faults cause the harmonic components of the current signals to change, resulting in variations in the elements of the S-Transform matrices and their associated skewness and kurtosis values.

Both skewness vs. time and kurtosis vs. time plots in every condition exhibited two distinct zones as depicted in Fig. 5.1 – 5.17. These zones are termed as Zone – 1 and Zone – 2. Six novel parameters (FPP, FNP, DZ_1, SPP, SNP and DZ_2) are established by studying the features of the aforementioned skewness vs. time and kurtosis vs. time graphs. It is observed that values of these parameters gets changed from healthy conditions values with occurrence of the faults. Any change in type and location of the fault also alter the values of these parameters. Furthermore, it is noticed that in both cases, with occurrence of faults one or two specific parameters out of the six, possess the maximum deviation from their healthy condition value. These are identified as the most effective for determining the fault type and identifying the fault location, leading to the development of a corresponding algorithm. In case of skewness based analysis the best parameter for the said purpose was SPP and DZ_2 and for kurtosis based analysis the most well suited parameter was DZ_2.

The algorithm is tested in various unknown conditions including the cases where the outputs of the DERs are varied. In all the cases, it performed satisfactorily. It is also tested in 'IEC 61850-7-420' microgrid network. In that network faults have been made to occur at load buses and outgoing currents from the bulk generator bus and also Photovoltaic (PV Cell) bus are analysed with the proposed method. Alike IEEE-standard 14 bus network in this microgrid network also the results obtained through this method are found to be very much satisfactory.

The proposed method offers several key advantages:

- It does not require knowledge of line parameters or wave velocity.
- Compared to prior S-Transformation-based techniques, it is significantly faster, requiring fewer parameters to identify fault locations and types, with a computational time of 0.015 seconds.
- The method is unaffected by fault resistance, as it relies on the statistical analysis of harmonic content in generator bus outbound currents, which is independent of resistive elements in the network.
- It is particularly effective for earth faults, as these are not influenced by arcing resistance, making it highly suitable for detecting earth faults in short-length lines commonly found in microgrid environments.

Both DWT and S – Transformation based techniques are unaffected by the noise present in the system. In both the analyses only the first twenty harmonics are considered i.e. for a 50 Hz system frequency, only harmonics falling inside the 1 – 1000 Hz range are taken into account. Noise signals generally have much higher frequency so those signals got excluded from the computation automatically.

7.2 Comparison of Different Methods

Brief comparative studies between various signal-processing tools have been shown below in Table 7.1.

Table 7.1 Comparison between different Signal Processing Tools

Sl. No.	Name of Signal Processing Tool	Special mathematical functions	Computational time	Other information
1	Fast-Fourier-Transform (FFT)	Needs a suitable window function.	Slower than both S – Transform and DWT.	For analysis of non-stationery signals it is not suitable.
2	Discrete Wavelet Transform (DWT)	Needs a suitable mother-wavelet function. Proper selection of the mother-wavelet is necessary to achieve high accuracy.	Fastest response (0.014 seconds).	The fastest computational time but a choice of mother-wavelet dictates the accuracy of the analysis.
3	Stockwell Transform (S - Transform)	No special mathematical function is needed to be considered for computation.	With respect to FFT, it is faster but slower than DWT. Response time is 0.015 seconds.	Though S-transform is slightly slower than DWT its accuracy is independent of the choice of any other mathematical function. So, accuracy is high.

Main advantage of DWT based method is the fast response time. However, accuracy is dependent upon proper choice of mother wavelet function. S – Transformation based methods do not require any mother wavelet functions but it is has slower response time than DWT based method but S – Transformation matrices are large and demand significant amount of computational memory. So, if large computational memory is readily available then S –Transformation based methods are very effective although a bit slower than DWT based method.

7.3 General Outcomes

The work presented here, shows a comprehensive approach to remote-end fault analysis in microgrid environment using Discrete Wavelet Transform (DWT) and Stockwell Transform (S-Transform) based statistical analysis of generator bus outgoing currents. Both methods aim to accurately identify fault type and location, even when faults occur at distant load buses.

The DWT-based technique employs wavelet decomposition and statistical parameter optimization to build a rule-set, which is effectively integrated with ANN and fog computing architecture for real-time fault monitoring. It provides rapid response time, resilience against variations in DER outputs, and independence from voltage/current magnitudes and fault resistance variations.

The S-Transform-based method analyzes time-frequency matrices without needing a predefined mother wavelet. Novel statistical parameters derived from skewness and kurtosis trends enable efficient fault classification and localization, with high accuracy and low computational time, even under multiple fault scenarios and varying DER outputs.

Both methods are tested and validated on the IEEE Standard 14-bus and IEC 61850-7-420 microgrid models, showing excellent performance in diverse and unknown conditions. While the DWT method excels in speed, the S-Transform based approach offers greater flexibility and accuracy, albeit with higher memory and computational requirements.

7.4 Societal Benefit of the Work

This thesis presents innovative techniques for accurately detecting and classifying faults in microgrid-based power distribution networks. A key contribution of this work is its ability to identify both the type of fault and its precise location, even when the fault occurs at distant load buses that are typically difficult to monitor. The proposed approaches improve the speed and accuracy of fault diagnosis, enabling quicker isolation and mitigation of problematic sections within the network. As a result, disruptions can be minimized and the overall performance of the power system can be maintained. By enhancing the reliability and resilience of microgrid power distribution, these methods help ensure a stable and continuous electricity supply for households, businesses, and essential services. Reliable electricity is fundamental to modern life, supporting economic activities, healthcare, communication, and daily living. Therefore, this research contributes to building safer, more dependable, and sustainable energy infrastructure that benefits both individual users and society as a whole.

7.5 Future Scope of Work

The work presented here may be extended in the following ways:

- The current work can be expanded such that the algorithm successfully identifies type and location of faults in other buses and also detects the effect of CT saturation.
- Algorithm can be modified to detect and differentiate between faults and power quality disturbances.
- Advanced machine learning techniques such as convolutional neural networks (CNNs), recurrent neural networks (RNNs), can be employed and also modern classifiers like support vector machine (SVM) can be incorporated.

- While the present study is conducted on the IEEE-Satndard 14-bus and IEC 61850-7-420 networks, the proposed methods can be extended and tested on larger standard test systems (e.g., IEEE 33-bus or 69-bus) to assess scalability and adaptability.
- Practical implementation of the work may be done using high-speed voltage and current sensors, including current transformers (CTs) and potential transformers (PTs), which would be placed at key buses and feeders in the microgrid (modelled after the IEEE 14-bus system). These sensors would continuously capture electrical signals, which are then sampled in real time using data acquisition devices. The acquired measurements would be forwarded to a local processing unit—such as an embedded controller, digital signal processor (DSP), or industrial computer—for initial signal conditioning and synchronization. The processing sequence begins with the application of the Discrete Wavelet Transform to break down the signals and identify transient events. Subsequently, the Stockwell Transform is employed to extract detailed time-frequency information, particularly useful under varying operating conditions. Relevant statistical features derived from both transforms are then fed into a pre-trained decision-making algorithm or machine learning-based classifier to determine the nature and location of the fault. The resulting diagnostic decision would be communicated to the microgrid's protection infrastructure, including relays and circuit breakers, to enable rapid isolation of the affected section. This framework can be implemented either through a centralized controller located at the microgrid control centre or in a distributed architecture across multiple intelligent electronic devices (IEDs). Such flexibility supports scalability, minimal response time, and strong performance for real-time fault detection, even in the presence of high renewable energy penetration, fluctuating loads, and noisy measurement environments.

References

[1] Dehghanpour, E., & Kheirollahi, R. (2016, February). Developing a new fault location topology for DC microgrid systems. In 2016 7th Power Electronics and Drive Systems Technologies Conference (PEDSTC).

[2] Dhar, S., Patnaik, R. K., & Dash, P. K. (2017). Fault detection and location of photovoltaic based DC microgrid using differential protection strategy. IEEE Transactions on Smart Grid, 9(5), 4303-4312.

[3] Kar, D., Chattopadhyay, S., Sharma, K. D., & Sengupta, S. (2016, January). Identification of faulty load bus in a multi-bus power system. In 2016 2nd International Conference on Control, Instrumentation, Energy & Communication (CIEC) (pp. 289-293). IEEE.

[4] Ray, D. K., Chattopadhyay, S., Sharma, K. D., & Sengupta, S. (2015, September). Steady state harmonic stability analysis in IEEE 14 bus system for fault at generator bus. In Michael Faraday IET International Summit 2015 (pp. 261-266). IET.

[5] Azevedo, G. M., Arruda, J. P., Cavalcanti, M. C., & Limongi, L. R. (2015, November). Fault detection system to trigger the microgrid disconnection procedures. In 2015 IEEE 13th Brazilian Power Electronics Conference and 1st Southern Power Electronics Conference (COBEP/SPEC) (pp. 1-6). IEEE.

[6] Madingou, G., Zarghami, M., & Vaziri, M. (2015, February). Fault detection and isolation in a DC microgrid using a central processing unit. In 2015 IEEE Power & Energy Society Innovative Smart Grid Technologies Conference (ISGT) (pp. 1-5). IEEE.

[7] Aziz, T., & Deeba, S. R. (2016, September). Investigation of post-fault voltage recovery performance with battery-based energy storage system in a microgrid. In 2016 Australasian Universities Power Engineering Conference (AUPEC) (pp. 1-6). IEEE.

[8] Mirsaeidi, S., Dong, X., Shi, S., & Tzelepis, D. (2017). Challenges, advances and future directions in protection of hybrid AC/DC microgrids. IET Renewable Power Generation, 11(12), 1495-1502.

[9] Farjah, E., Musavi, S., & Ghanbari, T. (2015, July). Appropriate interaction of the microgrid and main network by using unidirectional fault current limiters. In 2015 Modern Electric Power Systems (MEPS) (pp. 1-6). IEEE.

[10] Wen, S., Wang, Y., Tang, Y., Xu, Y., & Li, P. (2019). Proactive frequency control based on ultra-short-term power fluctuation forecasting for high renewables penetrated power systems. IET Renewable Power Generation, 13(12), 2166-2173.

[11] Chen, J. L., Kuo, C. L., Chen, S. J., Kao, C. C., Zhan, T. S., Lin, C. H., & Chen, Y. S. (2016). DC-side fault detection for photovoltaic energy conversion system using fractional-order

dynamic-error-based fuzzy Petri net integrated with intelligent meters. IET Renewable Power Generation, 10(9), 1318-1327.

[12] Makwana, Y. M., & Bhalja, B. R. (2017). Islanding detection technique based on superimposed components of voltage. *IET Renewable Power Generation*, *11*(11), 1371-1381.

[13] Manohar, M., Koley, E., & Ghosh, S. (2019). Enhancing the reliability of protection scheme for PV integrated microgrid by discriminating between array faults and symmetrical line faults using sparse auto encoder. IET Renewable Power Generation, 13(2), 308-317.

[14] Ghanbari, T., & Farjah, E. (2012). Unidirectional fault current limiter: An efficient interface between the microgrid and main network. IEEE Transactions on Power Systems, 28(2), 1591-1598.

[15] Chattopadhyay, S., Chattopadhyaya, A., & Sengupta, S. (2014). Measurement of harmonic distortion and Skewness of stator current of induction motor at crawling in Clarke plane. IET Science, Measurement & Technology, 8(6), 528-536.

[16] Chattopadhyay, S., Chattopadhyaya, A., & Sengupta, S. (2014). Analysis of stator current of induction motor used in transport system at single phasing by measuring phase angle, symmetrical components, Skewness, Kurtosis and harmonic distortion in Park plane. IET Electrical Systems in Transportation, 4(1), 1-8.

[17] Akhtar, I., & Kirmani, S. (2022). An application of fuzzy fault tree analysis for reliability evaluation of wind energy system. IETE Journal of Research, 68(6), 4265-4278.

[18] Raval, P. D., & Pandya, A. S. (2022). A hybrid PSO-ANN-based fault classification system for EHV transmission lines. IETE journal of research, 68(4), 3086-3099.

[19] Ikhide, M., Tennakoon, S. B., Ha, H., Griffiths, A. L., Subramanian, S., & Adamczyk, A. J. (2019). A transient and non-unit-based protection technique for DC grids based on the rate-of-change (RoC) of the fault induced travelling wave components. Sustainable Energy, Grids and Networks, 17, 100195.

[20] Mishra, M., Sahani, M., & Rout, P. K. (2017). An islanding detection algorithm for distributed generation based on Hilbert–Huang transform and extreme learning machine. Sustainable Energy, Grids and Networks, 9, 13-26.

[21] Ali, A., Khan, A. Q., Hussain, B., Raza, M. T., & Arif, M. (2015). Fault modelling and detection in power generation, transmission and distribution systems. IET Generation, Transmission & Distribution, 9(16), 2782-2791.

[22] Patel, D., Chothani, N. G., Mistry, K. D., & Raichura, M. (2018). Design and development of fault classification algorithm based on relevance vector machine for power transformer. IET electric power applications, 12(4), 557-565.

[23] Dhar, S., Patnaik, R. K., & Dash, P. K. (2017). Fault detection and location of photovoltaic based DC microgrid using differential protection strategy. IEEE Transactions on Smart Grid, 9(5), 4303-4312.

[24] Manohar, M., Koley, E., & Ghosh, S. (2018). Reliable protection scheme for PV integrated microgrid using an ensemble classifier approach with real-time validation. IET Science, Measurement & Technology, 12(2), 200-208.

[25] Eid, B. M., Abd Rahim, N., Selvaraj, J., & Elkhateb, A. (2014). Control methods and objectives for electronically coupled distributed energy resources in microgrids: A review. IEEE systems journal, 10(2), 446-458.

[26] Morshed, M. J., & Fekih, A. (2016). A fault-tolerant control paradigm for microgrid-connected wind energy systems. IEEE Systems Journal, 12(1), 360-372.

[27] Nademi, H., Vanfretti, L., & Pretlove, J. (2020). Fault detection method in subsea power distribution systems using statistical optimisation. IET Energy Systems Integration, 2(2), 144-150.

[28] Heidary, A., Radmanesh, H., Naghibi, S. H., Samandarpour, S., Rouzbehi, K., & Shariati, N. (2020). Distribution system protection by coordinated fault current limiters. IET Energy Systems Integration, 2(1), 59-65.

[29] Mukherjee, N., Chattopadhyaya, A., Chattopadhyay, S., & Sengupta, S. (2020). Discrete-wavelet-transform and stockwell-transform-based statistical parameters estimation for fault analysis in grid-connected wind power system. IEEE Systems Journal, 14(3), 4320-4328.

[30] Li, D., Ukil, A., Satpathi, K., & Yeap, Y. M. (2020). Improved S transform-based fault detection method in voltage source converter interfaced DC system. IEEE Transactions on Industrial Electronics, 68(6), 5024-5035.

[31] Ahmad, G., Mahela, O. P., & Ola, S. R. (2018, February). A stockwell transform based approach for detection of transmission line faults in the presence of thyristor controlled reactor. In 2018 5th International Conference on Signal Processing and Integrated Networks (SPIN) (pp. 691-695). IEEE.

[32] Ola, S. R., Saraswat, A., Goyal, S. K., Jhajharia, S. K., & Mahela, O. P. (2018, December). A technique using Stockwell transform based median for detection of power system faults. In 2018 IEEE 8th Power India International Conference (PIICON) (pp. 1-5). IEEE.

[33] Ghorbani, A., & Mehrjerdi, H. (2020). Accurate fault location algorithm for shunt-compensated double circuit transmission lines using single end data. International Journal of Electrical Power & Energy Systems, 116, 105515.

[34] Ghorbani, A., & Mehrjerdi, H. (2019). Negative-sequence network based fault location scheme for double-circuit multi-terminal transmission lines. IEEE Transactions on Power Delivery, 34(3), 1109-1117.

[35] Hemmati, R., & Mehrjerdi, H. (2019). Non-standard characteristic of overcurrent relay for minimum operating time and maximum protection level. Simulation Modelling Practice and Theory, 97, 101953.

[36] Mehrjerdi, H., & Ghorbani, A. (2017). Adaptive algorithm for transmission line protection in the presence of UPFC. International Journal of Electrical Power & Energy Systems, 91, 10-19.

[37] Ghorbani, A., Mehrjerdi, H., & Al-Emadi, N. A. (2017). Distance-differential protection of transmission lines connected to wind farms. International Journal of Electrical Power & Energy Systems, 89, 11-18.

[38] Vyas, B., Maheshwari, R. P., & Das, B. (2014). Evaluation of artificial intelligence techniques for fault type identification in advanced series compensated transmission lines. IETE Journal of Research, 60(1), 85-91.

[39] Agrawal, S., Mohanty, S. R., & Agarwal, V. (2015). Bearing fault detection using Hilbert and high frequency resolution techniques. IETE Journal of Research, 61(2), 99-108.

[40] Eskander, M. N., & Amer, S. I. (2011). Mitigation of voltage dips and swells in grid-connected wind energy conversion systems. IETE Journal of Research, 57(6), 515-524.

[41] Panigrahi, B. K., Sinha, S. K., Mohapatra, A., Dash, P., & Mallick, M. K. (2011). A comparative study of signal processing and pattern recognition approach for power quality disturbance classification. IETE Journal of Research, 57(1), 5-11.

[42] Elmasry, W., & Wadi, M. (2022). Detection of faults in electrical power grids using an enhanced anomaly-based method. Arabian Journal for Science and Engineering, 47(11), 14899-14914.

[43] Wong, S. Y., Choe, C. W. C., Goh, H. H., Low, Y. W., Cheah, D. Y. S., & Pang, C. (2021). Power transmission line fault detection and diagnosis based on artificial intelligence approach and its development in uav: A review. Arabian Journal for Science and Engineering, 46(10), 9305-9331.

[44] Mayadevi, N., Mini, V. P., Hari Kumar, R., & Prins, S. (2020). Fuzzy-based intelligent algorithm for diagnosis of drive faults in induction motor drive system. Arabian Journal for Science and Engineering, 45(3), 1385-1395.

[45] Kar, D., Chattopadhyay, S., Sharma, K. D., & Sengupta, S. (2016, January). Identification of faulty load bus in a multi-bus power system. In 2016 2nd International Conference on Control, Instrumentation, Energy & Communication (CIEC) (pp. 289-293). IEEE.

[46] Ray, D. K., Chattopadhyay, S., Sharma, K. D., & Sengupta, S. (2015, September). Steady state harmonic stability analysis in IEEE 14 bus system for fault at generator bus. In Michael Faraday IET International Summit 2015 (pp. 261-266). IET.

[47] Azevedo, G. M., Arruda, J. P., Cavalcanti, M. C., & Limongi, L. R. (2015, November). Fault detection system to trigger the microgrid disconnection procedures. In 2015 IEEE 13th Brazilian Power Electronics Conference and 1st Southern Power Electronics Conference (COBEP/SPEC) (pp. 1-6). IEEE.

[48] Mishra, S., Bhende, C. N., & Panigrahi, B. K. (2007). Detection and classification of power quality disturbances using S-transform and probabilistic neural network. IEEE Transactions on power delivery, 23(1), 280-287.

[49] He, Z., Fu, L., Lin, S., & Bo, Z. (2010). Fault detection and classification in EHV transmission line based on wavelet singular entropy. IEEE transactions on Power Delivery, 25(4), 2156-2163.

[50] Pignati, M., Zanni, L., Romano, P., Cherkaoui, R., & Paolone, M. (2016). Fault detection and faulted line identification in active distribution networks using synchrophasors-based real-time state estimation. IEEE Transactions on power delivery, 32(1), 381-392.

[51] Kumar, R., Singh, B., Shahani, D. T., Chandra, A., & Al-Haddad, K. (2014). Recognition of power-quality disturbances using S-transform-based ANN classifier and rule-based decision tree. IEEE Transactions on Industry Applications, 51(2), 1249-1258.

[52] Lin, C., Gao, W., & Guo, M. F. (2019). Discrete wavelet transform-based triggering method for single-phase earth fault in power distribution systems. IEEE Transactions on Power Delivery, 34(5), 2058-2068.

[53] Hatipoglu K, Cakir G, Fidan I (2013) Implementation of faults in a microgrid environment with MATLAB based GUI. In: Proceedings of IEEE Southeastcon - 428-434, Jacksonville, USA, April 2013.

[54] Ghanbari, T., & Farjah, E. (2012). Unidirectional fault current limiter: An efficient interface between the microgrid and main network. IEEE Transactions on Power Systems, 28(2), 1591-1598.

[55] Mishra, M., Sahani, M., & Rout, P. K. (2017). An islanding detection algorithm for distributed generation based on Hilbert–Huang transform and extreme learning machine. Sustainable Energy, Grids and Networks, 9, 13-26.

[56] Ikhide, M., Tennakoon, S. B., Ha, H., Griffiths, A. L., Subramanian, S., & Adamczyk, A. J. (2019). A transient and non-unit-based protection technique for DC grids based on the rate-of-change (RoC) of the fault induced travelling wave components. Sustainable Energy, Grids and Networks, 17, 100195.

[57] Gkavanoudis, S. I., & Demoulias, C. S. (2015). A control strategy for enhancing the fault ride-through capability of a microgrid during balanced and unbalanced grid voltage sags. Sustainable Energy, Grids and Networks, 3, 1-11.

[58] Tan, Y., Sun, Y., & Yin, X. (2013). Analog fault diagnosis using S-transform preprocessor and a QNN classifier. Measurement, 46(7), 2174-2183.

[59] Mohamad, N. Z., & Abidin, A. F. (2012, March). S-Transform based technique to detect high resistance symmetrical fault during power swing. In 2012 IEEE 8th International Colloquium on Signal Processing and its Applications (pp. 282-286). IEEE.

[60] Roy, N., & Bhattacharya, K. (2013, December). Identification and classification of fault using S-transform in an unbalanced network. In 2013 IEEE 1st International Conference on Condition Assessment Techniques in Electrical Systems (CATCON) (pp. 111-115). IEEE.

[61] Routray, P., Mishra, M., & Rout, P. K. (2015, October). High impedance fault detection in radial distribution system using S-transform and neural network. In 2015 IEEE Power, Communication and Information Technology Conference (PCITC) (pp. 545-551). IEEE.

[62] Santos, G. G., Menezes, T. S., Vieira, J. C. M., & Barra, P. H. A. (2019, August). An S-transform based approach for fault detection and classification in power distribution systems. In 2019 IEEE Power & Energy Society General Meeting (PESGM) (pp. 1-5). IEEE.

[63] Devi, S., Swarnkar, N. K., Ola, S. R., & Mahela, O. P. (2016, June). Detection of transmission line faults using discrete wavelet transform. In 2016 Conference on Advances in Signal Processing (CASP) (pp. 133-138). IEEE.

[64] Choudhury, M., & Ganguly, A. (2015, June). Transmission line fault classification using discrete wavelet transform. In 2015 International Conference on Energy, Power and Environment: Towards Sustainable Growth (ICEPE) (pp. 1-5). IEEE.

[65] Chattopadhyaya, A., Banerjee, H., Chattopadhyay, S., & Sengupta, S. (2013). Assessment of CT saturation caused by switching transient. International Journal of Electrical Electronics and Communication Engineering, 2(2), 57-61.

[66] Mahfouz, M. M., & El-Sayed, M. A. (2020). Fault detection scheme based on feeder buses impedance angles discriminator in smart microgrid. Sustainable Energy, Grids and Networks, 23, 100379.

[67] Tiwari, S. P., Koley, E., & Ghosh, S. (2021). Communication-less ensemble classifier-based protection scheme for DC microgrid with adaptiveness to network reconfiguration and weather intermittency. Sustainable Energy, Grids and Networks, 26, 100460.

[68] Do Nascimento, L. L., & Rolim, J. G. (2013, April). Multi-agent system for adaptive protection in microgrids. In 2013 IEEE PES conference on innovative smart grid technologies (ISGT Latin America) (pp. 1-8). IEEE.

[69] Banerjee, S., & Bhowmik, P. S. (2020, February). Transient disturbances and islanding detection in micro grid using discrete wavelet transform. In 2020 IEEE Calcutta Conference (CALCON) (pp. 396-401). IEEE.

[70] Salomonsson, D., Soder, L., & Sannino, A. (2009). Protection of low-voltage DC microgrids. IEEE Transactions on power delivery, 24(3), 1045-1053.

[71] Ustun, T. S., Ozansoy, C., & Zayegh, A. (2011, November). Extending IEC 61850-7-420 for distributed generators with fault current limiters. In 2011 IEEE PES innovative smart grid technologies (pp. 1-8). IEEE.

[72] Ustun, T. S., Ozansoy, C., & Zayegh, A. (2011, September). Distributed Energy Resources (DER) object modeling with IEC 61850–7–420. In AUPEC 2011 (pp. 1-6). IEEE.

[73] Mohanty, R., Balaji, U. S. M., & Pradhan, A. K. (2015). An accurate noniterative fault-location technique for low-voltage DC microgrid. IEEE Transactions on Power Delivery, 31(2), 475-481.

[74] Qiu, W., Tang, Q., Liu, J., Teng, Z., & Yao, W. (2019). Power quality disturbances recognition using modified S - Transform and parallel stack sparse auto-encoder. Electric Power Systems Research, 174, 105876.

[75] Bindumol, E. K. (2022, November). High impedance fault detection and control methods in ac microgrids: a review. In 2022 IEEE 19th India Council International Conference (INDICON) (pp. 1-6). IEEE.

[76] Nanda, S., Barik, S. K., Senapati, R. N., & Pattanayak, B. (2024, November). Application of Artificial Neural Network in Detecting, Locating, Classifying and Isolating AC Faults in Grid-Integrated Microgrid. In 2024 3rd Odisha International Conference on Electrical Power Engineering, Communication and Computing Technology (ODICON) (pp. 1-6). IEEE.

[77] Criollo, P., Ortiz, L., Aguila, A., & Pavón, W. (2022, October). A method based on a sliding mode observer for fault detection in photovoltaic solar systems connected to AC microgrids. In 2022 IEEE Sixth Ecuador Technical Chapters Meeting (ETCM) (pp. 1-6). IEEE.

[78] Prince, S. K., Elghali, S. B., Affijulla, S., & Panda, G. (2023, October). Robust Fault Detection and Characterisation in AC Microgrids using Ensemble Empirical Mode Decomposition. In 2023 IEEE PES Innovative Smart Grid Technologies Europe (ISGT EUROPE) (pp. 1-5). IEEE.

[79] Mola, M., Afshar, A., Meskin, N., & Karrari, M. (2020). Distributed fast fault detection in DC microgrids. IEEE Systems Journal, 16(1), 440-451.

[80] Miao, W., Zhi, F., Wang, F., Zhou, X., & Luo, Y. (2022, September). Arc Fault Detection and Location Technique Based on State Space Modeling for DC Microgrid. In 2022 7th International Conference on Power and Renewable Energy (ICPRE) (pp. 452-457). IEEE.

[81] Chang, F., Sun, H., Kawano, S., Nikovski, D., Kitamura, S., & Su, W. (2022, May). A fault detection and location technique for inverter-dominated islanding microgrids. In 2022 IEEE 5th International Electrical and Energy Conference (CIEEC) (pp. 2041-2046). IEEE.

[82] Takhellambam, M., Adhikari, S., & Chanu, L. K. (2024, July). Online Fault Detection and Classification of a Grid-Connected Microgrid System Based on Discrete Wavelet Transformation. In 2024 IEEE 4th International Conference on Sustainable Energy and Future Electric Transportation (SEFET) (pp. 1-5). IEEE.

[83] Ali, Z., Terriche, Y., Abbas, S. Z., Hassan, M. A., Sadiq, M., Su, C. L., & Guerrero, J. M. (2021). Fault management in DC microgrids: A review of challenges, countermeasures, and future research trends. IEEE Access, 9, 128032-128054.

[84] Sardashti, A., Ramezani, A., Nezhad, H. S., & Moradmand, A. (2019, October). Observer-based Sensor Fault Detection in Islanded AC Microgrids Using Online Recursive Estimation. In 2019 6th International Conference on Control, Instrumentation and Automation (ICCIA) (pp. 1-6). IEEE.

[85] Krommydas, K. F. (2022, October). Model-Based Fault Detection and Isolation in DC Microgrids. In 2022 2nd International Conference on Energy Transition in the Mediterranean Area (SyNERGY MED) (pp. 1-6). IEEE.

[86] Bhuyan, A., Panigrahi, B. K., Shukla, J., Pal, K., & Pati, S. (2023, November). Detection and Classification of Disturbances in DG Based Power System using Time-Frequency-Scale Transform. In 2023 IEEE Silchar Subsection Conference (SILCON) (pp. 1-6). IEEE.

[87] Jarika, D., Tudu, P., Biswal, T., Mishra, S., & Jena, S. (2025, January). A Hybrid DWT-SVM Based Approach For Fault Classification in Distribution Systems with Distributed Generators. In 2025 8th International Conference on Electronics, Materials Engineering & Nano-Technology (IEMENTech) (pp. 1-6). IEEE.

[88] Dutta, S., Jayalakshmi, N. S., & Jadoun, V. K. (2025). Shifting of Research Trends in Fault Detection and Estimation of Location in Power System. IEEE Access.

[89] Geethanjali, M. (2023, December). Fault Detection and Classification on Transmission Lines during Asymmetrical Faults using Wavelet Transformation and Decision Tree Algorithm. In 2023 International Conference on Energy, Materials and Communication Engineering (ICEMCE) (pp. 1-5). IEEE.

[90] Shaik, M., Shaik, A. G., & Yadav, S. K. (2019, November). S-Transform Based Protection Scheme for Distribution System Integrated with Solar Power Plant. In 2019 2nd International Conference on Smart Grid and Renewable Energy (SGRE) (pp. 1-6). IEEE.

[91] Naik, S. V. R., & Pulivarthi, N. R. (2024, August). Fault Diagnosis in PV Integrated Distribution System using Wavelet and Data Mining Techniques. In 2024 International Conference on Intelligent Algorithms for Computational Intelligence Systems (IACIS) (pp. 1-6). IEEE.

[92] Gashteroodkhani, O. A., Aznavi, S., Majidi, M., & Etezadi-Amoli, M. (2019, August). An intelligent protection scheme for microgrids based on S-transform and deep belief network. In 2019 IEEE Power & Energy Society General Meeting (PESGM) (pp. 1-5). IEEE.

[93] Jayamaha, D. K. J. S., Lidula, N. W. A., & Rajapakse, A. D. (2019). Wavelet-multi resolution analysis based ANN architecture for fault detection and localization in DC microgrids. IEEE Access, 7, 145371-145384.

[94] Joga, S. R. K., Sinha, P., Maharana, M. K., Jena, C., Mishra, A., & Roy, A. (2022, May). Stockwell Transform and Data Mining based Fault Diagnosis Method to protect Microgrid. In 2022 3rd International Conference for Emerging Technology (INCET) (pp. 1-5). IEEE.

[95] Pandey, P., & Biswas, S. (2023, June). Microcontroller Assist Fault Detection for Microgrids Based on Discrete Wavelet Transform. In 2023 5th International Conference on Energy, Power and Environment: Towards Flexible Green Energy Technologies (ICEPE) (pp. 1-6). IEEE.

[96] Thattai, K., Sahoo, A., & Ravishankar, J. (2018, April). On-line and off-line fault detection techniques for inverter based islanded microgrid. In 2018 IEEE 12th International Conference on Compatibility, Power Electronics and Power Engineering (CPE-POWERENG 2018) (pp. 1-6). IEEE.

[97] Ranjbar, S., & Jamali, S. (2019, January). Fault detection in microgrids using combined classification algorithms and feature selection methods. In 2019 International Conference on Protection and Automation of Power System (IPAPS) (pp. 17-21). IEEE.

[98] Hong, Y. Y., & Cabatac, M. T. A. M. (2019). Fault detection, classification, and location by static switch in microgrids using wavelet transform and taguchi-based artificial neural network. IEEE Systems Journal, 14(2), 2725-2735.

[99] Kar, S., Samantaray, S. R., & Zadeh, M. D. (2015). Data-mining model based intelligent differential microgrid protection scheme. IEEE Systems Journal, 11(2), 1161-1169.

[100] Stanisavljević, A. M., Katić, V. A., Dumnić, B. P., & Popadić, B. P. (2019, September). Application of S-Transform for voltage dips detection and analysis in modern distribution grids. In 2019 21st European Conference on Power Electronics and Applications (EPE'19 ECCE Europe) (pp. 1-5). IEEE.

[101] Saifuddin, M. R. B. M., Logenthiran, T., Naayagi, R. T., & Woo, W. L. (2018). Apprehending fault crises for an autogenous nanogrid system: Sustainable buildings. IEEE Systems Journal, 13(3), 3254-3265.

[102] Yan, J., Changgang, Li., Yutian, L., Dongxiao, Y., & Zhiping, J. (2024). Incremental Model Evolution for Power System Security Early Warning Based on Knowledge Distillation and Active Learning. IEEE Transactions on Industrial Informatics 20(1), 12958-12968.

[103] Saxena, K., Samantaray S. R., & Nanda S. (2026). A Faster µ-PMU Algorithm using Arctangent Framework with Parameter Step Change. IEEE Transactions on Smart Grid, doi: 10.1109/TSG.2026.3664302.

[104] Kanth, M. U., & Jena, P. (2026). A Symmetrical Component Decomposition-Based Unified Protection Technique for Hybrid AC/DC Microgrid. IEEE Transactions on Industrial Electronics, doi: 10.1109/TIE.2025.3645432.

[105] Stockwell RG, Mansinha L, Lowe R.P (1996) Localization of the complex spectrum: the S transform. IEEE Transactions on Signal Processing 44(4):99-114

[106] "Engineering Statistics Handbook", NIST/SEMATECH e-Handbook of Statistical Methods, NIST, Retrieved 18th March 2012.

Sagnik Datta
08.04.2026.

Analinda Das.
08/04/2026
Professor
Electrical Engg. Deptt.
Jadavpur University
Kolkata - 700 032

Surajit Chattopadhyay
08.04.2026
Associate Professor
Department of Electrical Engineering
Ghani Khan Choudhury Institute of Engineering & Technology
Narayanpur Malda